Theoretical investigation for electrochemical CO_2 reduction on silver and tin surfaces

Bandar Alsuwayni (Postgraduate Researcher)

This dissertation is submitted for the degree of Doctor of Philosophy

2026

Department of Physics, Lancaster University, UK

Declaration

This thesis has not been submitted in support of an application for another degree at this or any other university. It is the result of my work and includes nothing that is the outcome of work done in collaboration except where specifically indicated. Many of the ideas in this thesis were the product of discussion with my supervisor Prof. Colin Lambert and my co-supervisor, Dr. Qingqing Wu.

Bandar Alsuwayni

2026

Abstract

This thesis investigates strategies for enhancing electrochemical carbon dioxide (CO_2) reduction through a systematic study of catalyst surface modification. Particular attention is given to silver (Ag) and tin (Sn) as base materials, with a focus on the role of dopants in improving catalytic activity and selectivity. In CO_2 electroreduction, the nature and stability of reaction intermediates are critical in determining product distribution. In particular, *COOH is widely recognised as the key intermediate in the formation of carbon monoxide, whereas *OCHO governs the pathway towards formic acid. The competition between these intermediates for active sites plays a decisive role in controlling catalytic selectivity.

The study employs density functional theory (DFT) calculations using the Vienna *Ab initio* Simulation Package (VASP), with the generalised gradient approximation (GGA) to analyse the geometric and electronic properties of the investigated systems. The results provide detailed insights into how targeted doping strategies can be used to optimise catalyst performance.

For Ag-based systems, silver and gold clusters supported on the Ag (111) surface are examined to evaluate the effects of cluster composition and size. The presence of these clusters significantly alters the reaction energetics associated with *COOH formation. Smaller Ag clusters exhibit slightly greater reductions in energy barriers than larger ones, whereas larger Au clusters demonstrate superior performance compared with their smaller counterparts. This highlights a distinct size-dependent effect that varies with cluster composition.

For Sn-based systems, bismuth (Bi) doping is investigated in both adsorbed and substitutional configurations relative to pristine Sn surfaces. Bi incorporation enhances catalytic activity and promotes selectivity towards formate formation under both gas-phase and solvated conditions. Among the configurations studied, Bi atoms adsorbed on the Sn surface yield the most favourable energetic profiles, characterised by lower reaction barriers. However, achieving precise control over the adsorption of competing intermediates (*COOH and *OCHO) remains a key challenge for further improving selectivity.

Overall, this work demonstrates that rational surface modification through doping provides an effective strategy for tuning activity and selectivity in CO_2 electroreduction catalysts.

Acknowledgments

I would like to express my deepest gratitude to my supervisor, Professor Colin, and my co-supervisor, Dr Qingqing, for their unwavering support and guidance throughout my PhD studies. Their expertise and encouragement were crucial, particularly during the most challenging times.

I dedicate this work to my parents, who passed away recently. My father, Khalid Alsuwayni, passed away last year, and my mother, Mohrah Alsuwayni, followed six months later. Their absence is profoundly felt, and I deeply wish they could have witnessed the completion of this work.

I am eternally grateful to my wife, Jamilah Aljameel, and my children, Khalid and Abdulaziz, whose love and patience have been a constant source of strength throughout my academic journey. I am also delighted to welcome my newborn son, Turki, who was born in March 2026, and whose arrival has brought immense joy to our family.

I am also deeply thankful to my brother, Turki, for his emotional support, as well as my best friend, Thamer Altamimi, for his companionship and encouragement. I also wish them every success in their PhD studies.

My heartfelt gratitude extends to my sisters, Ahlam and Khulud, for their unwavering emotional and moral support. Additionally, I am grateful to my uncle, Fahad Alsuweina, for his support during the difficult period of bereavement.

Finally, I would like to extend my sincere thanks to the Ministry of Higher Education in Saudi Arabia and the University of Hail for their invaluable support and scholarship, which made this academic journey possible.

Contents

1.Introduction

1.1 General introduction

Carbon dioxide (CO_2) is a ubiquitous gas in nature, accounting for about 0.03% of the air. Although its content is very low, its existence is indispensable for the evolution of the earth's ecological environment, which is used by plants through photosynthesis to transform into a variety of hydrocarbons. As a naturally occurring gas on earth, the low concentration of CO_2 is harmless. However, the concentration of CO_2 in the atmosphere has been increasing year by year due to the impact of energy consumption and human activities since the industrial revolution. Nevertheless, the absorption of CO_2 by seawater leads to important chemical changes. When CO_2 dissolves in the ocean, it forms carbonic acid, altering the chemical equilibrium of seawater [1]. This process increases the concentration of hydrogen ions, resulting in ocean acidification, and decreases the availability of carbonate ions. Carbonate ions are essential for marine organisms, such as corals and shell-forming species, to build their skeletons and shells. Therefore, while ocean uptake of CO_2 reduces atmospheric concentrations, it simultaneously poses a threat to marine ecosystems.

Nowadays, the concentration of CO_2 in the atmosphere has risen from 320 ppm in 1960 to 425 ppm in August 2025, as shown in Figure 1A [1]. With the increasing CO_2 concentration in the atmosphere, the harm it brings is becoming more obvious. As a kind of greenhouse gas, a high concentration of CO_2 firstly increases the global temperature. The Intergovernmental panel on climate change (IPCC) research indicates that human activities are estimated to have caused global warming to be approximately 1.0 ºC above pre-industrial levels, with a possible range of 0.8 °C to 1.3 °C [2]. Today, global warming has reached 1.29 ºC [2], as shown in Figure 1B. Global warming will lead to a series of environmental problems, such as climate change,

bipolar glacier melting and sea-level rise, which will seriously harm the survival of animals and humans on earth [2]. Besides, recent studies have shown that increased concentrations of CO_2 in the atmosphere can also affect plant growth, such as reducing crop yields and nutritional value [3,4]. To avoid this situation, many countries around the world joined the Paris Climate Agreement, aiming to limit global warming to 2 ºC relative to the pre-industrial temperature, and try to control it at 1.5 ºC [5].

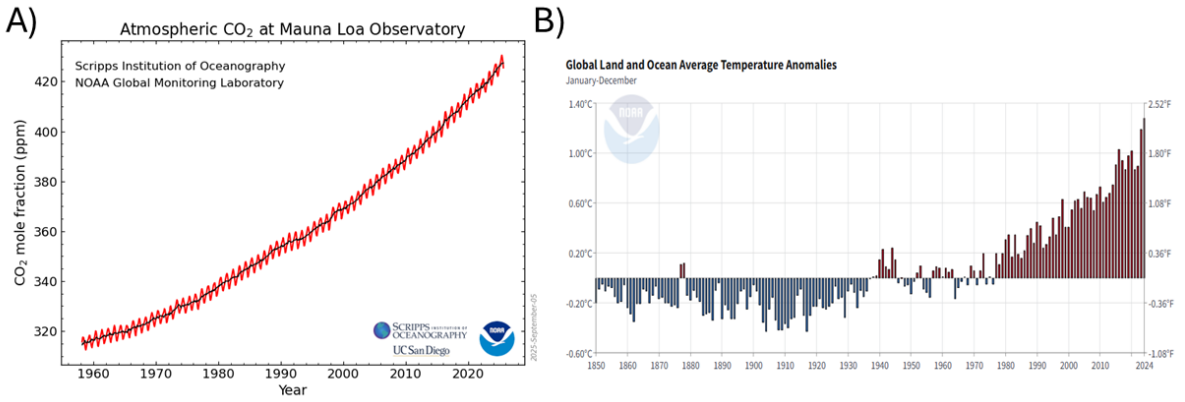

Fig 1. A) Increase in CO_2 atmospheric concentration from 1958-2025. B) The surface temperature from 1880–2023 Ref. [1,2].

1.2 CO_2 capture and utilization

In order to reduce the concentration of CO_2 in the atmosphere, human society must, on the one hand, minimise CO_2 emissions as far as possible. This can be achieved by imposing appropriate limits on industrial emissions and by actively developing renewable energy sources such as solar, wind, and tidal energy. On the other hand, researchers are exploring approaches to capture CO_2 directly from the atmosphere and store it. Carbon capture and storage (CCS) is considered an effective method for reducing atmospheric CO_2 concentrations and has become a significant area of research in the twenty-first century. One approach within this field is the electrochemical reduction of CO_2 (CO_2RR).

However, the large-scale deployment of CCS technologies is constrained by three major challenges. First, conventional CO_2 capture processes are highly energy intensive. After CO_2 is captured using solid or liquid adsorbents, it typically requires desorption at elevated temperatures, which significantly increases overall energy consumption. Second, there are persistent technical challenges associated with CO_2 separation, particularly in chemical processes, which contribute to inefficiencies and a high rate of project failure. Evidence indicates that between 1972 and 2018, 88% of CCS projects were not completed, with failure rates in the energy sector exceeding 90% (Kazlou et al., 2024). Third, economic and institutional barriers further hinder implementation. The high costs of capture and storage technologies, combined with the historical failure of many projects, have led to cautious investment behaviour among both governments and private companies. Therefore, carbon capture technologies remain costly and difficult to implement, as each project is unique and dependent on multiple contextual factors. Consequently, the development of low-cost and technically viable CO_2 treatment methods has attracted increasing attention.

From another perspective, CO_2 is an important carbon resource in nature. It can be converted into various organic substances by photosynthesis of plants. Therefore, the conversion and utilization of CO_2 is a more promising way. It can not only reduce the CO_2 concentration in the atmosphere but also convert it into other high value-added chemicals for producing economic benefits. The currently common CO_2 conversion technologies include thermochemical [6], biochemical [7], photochemical [8], and electrochemical [9] conversion methods. The main issues in methods such as photochemical and biocatalytic is lower efficiency. In addition, photochemical method has lower selectivity [10]. Thermochemical conversion usually requires high temperature and pressure, so the energy consumption is large [11]. Thus, the electrochemical CO_2 reduction reaction (CO2RR) technology attracts more attention due to its unique advantages, which will be discussed further in the following sections.

1.3 Electrochemical reduction of CO_2

CO_2 electroreduction technology attracts rapidly growing attention recently due to its potential to meet both energy and environmental problems [12-16]. It has become a research hotspot in many research fields such as chemistry, energy, environment and material science. CO_2 is very stable at normal temperature, which makes its chemical fixation and conversion very difficult. The reduction of CO_2 by traditional chemical methods requires the provision of a large amount of hydrogen and also consumes huge amounts of energy. In contrast, the electrochemical CO2RR is carried out at ambient temperature and pressure, and the product selectivity and reaction rate can be easily adjusted by changing the electrolytic conditions. More importantly, as shown in Figure 2, the CO_2 electro-reduction process can be combined with the use of renewable energy sources such as solar, wind and tidal energy to directly obtain high-value chemicals [17]. These chemicals can be used directly as chemical reagents for scientific research, or as raw materials for industrial synthesis or as fuel for new energy vehicles, thereby achieving large-scale energy storage [18]. This technology shows a very promising application prospect, which is in line with the goal of human sustainable development.

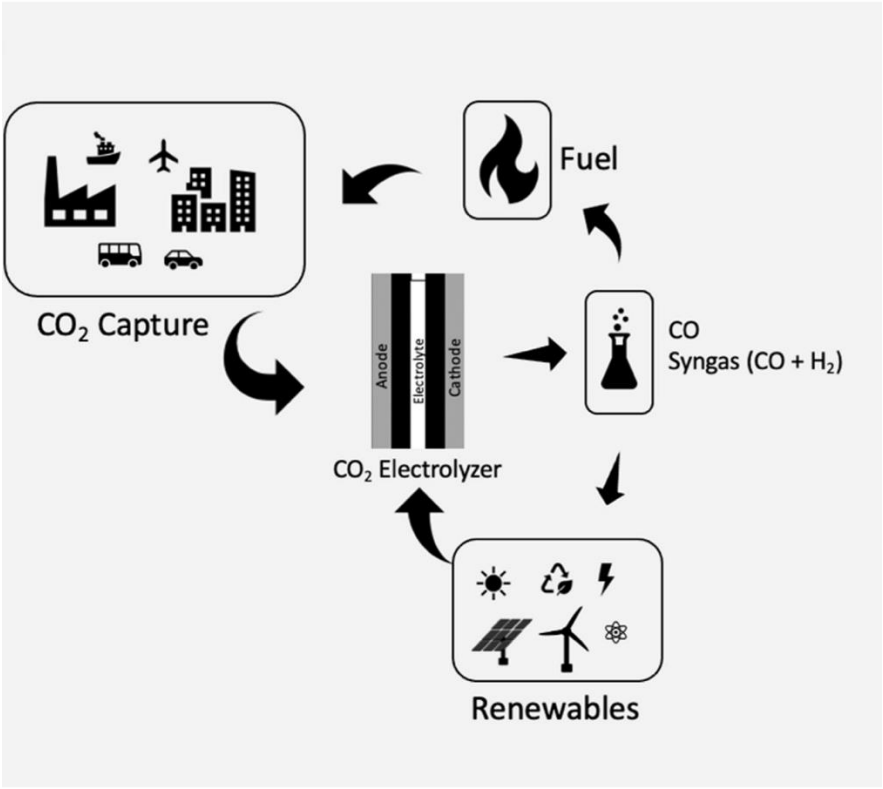

Fig 2. Schematic illustration of the electrochemical (CO2RR) [17].

Electrochemical systems for carbon dioxide reduction reactions (CO2RR) consist of the following essential components: an anode, a cathode, an aqueous electrolyte, and a membrane. At the anode, the Oxygen Evolution Reaction (OER) occurs, while the cathode facilitates the CO2RR process. The membrane plays a crucial role by segregating the products formed during oxidation and reduction product, ensuring charge balance, and establishing a closed loop system that facilitates proton transfer to the cathode [19].

The mechanism for electrochemical oxidation and reduction mechanism taking place at anode and cathode respectively are illustrated in Figure 3. When external positive bias is applied at the electrode (anode), the chemical potential of the metal electrode decreases. Consequently, the highest occupied molecular orbital (HOMO) of the molecule (i.e. H_2O in our case), becomes higher in energy and loses its electron to the anode, resulting in the oxidation of the molecule and thus the formation of O_2 as a product. On the other hand, when negative external

bias is applied, the chemical potential of the metal electrode (cathode) becomes higher in energy than the lowest unoccupied molecular orbital (LUMO) of the nearby molecule (i.e.CO_2). The LUMO of CO_2 accepts the electrons from the cathode, resulting in reduction and the formation of different products.

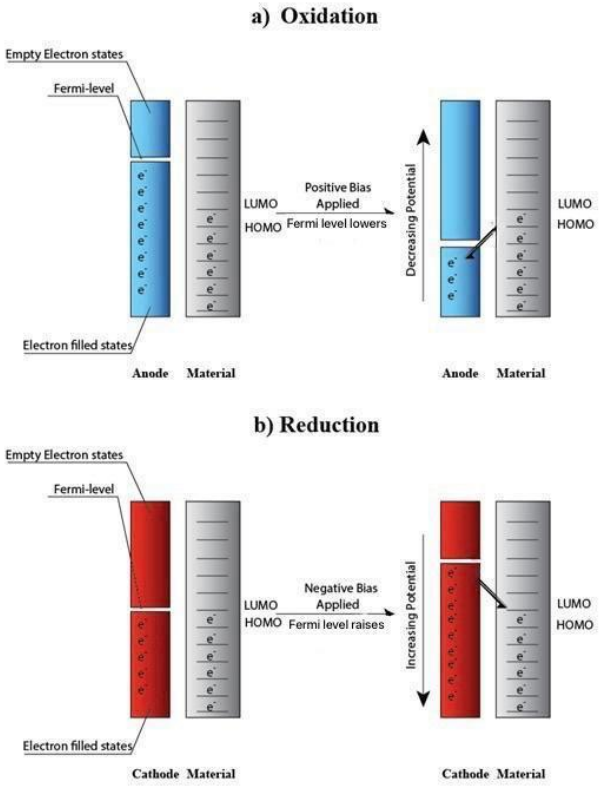

Fig 3. The mechanisms of electrochemical oxidation and reduction take place at the anode and cathode, respectively.

1.3.1 Common products and catalysts

Although electrochemical reduction of CO_2 is considered as a CO_2 resource conversion method with great industrial production potential, it has not yet achieved industrial application [20]. The main limitations are insufficient activity and selectivity of electrocatalysts, and low energy utilization efficiency. Due to the very high chemical stability of CO_2, electrocatalytic reactions usually require a high overpotential to occur in order to overcome the reaction barrier. Besides, the existence of competitive electrocatalytic hydrogen evolution reaction (HER) leads to the

low energy conversion efficiency of the CO2RR [21]. Therefore, it is important to develop efficient CO_2 electroreduction catalysts.

$$CO_2 + H^+ + 2e^- \rightarrow HCOO^- \quad (1\text{-}1)$$

$$CO_2 + 2H^+ + 2e^- \rightarrow CO + H_2O \quad (1\text{-}2)$$

$$CO_2 + 8H^+ + 8e^- \rightarrow CH_4 + 2H_2O \quad (1\text{-}3)$$

$$CO_2 + 6H^+ + 6e^- \rightarrow CH_3OH + H_2O \quad (1\text{-}4)$$

$$2CO_2 + 12H^+ + 12e^- \rightarrow C_2H_4 + 4H_2O \quad (1\text{-}5)$$

$$2CO_2 + 12H^+ + 12e^- \rightarrow C_2H_5OH + 3H_2O \quad (1\text{-}6)$$

As shown in Equations (1-1)–(1-6), CO_2 can be electrochemically reduced to a wide range of products, including formic acid (HCOOH), carbon monoxide (CO), methane (CH_4), methanol (CH_3OH), ethylene (C_2H_4), and ethanol (C_2H_5OH), depending on the applied electrode potential and the nature of the electrocatalyst [18,22] . However, the thermodynamic potentials associated with these reaction pathways are relatively close to one another. When referenced to the reversible hydrogen electrode (RHE), the standard electrode potentials for carbon dioxide reduction reactions (CO_2RR) fall within a narrow range, indicating only minor thermodynamic differences between competing pathways. For example, Hussain J. et al. [23] reported that at an applied potential of around -1 V, the corresponding reaction step exhibits a relatively low activation energy in the range of 0.2-0.35 eV for most metal electrodes investigated, whereas significantly higher activation energies, between 0.6 and 1.0 eV, were observed for Au and Ag surfaces. This close proximity of reaction potentials makes precise control over product selectivity particularly challenging, often resulting in the simultaneous formation of multiple products [23]. Consequently, the development of highly active and selective electrocatalysts is critical for improving energy efficiency and directing reaction pathways in CO_2RR.

Electrocatalysts employed for CO_2RR are generally classified into metal-based and metal-free catalysts. Among these, metal-based catalysts remain the most widely studied and practically relevant owing to their excellent electrical conductivity and comparatively high catalytic selectivity [22]. As illustrated in Figure 4, metal electrocatalysts can be broadly categorized into three groups based on their dominant CO_2 reduction products [18]. The first group includes metals such as Au, Ag, and Zn, which preferentially catalyse the formation of CO. The second group consists of metals such as Sn, Bi, In, and Pb, for which formic acid (HCOOH) is the primary reduction product. The third category is represented by copper-based catalysts, which exhibit unique CO_2RR behaviour. Copper is notably the only metal capable of producing a diverse range of hydrocarbons and oxygenated products, including CH_4, C_2H_4, and C_2H_5OH, with appreciable efficiency [24].

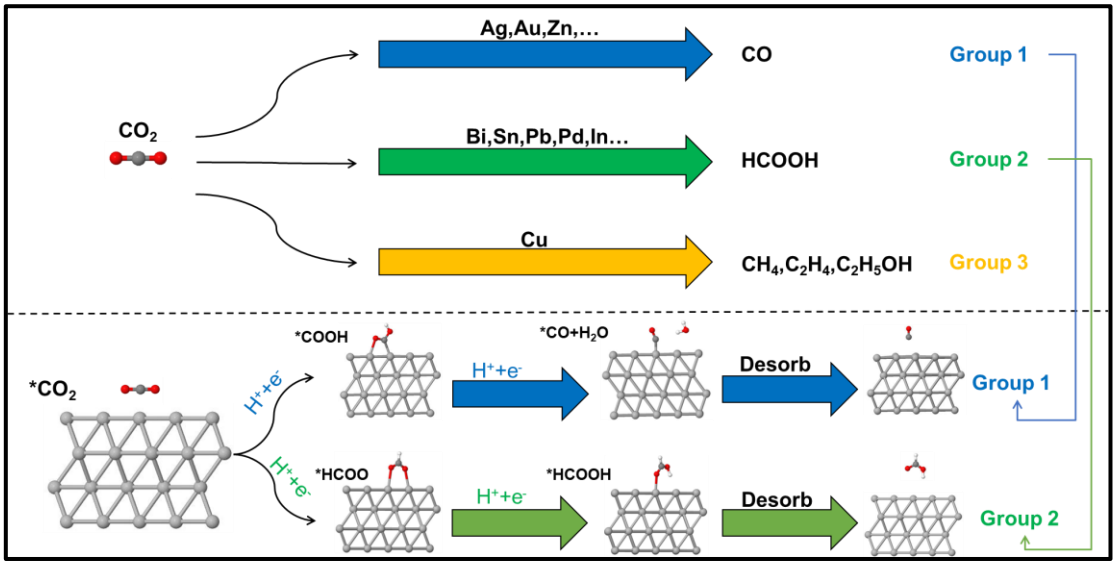

Fig 4. The common metal catalysts for electrocatalytic CO_2RR and their possible catalytic mechanism.

Density functional theory (DFT) studies have provided important insights into the origin of product selectivity on different metal surfaces. These studies suggest that two key intermediates, *COOH and *HCOO, can form during the initial stages of CO_2 reduction [25].

Metals such as Ag and Zn exhibit strong binding to the *COOH intermediate, facilitating its subsequent reduction to CO. In contrast, metals such as Sn, Bi, and Pb preferentially stabilize the *HCOO intermediate, leading predominantly to the formation of HCOOH. Copper, on the other hand, exhibits a stronger binding affinity for CO, which promotes further hydrogenation of adsorbed CO species and enables the formation of hydrocarbons and alcohols [25]. A detailed understanding of these reaction mechanisms and intermediate binding behaviours is therefore essential for the rational design of high-performance electrocatalysts for CO_2 reduction.

1.4 Improving the performance of catalysts

Since the beginning of the 21st century, it has been widely recognized that nanoscale effects play a decisive role in determining the activity, selectivity, and long-term stability of catalysts for electrochemical CO_2 reduction [26]. This recognition has driven extensive research efforts toward the rational design of nano-catalysts through precise control over their structural, electronic, and compositional characteristics. At the nanoscale, variations in atomic coordination, surface morphology, and electronic structure can significantly influence the adsorption, activation, and conversion pathways of CO_2 and key reaction intermediates, thereby dictating overall catalytic performance.

To address these challenges, a range of catalyst engineering strategies has been developed to enhance CO_2 electroreduction performance [27]. Among these, defect engineering and composition modulation have emerged as particularly effective approaches. The intentional introduction of defects (such as vacancies, grain boundaries, and lattice distortions can generate) low-coordination active sites, modify local electronic environments, and promote favourable adsorption energies for CO_2-derived intermediates. Similarly, adjusting catalyst

composition through elemental doping, alloying, or heterostructure construction enables fine-tuning of electronic structure and surface chemistry, allowing for improved reaction kinetics, enhanced product selectivity, and suppressed competing reactions such as hydrogen evolution.

These performance-enhancement strategies are closely linked to advances in catalyst synthesis and characterization techniques, which enable precise control over nanostructure and surface properties while providing mechanistic insight into structure–performance relationships [27]. In situ and operando characterization methods have played a crucial role in elucidating dynamic structural and electronic changes under electrochemical operating conditions. The following section systematically reviews the principal strategies employed to improve the performance of nano-catalysts for electrochemical CO_2 reduction, with a specific focus on the mechanistic origins of their enhanced catalytic behaviour. Such understanding is essential for guiding the rational design of highly efficient and selective catalysts for sustainable CO_2 conversion.

1.4.1 Making defects.

In recent years, crystallography researchers have increasingly recognised that structural imperfections such as defects, dislocations, and grain boundaries play a crucial role in determining the catalytic performance of crystalline materials [28]. Crystal defects, defined as localised disruptions in the periodic arrangement of atoms within the lattice, frequently give rise to unique physicochemical properties that can substantially enhance catalytic activity. These irregularities often create unsaturated coordination sites, modify the electronic environment, and facilitate the adsorption and activation of reactant molecules, thereby providing pathways that are inaccessible on ideal crystal surfaces.

A pertinent experimental example is provided by the work of Gong et al., who successfully synthesised defective bismuth nanotubes via the electroreduction of bismuth oxide double-walled nanotube templates, resulting in surfaces with a fragmented morphology [29]. They

specifically examined the impact of structural defects namely, 5-7 ring defects, mono-vacancies, and di-vacancies on the adsorption energy of *OCHO, a precursor to formate. The energy barriers of *OCHO on the ideal Bi (001) surface was determined to be +0.47 eV. In comparison, the energy barriers for *COOH (the precursor to CO) and *H (the precursor to H2) were considerably higher, at +1.2 eV and +0.97 eV, respectively. The introduction of a 5-7 ring defect reduced the energy barriers of *OCHO to +0.43 eV, while the presence of a mono-vacancy further decreased it to +0.37 eV [29]. Most strikingly, the energy barriers fell to +0.07 eV in the presence of a di-vacancy, indicating that structural defects greatly enhance the stability of *OCHO on Bi surfaces [29]. Additionally, the findings revealed that surface defects significantly affected the adsorption strength and stabilisation of intermediates, thereby lowering the energy barriers associated with the reaction. This catalyst demonstrated remarkable activity, selectivity, and stability, highlighting the broader significance of defect engineering in the design of catalysts.

1.4.2 Adjusting composition.

In addition to structural modifications aimed at enhancing catalytic performance, the adjustment of catalyst composition represents another important strategy. This approach includes the preparation of metal alloys and the combination of multiple materials, both of which will be discussed in detail in the following.

An alloy is generally defined as a material with metallic properties formed through the combination of two or more metals by specific synthesis methods. Depending on the number of constituent elements, alloys may be classified as binary, ternary, or multicomponent systems. Following extensive investigations into the electrocatalytic properties of single-element metals, it is a logical progression to examine how catalytic performance is modified when metals are combined. Consequently, alloy-based and bimetallic interface catalysts have

been widely explored in the context of electrocatalytic CO_2 reduction. For instance, Ren et al. reported the preparation of tin nanosheets decorated with bismuth nanoparticles via a three-step process involving hydrothermal, electrodeposition, and electroreduction [30]. Their study demonstrated that the alloy and bimetallic interface catalyst achieved a notably high formate faradaic efficiency of 90% and exhibited reduced energy barriers, with a comparison of these barriers between pure tin and the alloy presented.

1.5. Catalytic Properties of AQCs.

Building upon the general strategies for enhancing nano-catalyst performance in electrochemical CO_2 reduction, sub-nanometre atomic quantum clusters (AQCs), composed of only a few metal atoms, have emerged in recent years as a distinct and promising class of catalytic materials. Their unique physicochemical properties, which differ fundamentally from those of larger nanoparticles and bulk metals, arise primarily from their extremely high surface-to-volume ratio and their size being below the thermodynamic stability threshold. As a result, AQCs exhibit pronounced size-dependent electronic and structural characteristics, making them attractive building blocks for advanced nanostructures, nanoelectronics devices, and catalytic systems. Consequently, research into atomic clusters and nanoalloys remains highly active, with numerous studies devoted to their synthesis, stabilization, and detailed characterisation [31-34].

Metal-based clusters, particularly those composed of transition metals, have attracted considerable attention for two primary reasons. First, the interaction between partially filled d orbitals and outer s orbitals gives rise to complex electronic structures, making them study both scientifically significant and experimentally demanding. Moreover, achieving precise control over their synthesis remains a critical yet challenging requirement, as naked nanometals are

highly reactive and susceptible to trace contaminants, often leading to the unintended formation of oxides or carbides rather than well-defined pure metal clusters [35]. Second, these clusters show exceptional promise in optoelectronic and catalytic applications, including electrochemical processes relevant to CO_2 conversion. Notably, small metal clusters frequently exhibit a pronounced size-dependent gap between the highest occupied and lowest unoccupied molecular orbitals (HOMO–LUMO gap), which underpins their potential utility in luminescence [36], sensing [37], therapeutics [38], energy conversion [39], catalysis [40], and electrochemical applications [41,42].

Importantly, the physicochemical properties of AQCs can be systematically tuned by varying the choice of metal, adjusting intermetallic distances, and selecting appropriate support materials, thereby enabling optimization of their catalytic behaviour [43]. Such tunability offers distinct advantages for catalytic applications, including reduced activation energies, improved conversion efficiencies, and enhanced product selectivity. Moreover, AQCs often demonstrate high durability and increased resistance to common catalytic poisons, such as sulphur- and carbon monoxide–containing species, when compared with conventional catalysts [44]. These attributes make AQCs particularly attractive candidates for demanding electrochemical environments.

As the size of metal clusters approaches the Fermi wavelength (λ_f< 1 nm), entering the sub-nanometre regime, quantum confinement effects become dominant, leading to the discretisation of electronic energy levels and the emergence of a well-defined HOMO–LUMO gap. Under these conditions, electrons no longer exhibit the fully delocalised behaviour characteristic of bulk metals, and the clusters begin to display properties more commonly associated with non-metallic systems [45,46]. Consequently, the geometric structure, electronic configuration, and size-dependent properties of AQCs are intrinsically

interconnected and must be considered collectively when evaluating their catalytic performance.

1.6 Thesis Outline

This thesis is organised into the following six chapters.

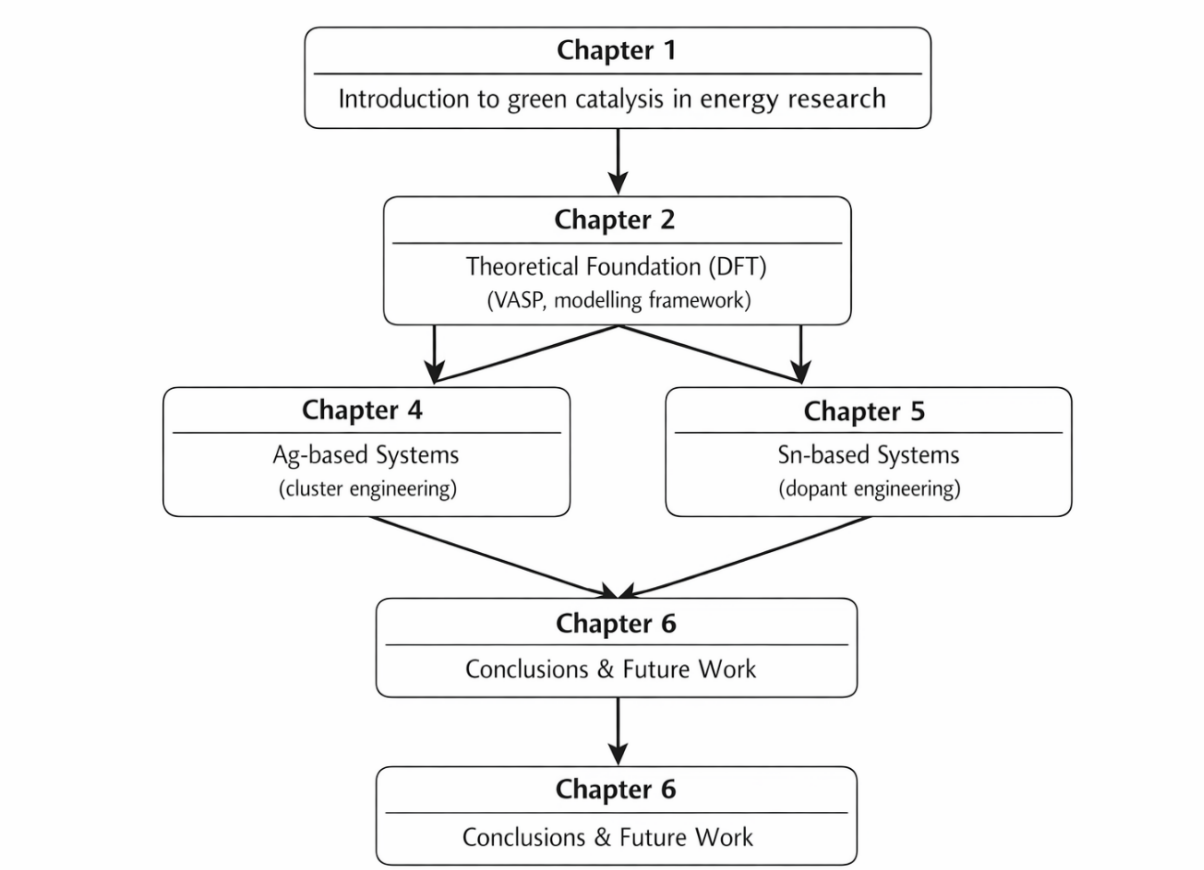

Figure 5. Schematic overview of the thesis structure and chapter interconnections.

Chapter 2 reviews the development of DFT, tracing the evolution of the theoretical frameworks that underpin the computational approaches employed in this thesis. The chapter provides the conceptual foundation necessary for understanding the electronic structure methods and modelling techniques used throughout this thesis.

Chapter 3 outlines the theoretical and computational methodology adopted in this research. It presents an overview of the Vienna ab initio Simulation Package (VASP) and its implementation using a plane-wave basis set. The chapter further details the procedures for geometry optimisation and introduces the key calculated quantities used to evaluate catalytic activity and selectivity, thereby establishing the framework for interpreting the results presented in the subsequent chapters.

Chapter 4 investigates the electrocatalytic reduction of carbon dioxide on silver-based systems, situating this study within the broader context of silver's established role as an efficient catalyst for carbon monoxide formation. Pristine silver surfaces and modified silver systems are examined to evaluate their influence on carbon dioxide activation and subsequent reduction. Density functional theory calculations are employed to model silver in the gas phase, under solvation conditions, and as surface-supported clusters of varying sizes.

The results demonstrate that the introduction of silver clusters significantly modifies the catalytic landscape. Five-atom clusters, exhibiting both two-dimensional and three-dimensional geometries, enhance the stabilisation of key reaction intermediates, while smaller three-atom clusters remain confined to surface sites yet still improve catalytic performance relative to pristine silver. In addition, the incorporation of gold clusters on silver surfaces further reduces reaction barriers, indicating a synergistic effect that promotes carbon monoxide formation. Overall, this chapter highlights the importance of structural and compositional control in tuning catalytic behaviour and identifies cluster engineering as an effective strategy for improving silver-based catalysts.

Chapter 5 examines the electrocatalytic reduction of carbon dioxide on tin-based systems, shifting the focus from surface-supported clusters to bismuth-doped tin substrates. Pristine tin surfaces and bismuth-modified tin systems are investigated to assess the impact of dopant

concentration and configuration on catalytic activity and selectivity. Density functional theory calculations are used to model tin surfaces doped with one to three bismuth atoms introduced through substitutional and adsorbed configurations.

The results reveal that increasing bismuth content significantly alters the catalytic behaviour of tin. Two primary reaction pathways are analysed: the carbon monoxide pathway involving the *COOH intermediate and the formic acid pathway involving *OCHO. Bismuth-doped tin surfaces are found to lower the energy barriers associated with both pathways, with notable improvements in activity and selectivity compared with pristine tin. Overall, this chapter demonstrates that controlled dopant incorporation is an effective strategy for tuning the catalytic performance of tin-based systems.

Chapter 6 summarises the key findings of the thesis and discusses their broader implications for catalyst design in electrochemical carbon dioxide reduction. The chapter also outlines potential directions for future research aimed at further improving activity, selectivity, and stability in next generation electrocatalysts.

2.Density Functional Theory

With the rapid advancement of computational technology, theoretical and computational approaches have become increasingly important for addressing complex chemical problems. Many materials, particularly composite materials, possess intricate internal structures that make it difficult to achieve a comprehensive understanding of their microscopic properties through experimental techniques alone. Computational simulation methods offer significant advantages in this context, providing valuable insights into material behaviour and enabling the prediction of macroscopic properties from atomistic models.

At the core of quantum chemical calculations lies the challenge of solving the Schrödinger equation, which allows the determination of fundamental molecular properties such as bond energies, geometric structures, and charge distributions. Theoretical methodologies therefore act as a crucial bridge between experimental observations and the intrinsic nature of molecular systems, playing an essential role in elucidating macroscopic material properties from a microscopic perspective. As a result, such methods have become indispensable tools in modern scientific research. Quantum chemical approaches include valence bond theory, molecular orbital theory, and DFT. Among these, DFT has emerged as the most widely used method due to its favourable balance between computational efficiency and accuracy, as well as its ability to treat systems containing a large number of atoms [46].

This chapter provides an overview of DFT, beginning with the fundamentals of the Schrödinger equation, followed by Hartree-Fock Theory, the Born–Oppenheimer approximation, the Hohenberg–Kohn theorems, and the Kohn–Sham formalism. The central principle of DFT is that the ground-state properties of a molecular or atomic system are uniquely determined by its electron density. Widely applied in physics and chemistry, DFT is a quantum mechanical approach for calculating the electronic structure of atoms, molecules, and solids [47]. Its

applications span a wide range of areas, including the prediction of molecular geometries, energetics, reaction mechanisms, optical properties, exchange interactions, and various spectroscopic techniques such as X-ray absorption, electron paramagnetic resonance (EPR), and Mössbauer spectroscopy [48].

In this work, calculations were performed using the Vienna Ab initio Simulation Package (VASP), which is based on density functional theory and employs the Kohn–Sham formalism to model systems containing many interacting particles. VASP was used to compute geometric and electronic structures as well as reaction energetics. This section therefore presents a concise overview of the theoretical foundations and mathematical formulation of DFT. More comprehensive treatments of DFT can be found in the works of Martin et al. and Koch et al. [49,50].

2.1 Schrödinger equation

The foundations of DFT are rooted in the Schrödinger wave equation, first proposed by Erwin Schrödinger in 1926 [51]. This equation describes the evolution of the wave function ψ over time, and its solution provides key insights into a system's fundamental properties, including energy, trajectory, and spatial configuration. The time-independent Schrödinger wave equation, in its most basic form, is expressed as follows:

$$\hat{H}\Psi = E\Psi \tag{2-1}$$

where the Hamiltonian operator is represented by $\hat{H}$, the wave function is depicted by Ψ, and E is the eigenvalue of the state's energy. Hamiltonian operator in classical mechanics comprises an operator for kinetic energy ($\hat{T}$) as well as an operator for potential energy ($\hat{V}$) given by

$$\hat{H} = \hat{T} + \hat{V} \tag{2-2}$$

Where $\hat{T}$ is expressed as $-\frac{\hbar^2}{2m}\nabla^2$. Therefore,

$$\hat{H} = -\frac{\hbar^2}{2m}\nabla^2 + \hat{V} \tag{2-3}$$

Here $\hbar$ is the Plank's constant in its reduced from given by $\hbar = \frac{h}{2\pi}$, m is the mass of an electron,$\hat{V}$ is the potential energy and ∇^2 denotes the Laplacian operator, expressed here in Cartesian coordinates as:

$$\nabla^2 = \frac{\partial^2}{\partial x^2} + \frac{\partial^2}{\partial y^2} + \frac{\partial^2}{\partial z^2} \tag{2-4}$$

For systems containing only a few electrons, solving the Schrödinger equation is both feasible and practical. However, when dealing with many body systems comprising multiple atoms and electrons the complexity of solving the equation increases significantly. In such cases, the system is described by the many-electron Schrödinger equation,

$$\left[-\sum_{i=1}^{N}\frac{\hbar^2}{2m}\nabla_i^2 + \sum_{i=1}^{N}V(r_i) + \sum_{i<j}\frac{e^2}{4\pi\varepsilon_0|r_i - r_j|}\right]\Psi(r_1, \dots, r_N) = E\Psi(r_1, \dots, r_N) \tag{2-5}$$

which explicitly accounts for electron–electron interactions and leads to a rapid increase in computational complexity. A fundamental goal of theoretical chemistry and physics is to develop methods for addressing the challenges associated with quantum many-body systems [52]. To tackle this complexity, various approximations have been introduced, which are discussed in the following sections.

2.2 Hartree-Fock Theory

The Hartree-Fock (HF) theory is one of the earliest and most fundamental approximations used to solve the many-electron Schrödinger equation [53]. It is a wavefunction-based method in which the complex many-body problem is simplified by assuming that each electron moves

independently in an average field created by all other electrons. This approximation transforms the many-electron problem into a set of effective one-electron equations.

In Hartree–Fock theory, the total electronic wavefunction is expressed as a single Slater determinant:

$$\Psi(x_1, x_2, \ldots, x_N) = \frac{1}{\sqrt{N!}} \begin{vmatrix} \psi_1(x_1) & \psi_2(x_1) & \cdots & \psi_N(x_1) \\ \psi_1(x_2) & \psi_2(x_2) & \cdots & \psi_N(x_2) \\ \vdots & \vdots & \ddots & \vdots \\ \psi_1(x_N) & \psi_2(x_N) & \cdots & \psi_N(x_N) \end{vmatrix} \tag{2-6}$$

Where $\psi_i(x)$ are spin-orbitals and x includes both spatial and spin coordinates. This determinant form ensures antisymmetric of the wavefunction and satisfies the Pauli exclusion principle [54]. Applying the variational principle to this wavefunction leads to the Hartree-Fock equations:

$$\hat{F}\psi_i = \varepsilon_i \psi_i \tag{2-7}$$

Where $\hat{F}$ is the Fock operator, defined as:

$$\hat{F} = \hat{h} + \sum_{j=1}^{N} (\hat{J}_j - \hat{K}_j) \tag{2-8}$$

Here, $\hat{h}$ is the one-electron Hamiltonian, while $\hat{J}_j$ and $\hat{K}_j$ represent the Coulomb and exchange operators, respectively. The Coulomb operator accounts for the classical electrostatic repulsion between electrons:

$$\hat{J}_j \psi_i(r) = \left(\int \frac{|\psi_j(r')|^2}{|r - r'|} dr' \right) \psi_i(r) \tag{2-9}$$

and the exchange operator arises from the antisymmetric of the wavefunction:

$$\hat{K}_j \psi_i(r) = \left(\int \frac{\psi_j^*(r')\psi_i(r')}{|r - r'|} dr' \right) \psi_j(r) \tag{2-10}$$

The Hartree-Fock equations must be solved iteratively using the Self-Consistent Field (SCF) method, as the Fock operator depends on the orbitals themselves. Starting from an initial guess, the equations are solved repeatedly until convergence is reached.

While Hartree-Fock theory successfully accounts for exchange interactions, it neglects electron correlation effects beyond this mean-field approximation. Consequently, it often overestimates the total energy of a system. Despite this limitation, HF theory provides an essential foundation for more advanced methods and serves as a reference point for both post-Hartree-Fock approaches and DFT.

2.3 Møller–Plesset Perturbation Theory (MP2/MP4)

Møller–Plesset (MP) perturbation theory [55] is a post-Hartree–Fock method used to account for electron correlation effects by applying many-body perturbation theory to the electronic Hamiltonian. In this approach, the Hartree–Fock solution is taken as the reference state, and the difference between the exact Hamiltonian and the Hartree–Fock Hamiltonian is treated as a perturbation.

The electronic Hamiltonian is partitioned as:

$$\hat{H} = \widehat{H_0} + \lambda \hat{V} \tag{2-11}$$

where $\hat{H}_0$ is the zeroth-order Hamiltonian (typically the sum of Fock operators), $\hat{V}$ is the perturbation, and λ is a bookkeeping parameter. The total energy is then expanded as a power series:

$$E = E^{(0)} + E^{(1)} + E^{(2)} + E^{(3)} + E^{(4)} + \ldots \tag{2-12}$$

In this expansion, $E^{(0)} + E^{(1)}$ corresponds to the Hartree-Fock energy, while higher-order terms account for electron correlation. The second-order Møller–Plesset correction (MP2) is the lowest-order term that includes electron correlation and is given by:

$$E^{(2)} = \sum_{i<j}^{occ} \sum_{a<b}^{virt} \frac{|\langle ij \,||\, ab \,\rangle|^2}{\varepsilon_i + \varepsilon_j - \varepsilon_a - \varepsilon_b} \quad (2\text{-}13)$$

where i, j denote occupied orbitals, a, b denote virtual orbitals, ε are orbital energies, and $|\langle ij \,||\, ab \,\rangle|$ are ant symmetrized two-electron integrals. The MP2 method provides a relatively inexpensive way to include dynamic electron correlation and is widely used due to its favorable balance between accuracy and computational cost.

Higher-order corrections, such as MP4, include additional terms up to fourth order in the perturbation expansion. These contributions improve the accuracy of energy by incorporating more complex electron correlation effects, including interactions involving multiple excitations. However, MP4 calculations are significantly more computationally demanding and are less commonly used in practice compared to MP2. Although Møller–Plesset perturbation theory improves upon Hartree-Fock results, it has limitations, including potential divergence in certain systems and sensitivity to the quality of the Hartree-Fock reference. Nevertheless, MP2 remains an important and widely applied method for capturing electron correlation in molecular systems.

2.4 Coupled Cluster Theory

Coupled Cluster theory is a highly accurate wavefunction-based method used to describe the electronic structure of many-electron systems [56]. It is considered one of the most reliable approaches in quantum chemistry for incorporating electron correlation effects beyond the Hartree-Fock approximation. Unlike Hartree-Fock theory, which neglects dynamic electron correlation, coupled cluster methods systematically include these effects through an exponential ansatz for the wavefunction.

In Coupled Cluster theory, the correlated many electron wavefunction is expressed as:

$$|\Psi_{CC}\rangle = e^{\hat{T}} |\Phi_0\rangle \quad (2\text{-}14)$$

where $|\Phi_0\rangle$ is a reference wavefunction, typically taken as the Hartree-Fock Slater determinant, and $\hat{T}$ is the cluster operator. The cluster operator is defined as a sum of excitation operators:

$$\hat{T} = \hat{T}_1 + \hat{T}_2 + \hat{T}_3 + \cdots \tag{2-15}$$

Here, $\hat{T}_1$, $\hat{T}_2$, and $\hat{T}_3$ represent single, double, and triple excitation operators, respectively. In practical calculations, the expansion is truncated at a certain level. The most used approximation is CCSD, which includes single and double excitations, and CCSD(T), which adds a perturbative treatment of triple excitations. The coupled cluster equations are derived by projecting the Schrödinger equation onto excited determinants:

$$\langle \Phi_i^a | \hat{H} e^{\hat{T}} | \Phi_0 \rangle = 0 \tag{2-16}$$

where $|\Phi_i^a\rangle$ denotes singly excited determinants, and similar expressions exist for higher excitations. The energy of the system is obtained as:

$$E_{CC} = \langle \Phi_0 | \hat{H} e^{\hat{T}} | \Phi_0 \rangle \tag{2-16}$$

One of the key advantages of Coupled Cluster theory is its size-extensivity, meaning that the calculated energy scales correctly with the number of particles. This property makes CC methods particularly suitable for studying large systems and comparing energies across systems of different sizes.

Despite its high accuracy, coupled cluster theory is computationally demanding, with the cost increasing rapidly as higher excitation levels are included. Nevertheless, methods such as CCSD(T) are often referred to as the “gold standard” of quantum chemistry due to their excellent balance between accuracy and computational feasibility.

2.5 Born-Oppenheimer Approximation

The Born-Oppenheimer approximation [57] is a fundamental concept in quantum chemistry. It enables the separation of the motion of the nuclei and the motion of the electrons. When describing the electrons in a molecule, this approximation assumes the motion of the atomic nuclei can be neglected. This is based on the fact that the mass of an atomic nucleus is significantly larger than that of an electron. This substantial mass difference results in the nuclei moving much more slowly than the electrons. In my work, I applied this approximation in order to achieve more precise results. In general, the Hamiltonian operator for a many-body system consists of five distinct components.

$$\hat{\mathrm{H}} = \widehat{T_e} + \widehat{T_n} + \widehat{V_{nn}} + \widehat{V_{ee}} + \widehat{V_{ne}} \tag{2-17}$$

As depicted through the above equation, this Hamiltonian consists of two operators $\widehat{T_e}$ and $\widehat{T_n}$ for the kinetic energy of electrons and nuclei respectively. Similarly, the remaining three operators $\widehat{V_{nn}}, \widehat{V_{ee}}$ and $\widehat{V_{ne}}$ are the operators of potential energy for the repulsion between the nuclei, electronic and for nuclear-electronic attraction respectively.

Here $\widehat{T_e}$ denotes the kinetic energy operator of the electrons, which is expressed as:

$$\widehat{T_e} = -\sum_i \frac{\hbar^2}{2m_e} \nabla_i^2 \tag{2-18}$$

Furthermore, the nuclear component of the equation can be disregarded, as atomic nuclei is significantly heavier than electrons. This allows the nuclei to be treated as fixed in position relative to the moving electrons. The fourth part of equation (2-17) $\widehat{V_{ee}}$ is defined as the electron-electron interaction and sum of all potentials acting on a given electron position r_i by all other electrons at position r_j, which can be written by

$$\widehat{V_{ee}} = \frac{1}{2} \sum_{i \neq j} \frac{e^2}{4\pi\varepsilon_0} \frac{1}{|\boldsymbol{r_i} - \boldsymbol{r_j}|} \tag{2-19}$$

The last part of the equation (2-17) $\hat{V}_{ne}$ describes the interaction between electrons and nuclei, and it depends on the positions of electrons r_i, nuclei R_I, the nuclear potential υ_{nuc}, which is given by

$$\widehat{V_{ne}} = \sum_I \sum_i v_{nuc}(|r_i - R_I|) \tag{2-20}$$

Since only the electronic part of the molecular wave function is considered when solving the Schrödinger equation to determine the eigenvalue of electronic energy, the Hamiltonian is simplified as follows:

$$\widehat{H_e}\Psi(r_1, r_2, \dots) = E\Psi(r_1, r_2, \dots) \tag{2-21}$$

Although the Born-Oppenheimer approximation reduces the complexity of the system, solving equation (2-21) remains a challenge, even with modern supercomputers. DFT addresses this issue by representing physical quantities in terms of the ground-state electron density, providing a more computationally efficient approach to solving many-body quantum systems.

2.6 The Hohenberg-Kohn Theorems

The foundational principles of DFT were established through the seminal contributions of Hohenberg and Kohn in 1964 [58]. Their first theorem states that, apart from an additive constant, the external potential v_{ext} (r) is uniquely determined by the ground-state particle density n_0 (r). To have a better understanding for the first theorem, it can be considered there are two Hamiltonians H_a and H_b, which have the same ground-state density $\rho(r)$ but different external potentials v_a and v_b. The wavefunctions of them could be obtained through solving the Schrödinger equation, and for a non-degenerate system there is one solution of the Schrödinger equation that presents the ground state wave-functions Ψ_a and Ψ_b. In this context, the electron density is defined in terms of the many electron wavefunction as

$$\rho(r) = N\int |\Psi(\boldsymbol{r}, \boldsymbol{r_2}, \boldsymbol{r_3}, \dots, \boldsymbol{r_N})|^2 \, d\boldsymbol{r_2} \, d\boldsymbol{r_3} \cdots d\boldsymbol{r_N} \tag{2-22}$$

which is obtained by integrating over the coordinates of all electrons except one.

Since $\Psi_b$is not a ground state of Hamiltonian H_a, we have:

$$E_a < \langle \Psi_b | H_a | \Psi_b \rangle \tag{2-23}$$

Write

$$H_a = H_b + (V_a - V_b) \tag{2-24}$$

so

$$E_a < \langle \Psi_b | H_b | \Psi_b \rangle + \langle \Psi_b | V_a - V_b | \Psi_b \rangle \tag{2-25}$$

Since

$$\langle \Psi_b | H_b | \Psi_b \rangle = E_b \tag{2-26}$$

We get:

$$E_a < E_b + \langle \Psi_b | V_a - V_b | \Psi_b \rangle \tag{2-27}$$

Now convert the potential expectation value into a density integral:

$$\langle \Psi_b | V_a - V_b | \Psi_b \rangle = \int \rho(\boldsymbol{r})[v_a(r) - v_b(r)]dr \tag{2-28}$$

Hence

$$E_a < E_b + \int \rho(r)[v_a(r) - v_b(r)]dr \tag{2-29}$$

Similarly, using $\Psi_a$as a trial wavefunction for $\widehat{H}_b$,

$$E_b < \langle \Psi_a | H_b | \Psi_a \rangle \tag{2-30}$$

which gives

$$E_b < E_a + \int \rho(r)[v_b(r) - v_a(r)]dr \tag{2-31}$$

Adding together the two expressions (2-27) and (2-31) to obtain the equation as follows:

$$E_a + E_b < E_b + E_a + \int \rho(r)[v_a(r) - v_b(r)]dr + \int \rho(r)[v_b(r) - v_a(r)]dr \quad (2\text{-}32)$$

The two integrals cancel, so

$$E_a + E_b < E_a + E_b \quad (2\text{-}33)$$

This expression results in a contradictory inequality, demonstrating that no two external potentials, differing by more than a constant, can produce the same non-degenerate ground-state density. The second theorem of Hohenberg and Kohn establishes that a universal functional for the energy E[ρ] can be expressed in terms of the electron density. The ground state corresponds precisely to the global minimum of this functional. Furthermore, the external potential is uniquely determined by the density, and in turn, this potential uniquely defines the ground-state wavefunction. Consequently, all other physical observables of the system, such as the kinetic energy T of electrons, are also uniquely specified. The total energy E[ρ] of the system can therefore be formulated as a functional of the density, as expressed below:

$$E[\rho] = T[\rho] + E_{int}[\rho] + \int dr V_{ext}(r)\rho(r) \quad (2\text{-}34)$$

The first terms in this expression correspond to the kinetic energy and the internal electron-electron interactions, which are typically combined into a single functional as expressed below:

$$F_{HK}[\rho] = T[\rho] + E_{int}[\rho] \quad (2\text{-}35)$$

This combination is considered universal, as it depends solely on the charge density and remains unaffected by the external environment.

According to the first Hohenberg–Kohn theorem, the Hamiltonian of a system is uniquely determined by its ground-state density ρ_0, which in turn specifies the external potential $V_{\text{ext}}$and the corresponding ground-state wavefunction Ψ_0. Furthermore, by the variational principle, for any trial wavefunction Ψ, the expectation value of the Hamiltonian satisfies:

$$E_0 = \langle \Psi_0 | H | \Psi_0 \rangle < \langle \Psi | H | \Psi \rangle = E \quad (2\text{-}36)$$

Consequently, if the universal functional $F_{\mathrm{HK}}[\rho]$is known, the ground-state density is obtained by minimizing Eq. (2-29). This, in turn, allows for the determination of all ground-state properties of the system.

2.7 The Kohn-Sham Approach

The Kohn–Sham equation [59] describes a hypothetical system of non-interacting particles whose electron density matches that of a corresponding system with interacting particles [60]. As previously discussed, determining the ground-state density theoretically allows for the calculation of the ground-state energy. However, the exact functional form expressed in equation (2-34) remains unknown. Consequently, the terms $T[\rho], E_{int}[\rho]$ in equation (2-34) cannot generally be formulated explicitly as functionals of the density. To address this limitation, Kohn and Sham [59] proposed a solution in 1965 by substituting the original Hamiltonian with an effective Hamiltonian that describes non-interacting particles within an effective external potential. This potential is constructed to ensure that the ground-state density remains identical to that of the original interacting system [61,62]. As a result, the energy functional is expressed as follows:

$$E_{KS}[\rho] = T_{KS}[\rho] + \int drV_{ext}(r)\rho(r) + E_H[\rho] + E_{ec}[\rho] \tag{2-37}$$

Hence, T_{KS} is the kinetic energy of the non-interacting system, where the kinetic energy (T) in the equation (2-28) has been used for the interacting system. This difference is due to the exchange correlation functional E_{xc}, which will be explained later in equation (2-39). Also, E_H presents the Hartree function, and describes the electron-electron interaction using the Hartree-Fock method [53,63-64] as given by:

$$E_H[\rho] = \frac{1}{2}\iint \frac{\rho(r)\rho(r')}{|r-r'|} drdr' \tag{2-38}$$

The above equation represents an approximate version of internal interactions of the electrons E_{int}. So, the exchange correlation functional E_{ec} describes the differences between the exact and approximated solutions to the kinetic energy and the electron-electron interaction terms that defined as:

$$E_{xc}[\rho] = (E_{int}[\rho] - E_H[\rho]) + (T[\rho] - T_{KS}[\rho]) \quad (2\text{-}39)$$

The Kohn-Sham theorem simplifies the complex many-body problem by reformulating it as a set of non-interacting equations, provided that the exact exchange-correlation functional is known. Due to the theoretical framework of DFT, only ground-state properties can be accurately determined, including the ground-state energy, electron density, fictitious Kohn-Sham eigenvalues, and the overall ground-state electron configuration. However, DFT is not suitable for reliably calculating excited states, such as the lowest unoccupied molecular orbital, and consequently tends to underestimate band gaps in semiconductors. It is important to note that DFT remains an approximate method for determining ground-state properties, as the precise form of the exchange-correlation functional is unknown, necessitating the use of approximations.

The DFT simplifies the quantum mechanical many-electron ground-state problem by reformulating it as a set of self-consistent one-electron equations through the Kohn-Sham approach [65]. While this method is formally exact, practical calculations require an approximation of the exchange-correlation energy, $E_{xc}[\rho]$, as a functional of the electron density. Historically, the Local Density Approximation (LDA) has been the standard choice for this purpose [66]. Despite its simplicity, LDA provides realistic descriptions of atomic structures, as well as the elastic and vibrational properties of a wide range of systems. However, LDA lacks the accuracy required to reliably predict the energetics of chemical reactions, such as reaction enthalpies and activation energy barriers, often leading to an overestimation of binding energies in molecules and solids. Furthermore, there are numerous instances where

LDA incorrectly ranks molecular conformations or crystal bulk phases in terms of energetic stability, sometimes even yielding qualitatively inaccurate results [67,68].

More recently, Generalized Gradient Approximations (GGAs) have significantly improved upon these shortcomings [65,69], offering, for example, a more reliable description of energy barriers in the dissociative adsorption of hydrogen on metal and semiconductor surfaces [70]. Gradient-corrected (GGA) functionals extend LDA by incorporating both the local electron density and its spatial variation. Consequently, LDA and GGA remain the two most widely used approximations for exchange-correlation energy in DFT calculations. The following section provides a more detailed discussion of these two approaches.

2.8 Approximations for exchange-correlation functional

2.8.1 Local Density Approximation

Among the numerous approximation methods developed for determining exchange-correlation functionals, the Local Density Approximation (LDA) remains the simplest [71]. Researchers have long employed LDA by assuming a uniform or slowly varying local electron density within a system to approximate the exchange-correlation functional [66]. Despite its simplicity, LDA has been widely utilised for calculating complex atomic structures, as well as evaluating elastic and vibrational properties, and conducting solid-state calculations.

Within the LDA framework, the electron density is assumed to be locally smooth. The term "local" signifies that the exchange-correlation energy at a given point in a system depends solely on the electron density at that specific location.

Unless otherwise stated, all quantities are expressed in Hartree atomic units ($\hbar = m_e = e = 1$). The exchange-correlation energy within the LDA framework is expressed as follows:

$$E_{xc}^{LDA}[\rho] = \int dr\rho(r)\, E_{ec}^{HG}\big(\rho(r)\big) \tag{2-40}$$

Here E_{xc}^{HG} is a term representing the exchange-correlational energy of a homogenous electron gas evaluated at the local electron density $\rho(r)$ assuming that the system behaves locally as a uniform electron gas. E_{xc}^{HG} is further divided into two components, the exchange component E_x^{HG} and correlational component E_c^{HG}.

$$E_{xc}^{LDA}[\rho] = \int dr\rho(r)\left(E_x^{HG}\left(\rho(r)\right) + E_c^{HG}\left(\rho(r)\right)\right) \tag{2-41}$$

The exchange energy component in the above equation is given by

$$E_x^{HG} = -\frac{3}{4\pi}\sqrt[3]{3\pi^2\rho} \tag{2-42}$$

LDA is most accurate for systems in which the electron density varies slowly, such as simple metals. However, it has limitations in describing systems with rapidly varying densities, which has led to the development of the Generalized Gradient Approximation (GGA) within DFT. For spin-polarized systems, LDA is extended to the Local Spin Density Approximation (LSDA), where the exchange–correlation energy depends separately on spin-up and spin-down densities, $\rho\uparrow(r)$ and $\rho\downarrow(r)$.

2.8.2 Generalized Gradient Approximation

In most real systems, including molecular systems, the electron density is not uniform. Despite this, the Local Density Approximation (LDA) often provides reasonable results, particularly when the electron density varies slowly in space. However, its accuracy deteriorates in systems where the electron density changes rapidly. This limitation motivates the use of the Generalized Gradient Approximation (GGA), which represents a significant improvement over LDA in such cases. By incorporating the gradient of the electron density, GGA enables a more accurate description of exchange–correlation effects in systems with strongly non-uniform electron density. The exchange–correlation energy in GGA is expressed as follows:

$$E_{xc}^{GGA}[\rho(r)] = \int d(r)\rho(r)E_{xc}^{GGA}[\rho(r), |\nabla p(r)|] \tag{2-43}$$

GGA is a significantly improved approximation method compared to LDA, as it enables accurate calculations for many properties that LDA is unable to evaluate effectively. In this thesis, the GGA and Perdew-Burke-Ernzerhof (PBE) [69] will be used in all the presented calculations.

2.9 Van der Waals (VDW)

Although van der Waals (VDW) interactions are generally regarded as the weakest among intermolecular forces, with typical interaction energies—defined as the depth of the potential energy minimum—ranging from approximately 0.4 to 4 kJ/mol, they play an indispensable role across a variety of scientific disciplines, including physisorption, structural biology, polymer chemistry, and crystallography.. Nevertheless, conventional exchange-correlation functionals employed in DFT, such as the Generalised Gradient Approximation (GGA) and the Local Density Approximation (LDA), are inadequate for accurately describing these interactions, as neither framework incorporates terms to represent dispersion forces [72]. GGA-based models frequently produce repulsive potential energy surfaces that lack a true minimum, whereas LDA tends to over bind, particularly in the context of noble gas dimers [73,74].

The quantum-mechanical origin of VDW interactions lies in the correlation between temporary dipole fluctuations, which can arise even between electronically neutral atoms without overlapping electron densities. Existing exchange-correlation functionals, which typically depend on local electron density, its spatial gradient, and the kinetic energy density, are insufficient to capture the long-range nature of VDW contributions [73,74]. This inadequacy is largely attributable to the extended spatial reach of these interactions, which decay swiftly as the intermolecular separation increases [75]. Van der Waals interactions decay rapidly with separation, approximately as r^{-6}, and therefore become very weak at distances beyond a few ångströms. While there is no strict cutoff, their contribution decreases sharply with distance.

These interactions are also generally anisotropic, depending on molecular orientation, except in highly symmetric cases such as interactions between two noble gas atoms. In layered materials such as graphite, this rapid decay means that interlayer coupling is dominated by nearest-neighbour layers, with more distant layers contributing only weakly.

To mitigate these limitations, DFT calculations are frequently augmented with empirical dispersion corrections that compensate for the absent VDW interactions. Among the most widely adopted of these are the D2 and D3 schemes [76]. These approaches, grounded in empirical observations rather than first-principles theory, are formulated to enhance the predictive accuracy of DFT by incorporating both pairwise (two-body) and collective (multi-body) dispersion effects. The D2 correction, for instance, is explicitly constructed to account for these neglected interactions [75].

$$E_{vdW}^{D2} = -S_6 \sum_{j=1}^{N-1} \sum_{j>i}^{N} \frac{C_{6,ij}}{R_{ij}^6} f_d\left(R_{ij}\right) \tag{2-44}$$

N represents the number of atoms, S_6 is the notation for scaling factors, the number of interacting atoms is represented by i and j and $f_d\left(R_{ij}\right)$ is the damping function which is represented as follows:

$$f_d\left(R_{ij}\right) = \frac{1}{1+e^{-d\left(\frac{R_ij}{R_r}-1\right)}} \tag{2-45}$$

where R_{ij} is the interatomic distance and R_r is the sum of the van der Waals radii of atoms i and j. The parameter d controls the steepness of the damping function.

The third-generation dispersion correction to Density Functional Theory (DFT-D3), represents a substantial improvement over its predecessor, DFT-D2 [76]. This method is applicable to systems comprising any of the first 94 elements of the periodic table. Unlike DFT-D2, which

applies differing treatments to main-group elements and transition metals, DFT-D3 offers a unified approach across both categories. A key advancement of the DFT-D3 framework lies in its treatment of dispersion coefficients: these are no longer fixed but are instead fully flexible and system-specific. This adaptability allows the method to more accurately reflect the unique electronic and structural characteristics of individual molecular systems, thereby enhancing the precision and general applicability of dispersion force calculations [77]. The general expression for the D3 correction is as follows:

$$E_{vdW}^{D3} = -\frac{1}{2}\sum_{i\neq j}\sum_{n=6,8,10,..} S_n \frac{C_n^{ij}}{R_{ij}^n} f_{d,n}(R_{ij}) \tag{2-46}$$

An alternative approach for incorporating van der Waals (VDW) interactions within DFT entails the modification of the exchange-correlation energy (E_{xc}) through the application of a non-local VDW density functional. In this framework, the non-local correlation energy (E_{xc}^{nl}) is evaluated based on the DFT charge density and is computed iteratively until self-consistency is reached [78]. The total exchange-correlation energy (E_{xc}) within this formalism is expressed as follows:

$$E_{xc} = E_x^{GGA} + E_c^{LDA} + E_c^{nl} \tag{2-47}$$

Here, E_x^{GGA} represents the GGA exchange energy term, E_c^{LDA} represents the LDA correlation energy term, and E_c^{nl} represents the non-local dispersion energy term and can be expressed as follows

$$E_c^{nl} = \frac{1}{2}\int\int \rho(r_1)\Phi(r_1,r_2)\rho(r_2)d^3r_1 d^3r_2 \tag{2-48}$$

Here, $\Phi(r_1,r_2)$ where $\rho(r)$is the electron density and $\Phi(r_1,r_2)$is a nonlocal kernel describing the interaction between electron densities at positions $r_1$and r_2.

However, this method is computationally more demanding than the method described earlier. Several variations of DFT-D3 exist, which differ in the type of damping function employed. Zero damping variation also known as the Grimme's formulation involves the use of following damping function:

$$f_{d,n}^{D3(0)}(R_{ij}) = \left[1 + 6\left(\frac{R_{ij}}{S_{r,n}R_{0,ij}}\right)\right] \tag{2-49}$$

To account for van der Waals (VDW) interactions, this thesis employs the spin-polarised Perdew Burke Ernzerhof (PBE) functional in combination with the Becke Johnson (BJ) damping scheme, as implemented in Grimme's D3 methodology. The D3(BJ) damping function is defined as follows [79]:

$$f_{d,n}^{D3(BJ)}(R_{ij}) = \frac{R_{ij}^{n}}{R_{ij}^{n}+(\alpha_1 R_{0,ij}\alpha_2)^{n}} \tag{2-50}$$

This DFT-D3(BJ) approach was further re-parameterized to form the DFT-D3(BJ) approach, with parameterizing relying on non-equilibrium geometries [80].

A variety of software packages are available for conducting DFT calculations, with widely used options including Gaussian, ORCA, Quantum Espresso, VASP, and ABINIT. The most appropriate choice depends on the nature of the calculations and the specific properties under investigation. In the present study, the Vienna Ab initio Simulation Package (VASP) was employed to examine the electrochemical reduction of CO_2 (CO_2RR), owing to its efficient plane-wave implementation of DFT, use of the projector augmented-wave (PAW) method, and its suitability for modelling periodic systems such as catalytic surfaces. VASP employs a plane-wave basis set to represent electronic orbitals, which is particularly convenient for periodic systems, as plane waves naturally satisfy periodic boundary conditions, allow systematic convergence through a single cutoff parameter, and avoid basis set superposition errors. Additionally, when combined with the PAW method, they provide an efficient and accurate

description of electron–ion interactions. In contrast, localized basis sets such as Gaussian orbitals, while efficient for molecular systems, are less suitable for periodic systems and may introduce basis set superposition errors.

3. Computational Method

This chapter serves to introduce the Vienna Ab Initio Simulation Package (VASP), the principal computational tool employed for all structural optimizations and related calculations discussed throughout this thesis. VASP is a sophisticated software suite designed to solve the Schrödinger equation for interacting many-electron systems within the framework of DFT [81]. It enables a range of molecular modelling tasks such as geometric optimisation, electronic structure analysis, band structure computations, density of states evaluations and wave function investigations. In order to perform simulations using VASP, a set of input files must be prepared, which upon execution yield a series of output files. The structure and function of these files will be detailed in the subsequent section.

3.1 Input Files

There are four different files that are required for VASP as input. They are as follows:

3.1.1 INCAR

This file serves as the primary input for VASP, guiding the program to execute the specified tasks. It contains all the essential keywords necessary to carry out the computational procedures. In terms of format, each line within the input file typically follows the structure: a tag name, followed by an equal sign (=), and the corresponding value(s) assigned to that tag (tag = values). For example, in an INCAR file used for DFT calculations that include van der Waals interactions, the tag IVDW = (1–14) is used, where each numerical value corresponds to a different method for accounting for dispersion forces. Another illustrative tag is ISPIN = (1–2); a value of 1 indicates a non-spin-polarised calculation, while a value of 2 enables spin-polarised calculations.

3.1.2 POSCAR

The POSCAR file contains all the essential information regarding the positions of ions and the geometry of the crystal lattice. Each line within this file is designated for specific types of data. The first line is a comment line, which typically includes a brief description or title related to the calculation being performed. The second line specifies the overall scaling factor and atomic coordinate system. The third to fifth lines define the unit cell through three lattice vectors. The sixth line lists the chemical elements present in the system, while the seventh line indicates the number of atoms for each respective species. The eighth line provides information about the type of coordinates used either Direct or Cartesian and may also include the phrase Selective Dynamics. If Selective Dynamics is present, the atomic positions in the following lines are accompanied by T (true) or F (false) flags, indicating whether the atomic coordinates are allowed to relax during optimisation. In the absence of Selective Dynamics, it is assumed that all atomic positions are subject to optimisation.

3.1.3 POTCAR

The POTCAR file contains pseudopotential data for all the chemical species involved in the calculations. In cases where multiple elements are present, a combined POTCAR file must be constructed, incorporating the pseudopotentials for each species. Importantly, the order in which the pseudopotentials appear in the POTCAR file must correspond precisely to the order of the chemical species listed in the sixth line of the POSCAR file. The pseudopotentials will be described in the next section.

3.1.4 KPOINT

The KPOINTS file contains the coordinates and weights of the k-points used in the Brillouin zone sampling. Here, k-points refer to discrete wavevectors in reciprocal space at which the

electronic structure is evaluated, reflecting the fact that electronic states in a periodic crystal are described by Bloch's theorem. According to this theorem, a Bloch orbital takes the form:

$$\psi_{nk}(r) = e^{ik \cdot r} u_{nk}(r) \tag{3-1}$$

Where $\psi_{n\boldsymbol{k}}(\boldsymbol{r})$ is the electronic wavefunction, n is the band index, $\boldsymbol{k}$ is the wavevector (k-point), and $\boldsymbol{r}$ is the position vector. The term $e^{i\boldsymbol{k}\cdot\boldsymbol{r}}$ represents a plane wave, while $u_{n\boldsymbol{k}}(\boldsymbol{r})$ is a function that has the same periodicity as the crystal lattice. The file is structured over several lines, each serving a distinct purpose. The first line is a comment line, typically used to provide a title or brief description of the calculation. The second line specifies the total number of k-points or indicates whether automatic generation will be used. The presence of a non-blank character on the third line determines the type and centre of the k-point mesh. The subsequent lines define the subdivisions and shifts applied to the k-point grid: the fourth line specifies the number of subdivisions along each reciprocal lattice vector (N1, N2, N3), while the optional fifth line introduces a shift of the mesh by (S1, S2, S3) relative to the default centre grid.

3.2 Output Files

There are five files that are output form VASP. They are as follows:

3.2.1 OUTCAR File

This principal output file serves as the comprehensive repository for all computational data. It integrates information derived from multiple sources, including symmetry analysis and three essential input files: POSCAR, POTCAR, and INCAR. It further incorporates keywords specified in the INCAR file, as well as detailed data concerning the basis set, k-point sampling, and ionic coordinates. Additionally, it records the full sequence of electronic steps undertaken during the optimisation process, alongside data on local charges, magnetic moments, total energy, atomic forces, and computational timing.

3.2.2 OZICAR File

This file provides a simplified counterpart to the OUTCAR file, containing essential details pertaining to each electronic step. It presents the information in a more accessible format, facilitating straightforward interpretation of key computational results such as the total energy, changes in energy, and related quantities.

3.2.3 CHGCAR File

The CHG or CHGCAR file in VASP contains a detailed representation of the total charge density, incorporating both the valence electron density and, where applicable, the core charge density. It is generated at the conclusion of a calculation and is formatted similarly to the structural files, including lattice vectors and grid dimensions, followed by the real-space charge density values on a three-dimensional grid. This file is particularly valuable for post-processing analyses, such as Bader charge partitioning, charge density difference mapping, and visualization of electron distribution within the system.

3.2.4 DOSCAR File

The DOSCAR file contains data relating to the density of states (DOS) calculated. It provides information on the distribution of electronic states across different energy levels, which is essential for analysing the electronic structure and understanding the material's behaviour. The file includes total DOS as well as projected DOS onto individual atoms or orbitals, enabling detailed insight into the contribution of specific elements or states to the overall electronic properties. This information is particularly valuable when investigating phenomena such as band gaps, conductivity, and magnetic behaviour in materials.

3.2.5 CONTCAR File

The CONTCAR file contains the final atomic configuration of the system following the completion of a VASP calculation. Its structure is identical to that of the POSCAR file, listing the lattice vectors, atomic species, and atomic positions, typically in either direct or Cartesian coordinates. This file reflects the relaxed geometry of the system after ionic optimisation and can be readily used as input for subsequent calculations. It is particularly useful for examining structural changes during simulation and provides a reliable reference for further analysis of the system's physical or chemical properties.

3.3 Geometry Optimisation

Geometry optimisation refers to the process of locating a local minimum on the potential energy surface by minimizing the total energy of the system, thereby yielding the most thermodynamically stable atomic configuration at zero temperature and zero pressure. At finite temperature and pressure, the equilibrium configuration would instead be determined by minimising the Gibbs free energy. This step is essential, as neglecting it can lead to significant inaccuracies in the calculation of material properties such as defect energetics or electronic structure. In the present work, a conjugate-gradient algorithm (CGA) [82,83] is employed to iteratively relax the atomic positions by minimizing the forces acting on each atom. Within VASP, this is achieved by specifying the tag IBRION=2 in the input file. The CGA operates through a three-step cycle comprising initial, trial, and correction phases designed to efficiently approach the minimum energy configuration. Initially, the algorithm evaluates the energy and force landscape to determine the direction of steepest descent, updating the ionic positions accordingly. This process is iteratively continued, with new gradients computed at each step, until convergence is achieved. Convergence in the electronic self-consistent field (SCF) calculations is governed by an energy threshold of EDIFF = 10^{-4} eV, while structural relaxation

is controlled by a force convergence criterion of EDIFFG = −0.02 eV/Å, ensuring that the forces on all atoms fall below 0.02 eV/Å. This thesis adopts a plane-wave kinetic energy cut-off of 500 eV, and energy convergence has been tested with respect to k-point sampling. To accurately represent band occupations in large supercells, Gaussian smearing is introduced via the tag ISMEAR = 0, with a smearing width of SIGMA = 0.05 eV. In such systems, artificial interactions between periodic images, particularly along the vacuum direction, can lead to spurious electrostatic effects. These are mitigated using a dipole correction (IDIPOL = 3), which removes the artificial interaction between periodically repeated dipoles. The associated correction to the total energy can be expressed as:

$$E_{\text{dipole}} = \frac{2\pi}{\Omega} \mid \mathbf{p} \mid^2 \tag{3-2}$$

Where **p** is the dipole moment of the supercell and Ω is its volume. It should be noted that this approach differs from the Makov-Payne correction, which is typically applied to charged defect calculations.

3.4 Vibrational frequency analysis

In computational chemistry, vibrational frequency analysis is employed to investigate the dynamic behaviour of molecules by calculating their vibrational modes. Using DFT implemented in VASP, researchers can gain insight into the vibrational properties of molecular systems, thereby enhancing understanding of their stability, reactivity, and other thermodynamic characteristics. The thermodynamic properties of a system describe its physical behaviour in relation to temperature, pressure, and other state variables. In this thesis, the VASPKIT package was used to determine the zero-point energies and entropy contributions to the free energy at room temperature (298.15 K) through vibrational frequency analysis. The free energy of the electrochemical system is then evaluated as the sum of the static-nucleus (electronic) energy and the vibrational free energy contribution:

$$G = E_{DFT} + F_{vib} \tag{3-3}$$

Where E_{DFT} is the total energy obtained from DFT optimization, and F_{vib} includes the zero-point energy and entropy contributions derived from vibrational frequency analysis.

The computed Gibbs free energies are further used to evaluate reaction kinetics within the framework of transition state theory (TST) [84]. According to TST, the rate constant of a chemical reaction is determined by the free energy barrier between reactants and the transition state:

$$k = \frac{k_B T}{h} \exp\left(-\frac{\Delta G^{\ddagger}}{RT}\right) \tag{3-4}$$

Where k_B is Boltzmann's constant, $\Delta G^{\ddagger}$ is the Gibbs free energy of activation, defined as the difference between the free energy of the transition state and that of the reactants. Thus, vibrational frequency analysis not only provides thermodynamic properties but also enables the prediction of reaction rates.

3.5 VASPKIT

In recent years, the development of robust post-processing tools has become increasingly important in the field of computational materials science, particularly for streamlining workflows associated with first-principles calculations. One such tool, VASPKIT [85], has emerged as a widely adopted open-source utility that significantly enhances the usability of data generated from the Vienna Ab initio Simulation Package (VASP). Designed to operate through both a menu-driven interface and a command-line mode, VASPKIT provides a flexible environment for the manipulation and analysis of input and output files. Its capabilities span a broad range of tasks, including the generation of high-symmetry k-point paths for band structure calculations, extraction of density of states (DOS) and charge density data, and band structure plots. For researchers working with complex systems such as defective crystals,

surfaces, or low-dimensional materials, the ability to construct supercells or slab models directly within the VASPKIT framework is especially valuable. Moreover, the tool simplifies the interpretation of electronic and optical properties by offering straightforward access to quantities such as the dielectric function, local potential, and electrostatic difference maps. By removing the need to manually parse large and often cumbersome output files like OUTCAR or vasprun.xml, VASPKIT not only reduces the probability of human error but also accelerates the research cycle. Its compatibility with popular visualization software, such as VESTA, further enhances its utility in both qualitative and quantitative analysis. In this study, VASPKIT has been employed extensively for the density of states, the examination of charge distribution, and the thermodynamic properties. Its role in bridging the gap between raw DFT data and meaningful physical interpretation cannot be overstated, particularly in large scale or high throughput investigations where efficiency and accuracy are paramount.

3.6 Solvation correction

VASPsol provides an implicit approach to modelling solvation within VASP software, allowing the influence of a polar medium and any dissolved ions to be represented without the explicit inclusion of solvent molecules [86,87]. In this framework, the solvent is described as a continuum dielectric whose spatial distribution is determined self-consistently from the electronic density of the solute, thereby defining a smooth solute–solvent interface without the need for predefined cavities. The electrostatic potential is obtained by solving a modified Poisson equation in which the dielectric permittivity varies in space, accounting for the polarization response of the solvent. In addition, non-electrostatic contributions such as cavitation and dispersion interactions between the solute and solvent are incorporated through parametrized terms. Building on this description, the more recent formulation further includes the effect of mobile ions by coupling the electrostatics to a Poisson–Boltzmann-type treatment, in which ionic charge densities respond to the local electrostatic potential. This extension

enables the description of electrolyte environments and interfacial screening effects relevant to electrochemical systems. Through its treatment of electrostatic screening, interfacial effects, and solute–solvent dispersion interactions, the method provides an efficient route to account for environmental contributions in large periodic systems, including metallic and semiconducting surfaces. The implementation is fully compatible with VASP's existing ultrasoft and projector-augmented wave pseudopotential frameworks, enabling solvation effects to be incorporated with minimal departure from standard computational practice.

To ensure that calculations employing the VASPsol implicit solvation model proceed in a stable and reproducible manner, the work was organized into a three-stage directory structure. Each stage corresponds to a discrete part of the computational workflow and is intended to separate geometry optimisation from the generation of charge densities and, finally, from the solvation calculation itself.

The first directory contains a conventional gas-phase relaxation of the structure (relax_gas). This step is carried out without the solvation model enabled, allowing the geometry to converge without any influence from the solvent cavity. Once this optimisation was completed, the resulting CONTCAR file was transferred to a second directory (sol) and used as the input geometry for a single-point calculation. The sole purpose of this intermediate step was to produce a well-converged WAVECAR file, as VASPsol requires an electron density reference to define the implicit solvent cavity.

The final stage of the workflow was placed in a separate directory (thermo_sol), which contained the structural files from the preceding step alongside the WAVECAR. Here, the solvation model was activated in the INCAR file by enabling LSOL together with the chosen dielectric parameters. Keeping this stage isolated helped to maintain a clear record of the solvation-specific settings and ensured that results could be traced unambiguously to their

corresponding inputs. This structured approach also facilitated post-processing, as each directory reflected a logical phase of the calculation and could be inspected or repeated independently if required.

3.6 Density of states

The electronic density of states (DOS) is a fundamental quantity for analyzing the electronic structure of a system, particularly in simulations performed using VASP [88-90]. It describes the distribution of available electronic states as a function of energy. At zero temperature, states below the Fermi level are considered occupied, while those above it are unoccupied. In bulk materials, the DOS per unit volume at a given energy can be formally expressed as:

$$\frac{1}{V} \cdot \frac{N(E+\Delta E)-N(E)}{\Delta E} = \frac{1}{V} \cdot \frac{dN(E)}{dE} \tag{3-5}$$

For free electron gas, this becomes

$$\frac{1}{V} \cdot \frac{dN(E)}{dE} = \frac{1}{2\pi^2}\left(\frac{2me}{\hbar^2}\right)\sqrt{E} \tag{3-6}$$

where V is the volume of the cell, E is the energy of the system, $N(E)$ is the cumulative number of single-particle energy eigenvalues with energies less than or equal to E . Here, m is the electron mass and $\hbar = \frac{h}{2\pi}$ where h is Planck's constant. The total DOS can be defined as the sum of the band contributions at a certain eigenvalue. The DOS is disintegrated into the projected DOS (PDOS) based on the individual contributions of atoms included in the system. It is important to note that the calculations made by the Vaspkit software for all the DOS numbers that are displayed automatically shift the Femi energy level to zero eV.

3.7 Pseudopotentials

In plane-wave implementations of DFT, a key limitation arises from the need for a very large number of plane waves—often exceeding 10,000—to accurately describe the rapid oscillations

of electronic wave functions in the core region. This significantly increases the computational cost of electronic structure calculations. However, the physical and chemical properties of most systems are primarily governed by valence electrons, while core electrons play a relatively minor role. To reduce computational demands, the all-electron problem can therefore be simplified by replacing the strong nuclear potential and core electrons with a weaker, effective potential acting only on valence electrons. These effective potentials are known as pseudopotentials (PSPs). This approach, commonly referred to as the pseudopotential approximation [91-94], replaces the complex core potential with a smoother alternative. As a result, the true, highly oscillatory wave functions in the core region can be substituted with smoother pseudo-wavefunctions, enabling a significant reduction in computational effort while preserving the essential physical characteristics of the system [95]. A visual comparison between the core and pseudo wave functions is presented in Fig 5 [94].

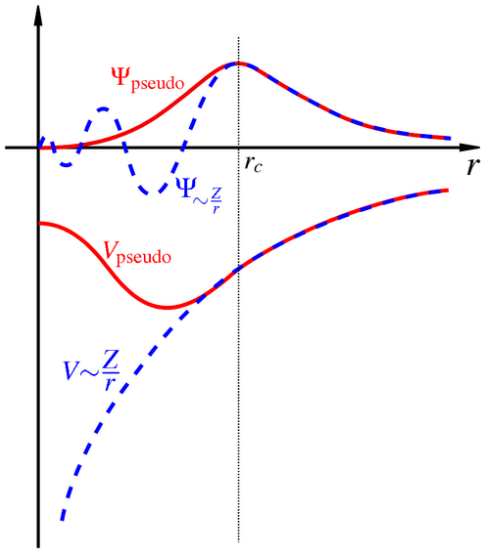

Fig.5 Schematic illustrations of the real wavefunction (Ψ_v), pseudo-wavefunction (Ψ_{pseudo}), and their corresponding potential and pseudopotential [94]. r_c is the radius where the core-wavefunction and pseudo-wavefunction meet.

An alternative to the use of pseudopotentials (PSPs) is the projector augmented wave (PAW) method, introduced by Blöchl [96], which enables the generation of even smoother wave functions in the vicinity of atomic nuclei. The PAW approach incorporates auxiliary localised functions, similar in spirit to the 'ultrasoft' pseudopotential technique, and as a result, much of its computational framework mirrors that of standard pseudopotential calculations. A defining feature of the PAW formalism is its transformation of the rapidly oscillating valence wave functions, denoted by Ψ, near the core region into a set of smooth auxiliary functions, $\widetilde{\Psi}$. This transformation lies at the heart of the PAW method and allows for an efficient yet accurate representation of electronic behaviour near atomic centers. If Ψ represents the valence wave function fluctuating at a fast rate in the vicinity of the nucleus, and $\widetilde{\Psi}$ represents several smooth auxiliary functions, then they can be interconverted as follows:

$$\Psi = \mathrm{T}\widetilde{\Psi} \tag{3-7}$$

$$\mathrm{T} = \mathrm{I} + T_0 \tag{3-8}$$

Furthermore, T_0 can be expanded as:

$$T_0 = \sum_R T_R \tag{3-9}$$

where R are non-overlapping spheres positioned around the atoms. To obtain the real wave function formula, the real and auxiliary wave functions are expanded as linear combinations of plane waves within the spheres R as [96]:

$$|\Psi\rangle = |\widetilde{\Psi}\rangle + \sum_n C_n \left(|\phi_n\rangle - |\widetilde{\phi}_n\rangle\right) \tag{3-10}$$

where $|\phi_n\rangle$ and $|\widetilde{\phi}_n\rangle$ are the all-electron and pseudo partial waves, respectively.

By introducing projector functions $\langle \tilde{p}_n |$, the coefficients C_n are defined as [96]:

$$C_n = \langle \tilde{p}_n | \widetilde{\Psi} \rangle$$

which leads to the standard PAW reconstruction formula:

$$|\Psi\rangle = |\widetilde{\Psi}\rangle + \sum_n \left(|\phi_n\rangle - |\widetilde{\phi}_n\rangle\right) \langle \widetilde{p}_n | \widetilde{\Psi}\rangle \tag{3-11}$$

Accordingly, the transformation operator can be written as:

$$T = I + \sum_n \left(|\phi_n\rangle - |\widetilde{\phi}_n\rangle\right) \langle \widetilde{p}_n | \tag{3-12}$$

The expectation value of an operator A is then evaluated using [96]:

$$\langle A \rangle = \langle \widetilde{\Psi} | T^{\dagger} A T | \widetilde{\Psi} \rangle \tag{3-13}$$

Finally, the total energy can be expressed as a sum of a smooth contribution and atom-centred corrections:

$$E = \tilde{E} + \sum_R \left(E_R^1 - \widetilde{E_R^1}\right) \tag{3-14}$$

In conclusion, the PAW method offers a significant improvement over the conventional pseudopotential (PSP) approach, particularly in terms of the transferability and accuracy required for reliable electronic structure calculations. Owing to these advantages, the PAW method has been employed throughout this thesis to investigate surface interactions.

3.8 Bader Charge Analysis

In this work, DFT is employed to calculate the electronic charge density. Bader charge analysis is used as a powerful tool to elucidate the electronic structure of both molecular and solid-state systems and occupies an important role in theoretical and computational chemistry. The concept of atomic charges is widely applied to interpret chemical reactivity and structural variations [97]. Within this approach, the electron density, denoted as $\rho(x, y, z)$, obtained from plane-wave DFT calculations, is analysed as a continuous function of three spatial coordinates. In such systems, atomic nuclei act as localised centres of attraction surrounded by an electron

cloud. The charge density reaches its maximum at the nuclear positions and gradually decreases with increasing distance from the nuclei.

Henkelman and colleagues [98-100] proposed an efficient, grid-based algorithm for the Bader decomposition of electron density. This method employs steepest-descent trajectories, constrained to the grid points, to delineate the Bader regions. In the so-called near-grid scheme, a grid point is identified by the indices (i, j, k), and from this point a trajectory of steepest ascent is traced in the direction of increasing charge density gradient ($\nabla\rho$), which is computed along the direction $\hat{r}$ as follows:

$$\nabla\rho(i,j,k)\cdot\hat{r}(di,dj,dk)=\frac{\Delta\rho}{|\Delta\vec{r}|} \tag{3-15}$$

3.9 Adsorption energy

Accurately determining the adsorption energy is of fundamental importance in catalyst research, as it influences both selectivity and catalytic activity. DFT facilitates reliable calculations of adsorption energies and provides insight into the strength of interactions between catalyst surfaces and adsorbate molecules. Such calculations, which often incorporate periodic boundary conditions and dispersion corrections, underpin rational catalyst design, optimisation, and the elucidation of reaction mechanisms. They are also instrumental in predicting catalyst deactivation (poisoning) and in developing durable catalysts with extended operational lifetimes.

Overall, the calculation of adsorption energy is essential for understanding and controlling catalyst adsorbate interactions, thereby advancing catalysis research and contributing to the development of more efficient and sustainable industrial processes. The adsorption energy is obtained using the following equation:

$$E_{ads}=E_{AB}-E_A-E_B \tag{3-16}$$

where E_{AB} is the total energy of the complex two systems, E_A represents the total energy of optimised system A, and E_B represents the total energy of optimised system B. From the definition of adsorption energy, a negative value represents a stable adsorption mechanism. According to this definition, a negative adsorption energy indicates a thermodynamically stable adsorption process. It should be noted that this definition corresponds to adsorption energies calculated at 0 K from DFT total energies. At finite temperatures, adsorption is more accurately described by the Helmholtz free energy, which includes entropic contributions. In practice, finite-temperature corrections may include zero-point energy (ZPE), vibrational contributions, and entropy terms.

4. Electrochemical reduction of CO_2 on silver substrate

In this chapter, DFT calculations are employed to investigate the electrocatalytic reduction of carbon dioxide to carbon monoxide on the Ag (111) surface, considering both gas-phase and solvated environments. As mentioned in chapter 1, electrochemical CO_2 reduction offers a promising route for mitigating greenhouse gas emissions while simultaneously enabling the conversion of carbon dioxide into value-added chemicals and fuels using renewable electricity. As such, the development of efficient and selective CO_2 reduction catalysts is of considerable importance for sustainable energy and carbon recycling technologies. By examining a range of atomically defined metal clusters supported on Ag (111), including Ag_5, Ag_3, Au_5, and Au_3, this study evaluates how cluster composition and size influence catalytic activity. The results demonstrate that these surface clusters play a pivotal role in modifying reaction energetics, leading to a significant reduction in the energy barriers associated with the CO_2-to-CO pathway. This reduction in activation barriers indicates enhanced catalytic efficiency and highlights the potential of cluster-modified silver surfaces for improved CO_2 conversion. Overall, these findings provide fundamental insights into CO_2 electroreduction mechanisms and offer a valuable framework for the rational design of advanced electrocatalysts in future studies.

4.1 Introduction

The imperative to reduce carbon dioxide (CO_2) emissions, to convert solar and wind energy into chemical energy, and to advance the commercial utilization of CO_2 has driven considerable research into its reduction to carbon monoxide (CO) or hydrocarbons. Electrochemical reduction of CO_2 represents a promising route; whereby waste emissions can be transformed into alternative hydrocarbon fuels [101]. However, owing to the exceptional thermodynamic and kinetic stability of CO_2, efficient catalysis is essential, requiring catalysts that are both highly active and stable under operating conditions. Two key parameters define an effective electrocatalyst: high selectivity, which ensures preferential formation of the desired product, and high activity, which enhances reaction rates.

A wide range of metal electrocatalysts, including silver (Ag) [101], gold (Au) [102], gallium (Ga) [103], palladium (Pd) [104], and zinc (Zn) [105] have been investigated for the carbon dioxide reduction reaction (CO2RR). Many of these materials exhibit high selectivity and activity, often producing syngas (a controlled mixture of CO and H_2) depending on the applied potential and type of materials. The influence of crystallographic facets on electrocatalytic performance has long been recognised, and achieving optimal selectivity and activity requires precise identification and optimisation of the catalytically active sites.

Although silver has been extensively examined [106-112], its catalytic efficiency remains limited and its cost is non-negligible. Notably, noble metals with carefully engineered architectures and reduced loadings can exhibit superior catalytic performance compared with bulk counterparts. Silver is particularly attractive for CO production because it is less expensive than gold and palladium and preferentially reduces CO_2 to CO. However, surface defects and structural heterogeneity can significantly affect its activity. The concept of active sites, first proposed by Taylor (1925) [113], suggests that only a small fraction of the specific surface atoms or groups of atoms located at edges, corners, or defects is catalytically active.

Consequently, considerable effort has been devoted to identifying and exploiting such surface features to enhance catalytic efficiency, including the use of atomic quantum clusters (AQCs) and metal nanoparticles.

Interest in metal clusters was revitalised in the 1980s following the discovery of pronounced size-dependent physical and chemical properties [114-116]. The unusual catalytic behaviour of small noble metal particles subsequently became a major research focus and remains an active field of study [117]. Metal clusters often acquire charge through electron transfer to a support surface, such as a metal oxide, while free clusters can be investigated through electron attachment or ionisation. A detailed understanding of the interaction between small molecules and cluster surfaces, as well as their associated reactivity, is therefore essential.

Atomic quantum clusters (AQCs), which exhibit molecule-like electronic structures at the sub-nanometre scale, possess discrete energy levels and a HOMO–LUMO gap comparable to that of molecular systems. Unlike larger nanoparticles, they do not exhibit plasmonic behaviour, endowing them with unique chemical and physical properties suitable for advanced catalytic applications [114]. Studies of such clusters and nanoalloys have provided valuable insights into size-dependent structural, energetic, and reactive properties, with gas-phase investigations offering benchmark thermodynamic data for validating theoretical models.

Despite extensive experimental and theoretical efforts, the fundamental mechanisms governing highly efficient electrochemical CO_2 reduction remain incompletely understood. DFT has emerged as an indispensable tool for elucidating the relationships between geometric structure, electronic properties, and catalytic performance. In this thesis, DFT-based investigations are employed to examine silver surfaces modified with gold and silver clusters, with particular emphasis on the role of cluster size in modulating electrocatalytic activity and selectivity.

4.2 Computational approach.

DFT calculations were performed using the Vienna Ab initio Simulation Package (VASP) [90] to determine both the electronic and geometrical properties of the system, both in the absence and presence of atomic quantum clusters (AQCs). The predominant surface of silver corresponds to its most exposed close-packed (111) facet. To model face-centred cubic bulk silver, the lattice parameter was initially taken as 4.12 Å, which closely matches the experimental value of 4.09 Å [118,119]. For accurate calculations, the Brillouin zone was sampled using a 12 × 12 × 12 k-point mesh. The construction of the surface slab followed the methodology proposed by Ong et al. [120] and employed the VESTA software [121] for visualization and geometrical setup, while all images were generated using Jmol [122].

The Ag (111) surface was modelled as a (5 × 5) four-layer slab with lateral dimensions 14.36 × 12.43 Å, and a vacuum spacing of 20 Å in the z-direction to eliminate interactions between periodic images, as illustrated in Figure 6A. Convergence tests with respect to both the in-plane supercell size and the vacuum thickness were performed, and variations in adsorption energies were found to be less than 0.02 eV, confirming that the chosen slab model effectively minimises interactions between periodic images. During structural optimisation, the top three atomic layers were allowed to relax, while the bottom layer was fixed at the bulk positions. For relaxation of the surface structures, a kinetic energy cut-off of 500 eV was employed, and the Brillouin zone was sampled using a 3 × 3 × 1 k-point mesh, as specified in Figure 6B. Total energies and geometry optimisations were carried out within the Generalised Gradient Approximation (GGA) using the Perdew–Burke–Ernzerhof (PBE) exchange–correlation functional [69]. London dispersion interactions were accounted for by employing the Becke–Johnson damping method [83], within a spin-polarised DFT framework. The electronic self-consistency was converged to within 10^{-4} eV [123], and the forces were relaxed to below 0.02

eV/Å. Bader charge analysis was carried out using the code developed by the Henkelman group [98-100].

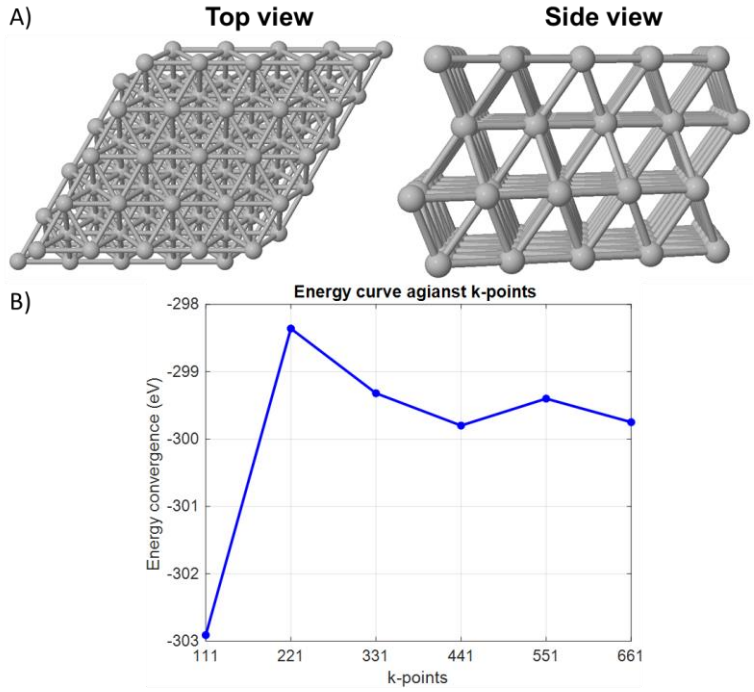

Fig 6. The optimised structures of the Ag (111) and the energy convergence vs k-points.

However, the density of states and thermodynamic properties at standard room temperature and pressure were evaluated using the open-source command-line program VASPKIT [85]. Gibbs free energy at 298.15 K and 1 atm was also calculated with

$$G = E_{DFT} + E_{ZPE} + \int_0^{298.15} C_v \, dT - TS \qquad (4\text{-}1)$$

where E_{DFT} is the total energy obtained from DFT optimization, E_{ZPE} is total vibrational zero-point energy, C_v is the heat capacity at constant volume, T is the temperature, and S is the entropy. The pV term is negligible under standard conditions and was therefore omitted. Moreover, to evaluate the thermodynamic stability of the heterostructures of Ag and molecules the adsorption energy was calculated according to Eq. (3–16). According to this definition, negative adsorption energies correspond to thermodynamically stable adsorption configurations.

The CO pathway reaction mechanism, underlying the transformation of CO_2 into CO is suggested to involve three fundamental steps, which are represented by the equations below.

$$CO_{2(aq)} + * + H_{(aq)}{}^{+} + e^{-} \leftrightarrow * COOH \quad (4\text{-}3)$$

$$* COOH + H^{+}_{(aq)} + e^{-} \leftrightarrow * CO + H_2O \quad (4\text{-}4)$$

$$* CO \leftrightarrow CO_{(aq)} + * \quad (4\text{-}5)$$

where a lone asterisk (*) denotes a surface site and an * symbol before a molecule denotes an adsorbed species. Figure 7 showing that mechanism on Ag (111).

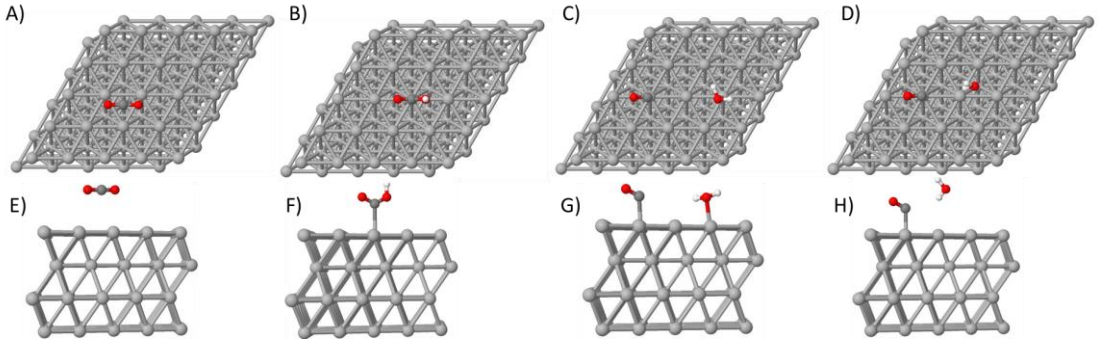

Fig. 7 Geometrical configurations of adsorption for CO pathway on pure Ag (111). (A)-(D) are the top view for the $*CO_2$, *COOH, $*CO+H_2O$ and $*+CO+H_2O$, respectively. (E)-(H) are the side view for $*CO_2$, *COOH, $*CO+H_2O$ and $*+CO+H_2O$, respectively. * Represents the metal surface and adsorption site of surface species. The Ag, O, C, and H atoms are represented with grey, red, dark grey, and white spheres, respectively.

The hydrogen evolution reaction (HER) was employed as a fundamental process for producing molecular hydrogen (H_2) through the electrochemical reduction of protons, which are represented by the equation below.

$$H_{(aq)}{}^{+} + e^{-} \leftrightarrow \frac{1}{2} H_2(g) \quad (4\text{-}6)$$

Finally, having generated the diagrams and output files for the CO_2 reduction reaction (CO_2RR) on pristine Ag (111) in the gas phase, the corresponding diagram for the solvated phase was constructed by employing an appropriate solvation model [86,87]. This entire procedure was

subsequently repeated for the other surfaces studied, namely Ag_5/Ag (111), Ag_3/Ag (111), Au_5/Ag (111) and Au_3/Ag (111).

4.3 Results and discussion

4.3.1 Pure Ag (111)

The geometric and electronic configurations of reaction intermediates play a pivotal role in determining the behaviour of the CO_2 reduction reaction (CO_2RR) on pure silver surfaces. As illustrated in Figure 8A, the Ag (111) surface offers four distinct adsorption sites: the fcc hollow site, which is the threefold hollow site over a third-layer Ag atom; the hcp hollow site over a second-layer Ag atom; the top and the bridge sites. A custom script developed in the MATLAB software was used to construct the initial adsorption geometries [124]. The script systematically positioned adsorbate molecules at the different adsorption sites (fcc, hcp, bridge, and top) on the slab, while controlling their orientation and distance relative to the surface. This approach enabled consistent and reproducible generation of initial configurations prior to DFT optimisation, with improved precision compared to manual placement.

For example, Figure 8B depicts CO_2 adsorbed at each of these sites. Furthermore, all four sites were evaluated for all pathway adsorbates such as CO_2, COOH, CO + H_2O, and H. It is worth noting that these four configurations exhibit differences in total energy; however, this difference is relatively small in a simple system, such as pure silver. As the system becomes more complex, for example, Ag_5/Ag (111), Ag_3/Ag (111), Au_5/Ag (111), and Au_3/Ag (111) the total energy at these four configurations increases. Based on these results, the configuration with the lowest total energy was identified and subsequently used to construct the CO reaction pathway diagram.

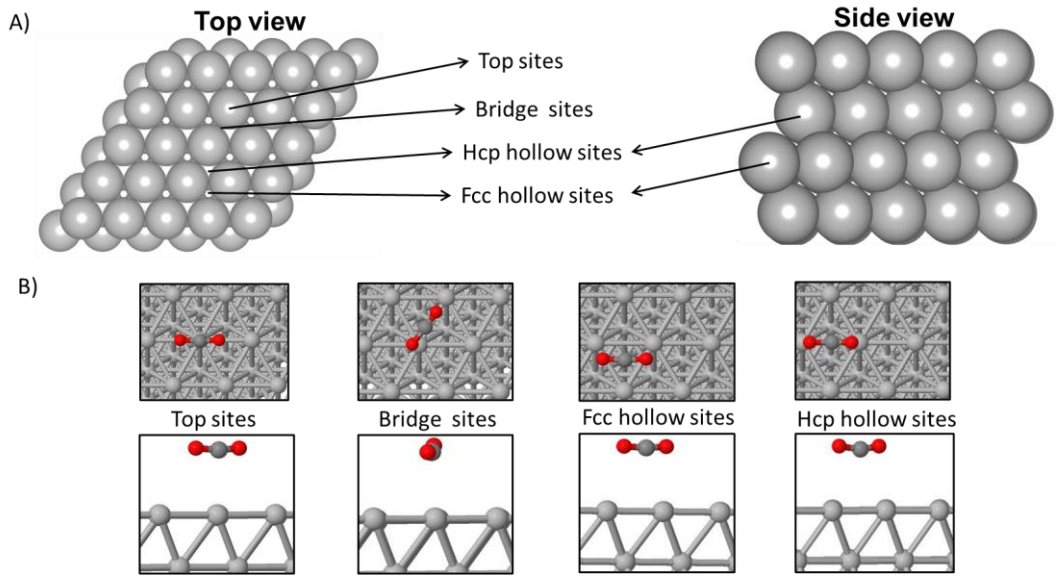

Fig. 8 Four-layer Ag (111) models and CO_2 adsorbed on Ag (111). A) The four high-symmetry adsorption sites (top site, Fcc- hollow site, Hcp hollow site and bridge site) were denoted by arrows. B) Top and side views for the top site, the bridge site, the Fcc hollow site and the Hcp hollow site, respectively. The Ag, O and C atoms are represented with grey, red and dark grey spheres respectively.

As illustrated, the conversion of CO_2 to CO proceeds spontaneously from a thermodynamic standpoint in the gas phase. To explore this process, three reaction pathways were evaluated based on our DFT calculations. The first, known as the adsorbed hydrogen transfer mechanism, involves surface-bound hydrogen reacting with $*CO_2$ to produce *COOH, with a calculated reaction barrier of approximately 1.18 eV on Ag (111). This is followed by desorption of the second *COOH species. However, our computational results indicate that *COOH more readily converts to *CO via a water-assisted hydrogen transfer mechanism, which exhibits a lower energy barrier of around 1.03 eV. These findings suggest that the water-assisted pathway is energetically more favourable for the reduction of CO_2 to CO, as depicted in Figure 9A. In the solvated phase, the energy barrier is further reduced, as shown in Figure 9B. Here, the intermediate *COOH exhibits a slightly lower barrier of 1.11 eV. In the third pathway (CO + H_2O), the barrier decreases by 0.16 eV (to 0.87 eV), while for ($*CO + H_2O$) it falls by 0.21 eV (to 0.51 eV). Meanwhile, the hydrogen evolution reaction (HER) shows a slight increase in barrier, by approximately 0.02 eV.

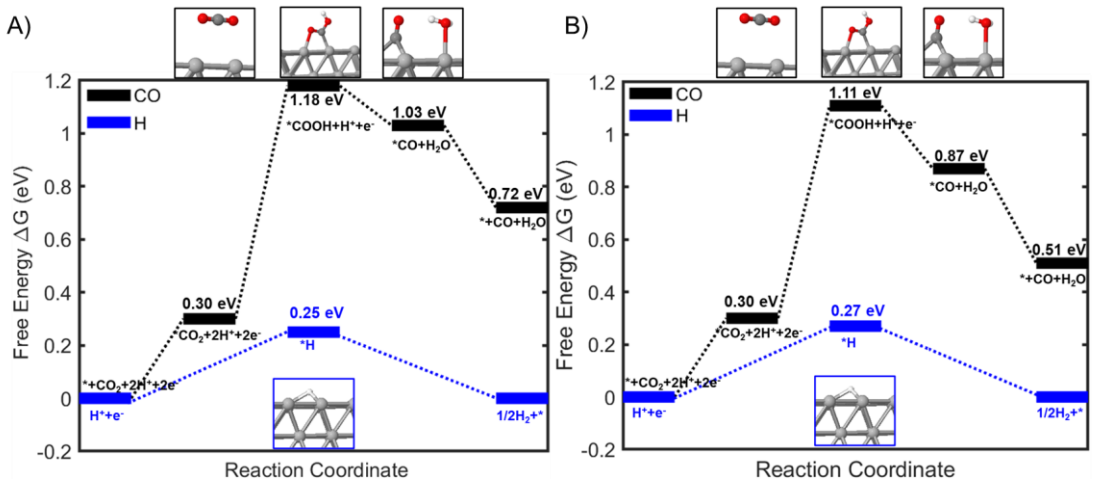

Fig. 9 Gibbs free energy diagrams for the CO_2RR to CO on Ag (111). A) Pathway in the gas phase. B) Pathway in the solvation phase. * Represents the metal surface and adsorption site of surface species.

These results are consistent with previous theoretical studies of CO_2 reduction on silver surfaces [106-112], which also report that proton-coupled electron transfer steps involving *COOH intermediates are key to determining activity, and that water-assisted mechanisms can lower reaction barriers. While the absolute values of the energy barriers may differ from earlier reports due to variations in computational setup such as slab size, solvation model, and exchange–correlation functional the overall trend remains in good agreement.

4.3.2 Silver cluster on Ag (111).

As an initial step towards understanding the role of atomic quantum clusters (AQCs), both three-dimensional (3D) bipyramidal and two-dimensional (2D) trapezoidal geometries were considered. The optimised 3D bipyramidal structures of Ag_5 and Au_5 are shown in Figure 10, with the corresponding interatomic distances listed in Table 1; these geometries are in good agreement with previously reported theoretical and computational studies [125]. The optimised 2D trapezoidal structures of Ag_5 and Au_5 AQCs are presented in Figure 11, and the associated atomic distances are summarised in Table 2, also showing good agreement with the same reference [125].

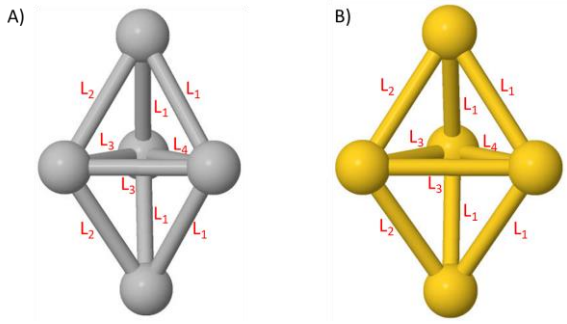

Fig. 10 The optimised structures of bipyramidal AQC. A The geometry of silver AQC, and B the geometry of gold AQC.

Table 1 The bond length.

Bond length (Å)	Ag_5	Au_5
L_1	2.80	2.77
L_2	2.76	2.73
L_3	2.67	2.70
L_4	2.99	2.99

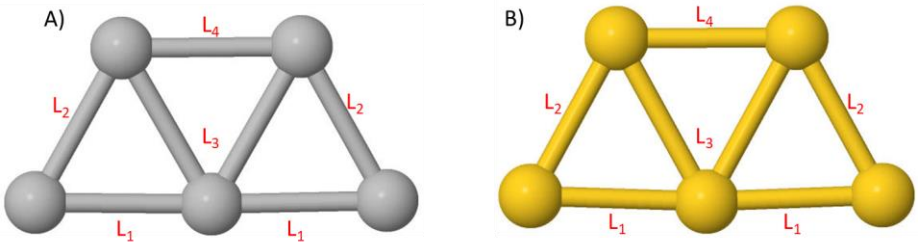

Fig. 11 The optimised structures of trapezoidal AQC. A The geometry of silver AQC, and B the geometry of gold AQC.

Table 2 The bond length.

Bond length (Å)	Ag_5	Au_5
L_1	2.68	2.61
L_2	2.70	2.66
L_3	2.76	2.76
L_4	2.74	2.67

For larger clusters, where the number of possible geometries increases rapidly, the identification of the most stable structure becomes increasingly challenging. Global optimisation (GO) techniques are therefore employed to explore the potential energy surface. In such approaches, a nearby minimum in the potential energy can be identified, although this process is computationally demanding. Consequently, many GO algorithms are implemented in two variants: one that evaluates the cluster energy at a given geometry, and another that further relaxes this geometry using gradient-driven methods to reach a local minimum [126]. These strategies are often combined with DFT calculations for accurate refinement of low-energy configurations. In contrast, for smaller clusters such as Ag_3 and Au_3, the reduced configurational complexity allows for a more straightforward determination of stable geometries. For the smaller Ag_3 and Au_3 clusters, which contain fewer atoms, only a single stable geometric configuration was identified. These structures are shown in Figure 12, with the corresponding interatomic distances reported in Table 3; these results are in good agreement with previously reported theoretical and computational studies [127,128].

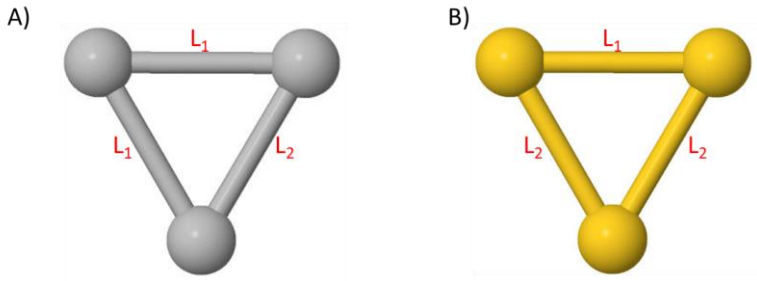

Fig. 12 The optimised structures of dimer AQC. (A) The geometry of silver AQC, and (B) the geometry of gold AQC.

Table 3 The bond length.

Bond length (Å)	Ag_3	Au_3
L_1	2.84	2.84
L_2	2.83	2.83

A comparison of the total energies reveals that, for the five-atom clusters, the trapezoidal two-dimensional (2D) configuration is the most stable structure; this finding is in good agreement with previously reported theoretical and computational studies [125]. This configuration exhibits a lower total energy and more favourable geometric characteristics than the corresponding three-dimensional (3D) bipyramidal forms, as illustrated in Figure 13.

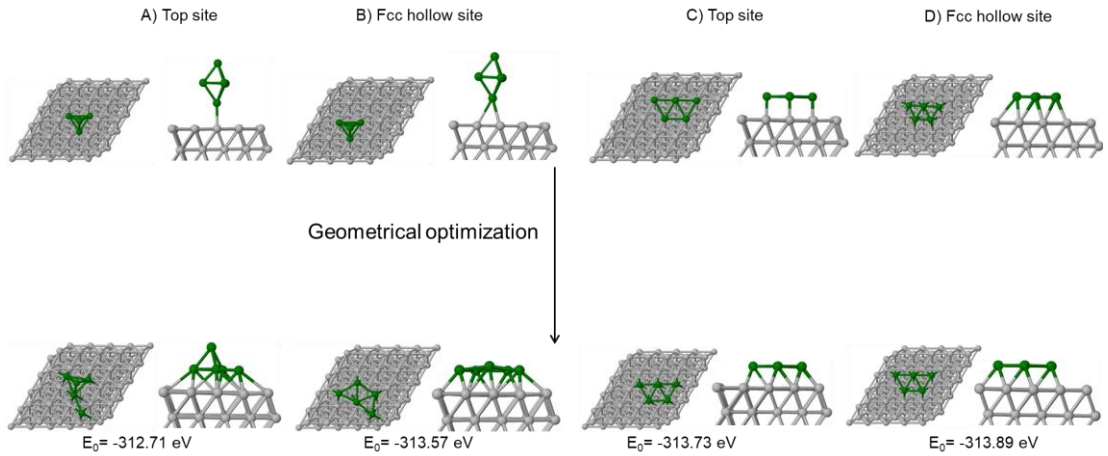

Fig. 13 Comparison between bipyramidal and trapezoidal. A) and B) the geometric bipyramidal cluster. C) and D) the geometric of trapezoidal cluster.

The presence of the AQC on the surface introduces greater structural complexity compared with pure silver. In addition to the fundamental adsorption sites, new sites arise both on the cluster itself and at the interface regions. The geometric structure of Ag_5/Ag (111) is shown from both top and side perspectives in Figure 14A, while that of Ag_3/Ag (111) is depicted similarly in Figure 14B. The key step in the conversion of CO_2 to CO involves the intermediate *COOH species. On pure silver, the total energy difference between adsorption sites at the *COOH stage is minimal, approximately 0.02 eV. However, with AQCs present on the surface the difference increases markedly to approximately 0.50 eV. Summaries of the adsorption sites for Ag_5 and Ag_3 on the surface are presented in Figure 14C and 14D, respectively.

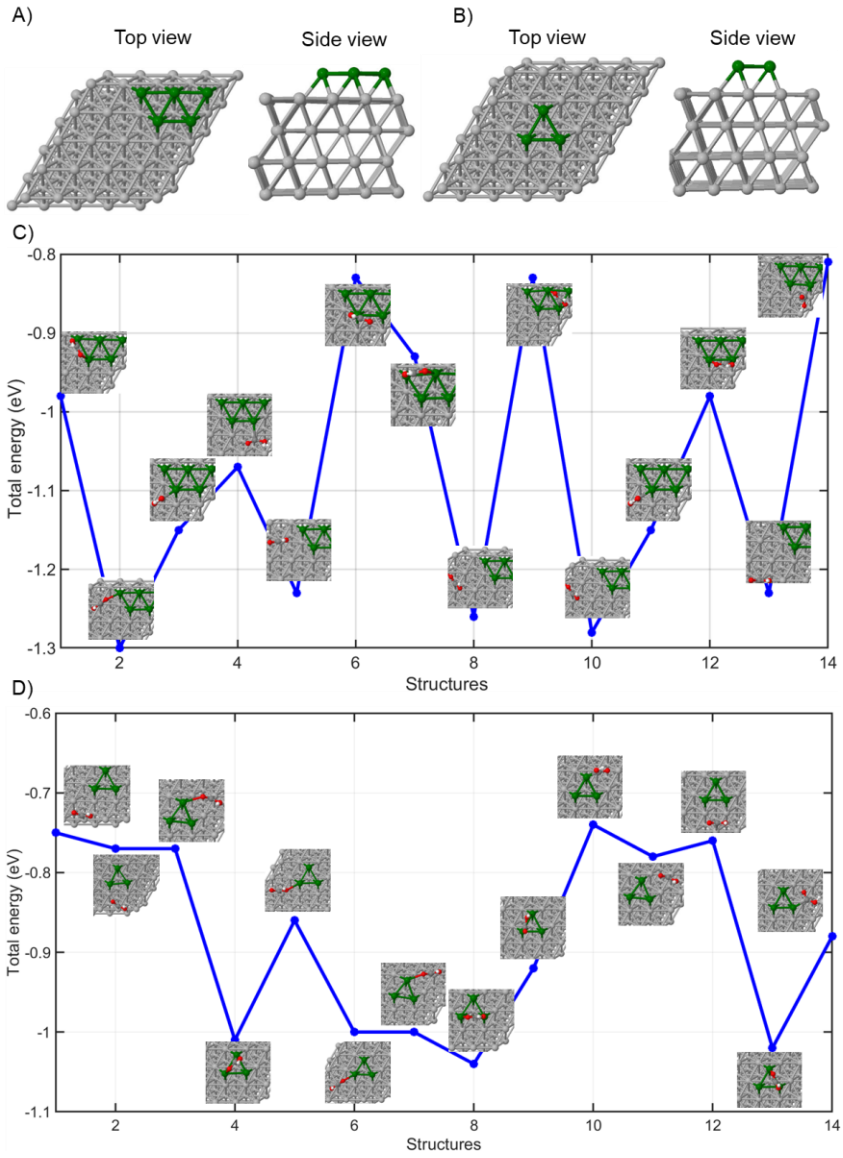

Fig. 14 The DFT calculations. A) The optimised structures in trapezoidal (Ag_5/Ag (111)). B) The optimised structures in trapezoidal (Ag_3/Ag (111)). C) Total energy difference for several positions of COOH on Ag_5/Ag (111). D) Total energy difference for several positions of COOH on Ag_3/Ag (111). The Ag (111), AQC, O, C and H atoms are represented with grey, green, red, dark grey and white spheres, respectively.

Although the adsorbate molecules tend to bind to the surface in the case of Ag_5, their behaviour differs for Ag_3, where adsorption preferentially occurs directly on the cluster rather than on the underlying silver surface. This observation indicates distinct adsorption dynamics for Ag_5 and Ag_3, likely arising from differences in their electronic structures, surface energies, and geometric configurations. Moreover, the reaction energy barriers associated with AQCs

supported on the surface are slightly lower than those observed for pristine silver under both gas-phase and solvated conditions.

The energy barriers for Ag_5 and Ag_3 in the gas phase are illustrated in Figure 15A. Notably, under solvated conditions, the energy barriers are significantly reduced relative to pristine silver, highlighting the stabilising effect of the solvent environment. A comparative analysis of the solvated energy barriers for Ag_5 and Ag_3 is presented in Figure 15B, which clearly demonstrates that Ag_3 exhibits a markedly lower barrier than both pristine silver and Ag_5. According to the Eyring equation (3-4), this ~0.02 eV reduction in activation free energy corresponds to an approximate twofold increase in reaction rate at room temperature. This behaviour suggests modestly enhanced stabilisation of reaction intermediates and improved reactivity for Ag_3 in the solvated phase, with implications for its catalytic and electronic performance.

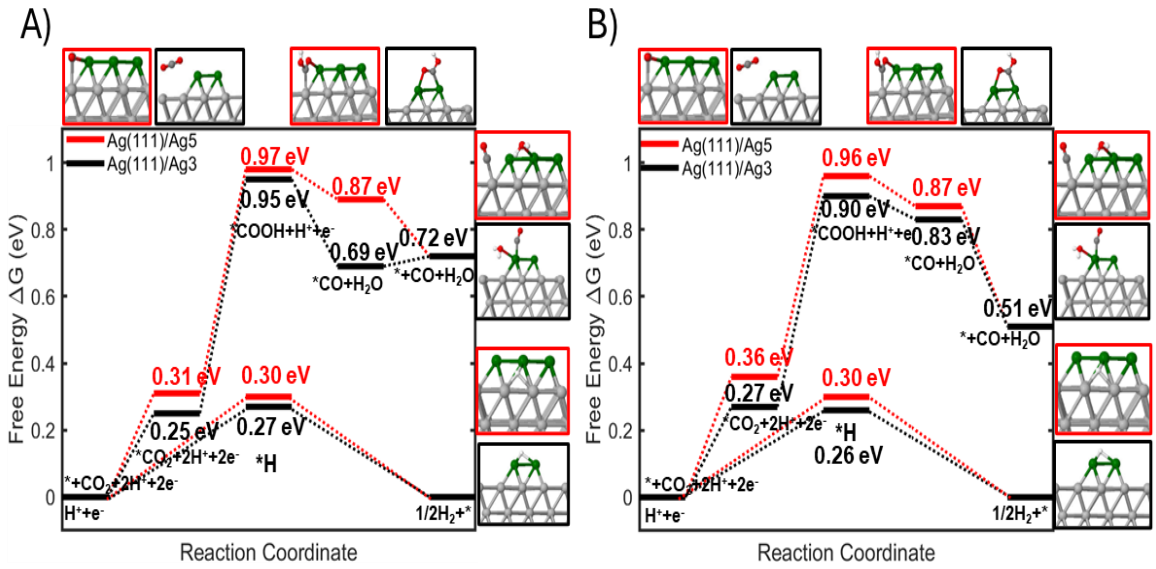

Fig. 15 Comparison between Ag_5/Ag (111) and Ag_3/Ag (111). A) CO pathway is the *CO_2, *COOH, *CO+H_2O and *+CO+H_2O in the gas phase, respectively. B) CO pathway is the *CO_2, *COOH, *CO+H_2O and *+CO+H_2O in the solvation phase, respectively. The red colour of line and frame are referred to Ag_5/Ag (111), and the black colour of line and frame are referred to Ag_3/Ag (111). The Ag (111), AQC, O, C and H atoms are represented with grey, green, red, dark grey and white spheres, respectively.

The presence of atomic quantum clusters (AQCs) increases the complexity of surface interactions, thereby enhancing catalytic activity and modifying reaction behaviour under both gas-phase and solvated conditions. These findings highlight the important role of AQCs in governing the reactivity and stability of the surface across different environments. Further insight into the electronic structure of these systems is provided by Bader charge analysis. The results show that the *COOH intermediate on Ag_5 gains approximately 0.43 electrons through charge transfer from both the Ag_5 cluster and the substrate, whereas on Ag_3 it gains around 0.45 electrons exclusively from the Ag_3 cluster. Although the difference in the total transferred charge is small, the distinct charge-transfer pathway is mechanistically important. Electron donation to *COOH stabilises this key reduction intermediate, promotes activation of the adsorbed CO_2-derived species, and can facilitate subsequent proton-coupled electron-transfer steps. The slightly higher and more localised charge transfer on Ag_3 therefore suggests somewhat stronger electronic activation of *COOH, which is consistent with enhanced reduction reactivity.

4.3.3 Gold cluster on Ag (111).

The catalytic performance of gold clusters was investigated using the same systematic approach applied to the silver clusters, with Au_5 and Au_3 considered as representative systems. Gold exhibits selectivity comparable to that of silver, with both metals facilitating the electrochemical conversion of CO_2 to CO. Consequently, understanding the geometric and electronic properties of gold clusters supported on the Ag (111) surface is essential for a meaningful comparison of their catalytic behaviours.

The results indicate that the two-dimensional trapezoidal configuration is the most stable structure, owing to its lower total energy and favourable geometric characteristics, as illustrated in Figure 16. To further examine charge transfer effects, Bader charge analysis and charge

density difference calculations were performed for the clean metal surface, defined here as the bare surface without any adsorbed molecular species. The calculated charge distribution provides insight into the electrochemical behaviour of the surface. Regions of charge accumulation and depletion determine the electron-donating and electron-accepting character of active sites, which directly influences the adsorption and activation of reaction intermediates. In particular, electron-rich sites can facilitate the activation of CO_2-derived species and stabilise key intermediates such as *COOH, thereby promoting proton-coupled electron transfer steps. Consequently, the observed charge redistribution is expected to play a crucial role in lowering reaction barriers and enhancing catalytic activity. The corresponding results are presented in Table 4 and Figure 17.

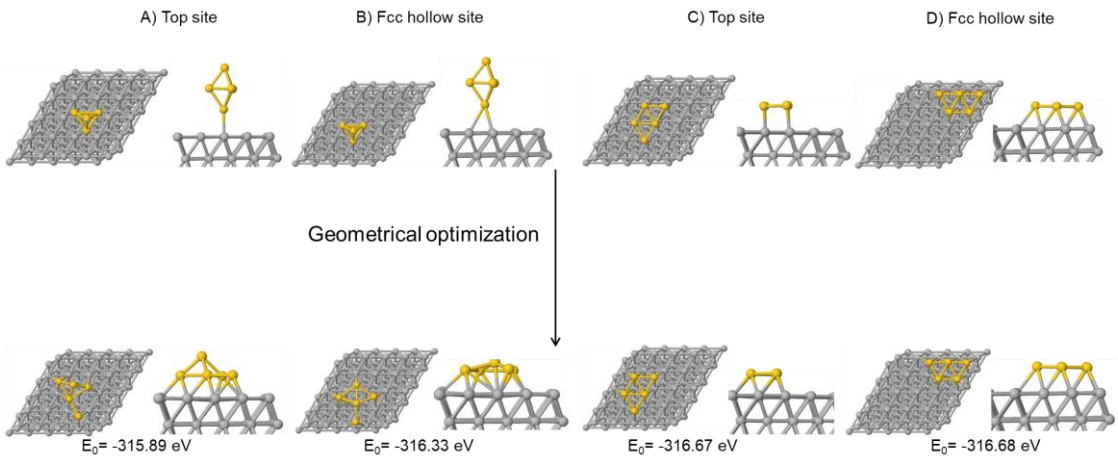

Fig. 16 Comparison between bipyramidal and trapezoidal. A and B the geometric bipyramidal cluster. C and D the geometric of trapezoidal cluster.

Table 4 Bader charge analysis of the substrate and cluster.

	Slab	**AQC**
$Ag(111)/Ag_5$	Gain 0.02e	Loss 0.02e
$Ag(111)/Ag_3$	Gain 0.03e	Loss 0.03e
$Ag(111)/Au_5$	Loss 0.85e	Gain 0.85e
$Ag(111)/Au_3$	Loss 0.61e	Gain 0.61e

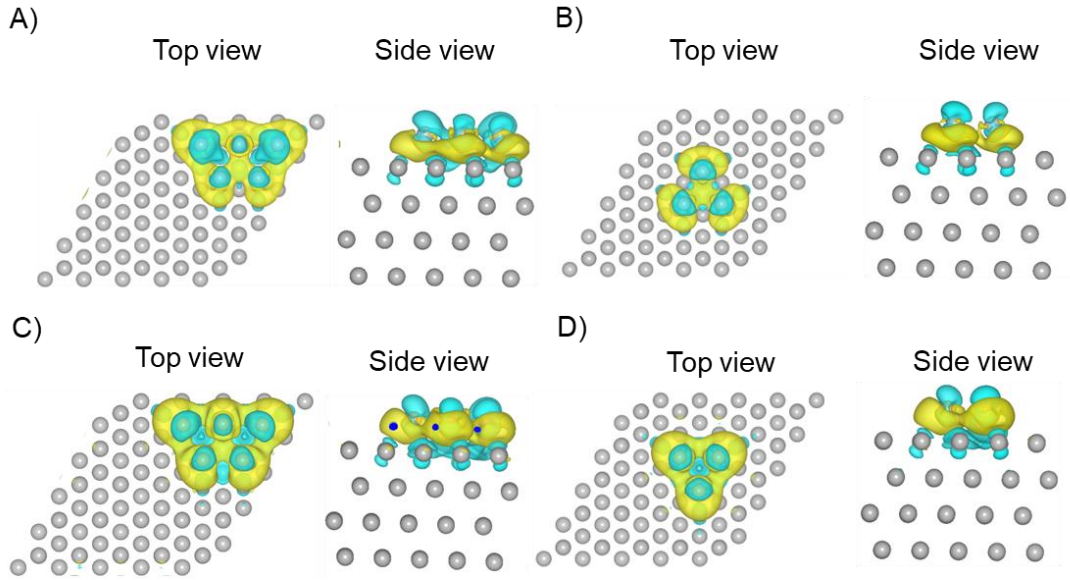

Fig. 17 The charge density difference. A) The charged density difference of Ag_5/Ag (111). B) The charged density difference of Ag_3/Ag (111). C) The charged density difference of Au_5/Ag (111). D) The charged density difference of Au_3/Ag (111). The yellow and cyan regions depict the electron accumulation and depletion, respectively.

Having identified the most stable structure of Au_5, the next step is to examine the electrochemical reduction of carbon dioxide using the gold clusters. The geometric structures of Au_5/Ag (111) and Au_3/Ag (111) are shown in both top and side views in Figures 18A and 18B, respectively. The total energy differences between adsorption sites in gold clusters are found to be similar to those observed for silver clusters, suggesting a comparable degree of site stability. A detailed summary of the adsorption sites for Au_5/Ag (111) and Au_3/Ag (111) is provided in Figures 18C and 18D, respectively.

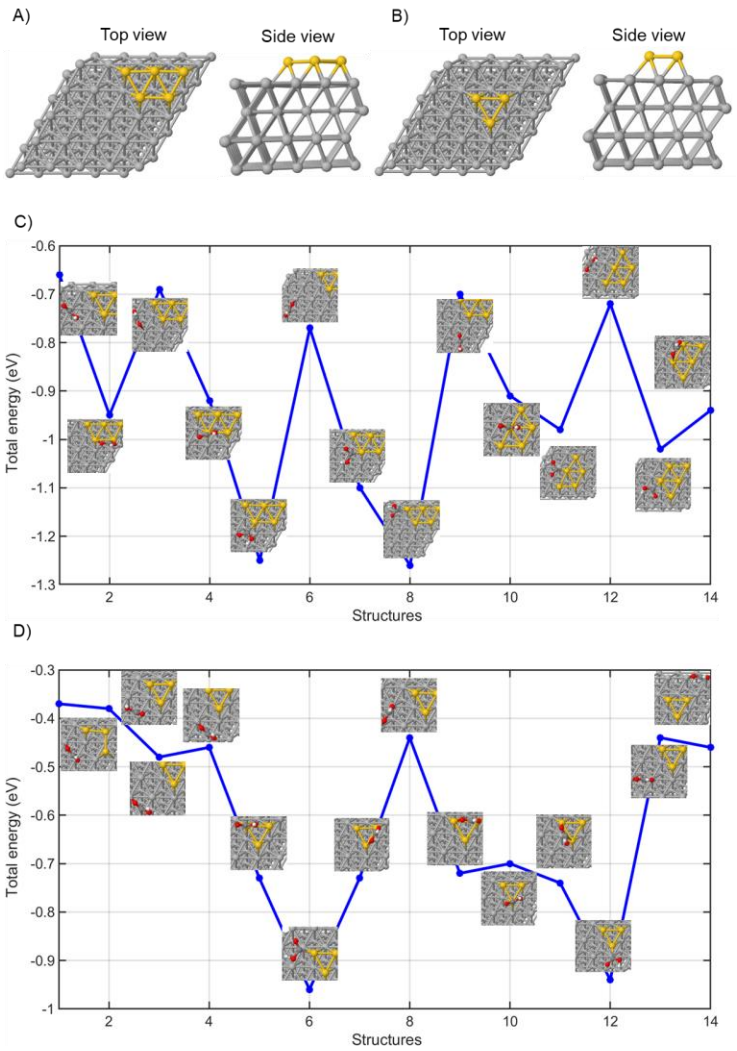

Fig. 18 The DFT calculations. A) The optimised structures in trapezoidal (Au_5/Ag (111)). B) The optimised structures in trapezoidal (Au_3/Ag (111)). C) Total energy difference for several positions of COOH on Au_5/Ag (111). D) Total energy different for several positions of COOH on Au_3/Ag (111). The Ag (111), AQC, O, C and H atoms are represented with grey, yellow, red, dark grey and white spheres, respectively.

The binding behaviour of molecules differs markedly between silver and gold clusters, reflecting distinct adsorption characteristics. Whereas molecules exhibit varied binding tendencies on silver clusters, they show a pronounced preference for cluster–substrate interface sites on gold clusters. This distinction suggests that adsorption behaviour is governed by fundamental differences in the electronic structure, surface energy, and geometric configuration of silver and gold clusters. Such variations are expected to influence the stability and reactivity of the clusters, thereby shaping their catalytic performance.

Moreover, the reaction energy barriers associated with gold clusters supported on the surface are significantly lower than those observed for silver clusters under both gas-phase and solvated conditions. This reduction in energy barriers indicates that gold clusters facilitate more favourable reaction pathways than their silver counterparts. The gas-phase energy barriers for Au_5 and Au_3 are shown in Figure 19A, while Figure 19B presents a comparative analysis of the corresponding barriers under solvated conditions. Notably, Au_5 exhibits a substantially lower energy barrier than both the silver clusters and Au_3, suggesting enhanced stabilisation of reaction intermediates and improved reactivity in the solvated phase. These differences between gold and silver clusters underscore the importance of atomic composition and structural configuration in determining adsorption behaviour and reaction energetics.

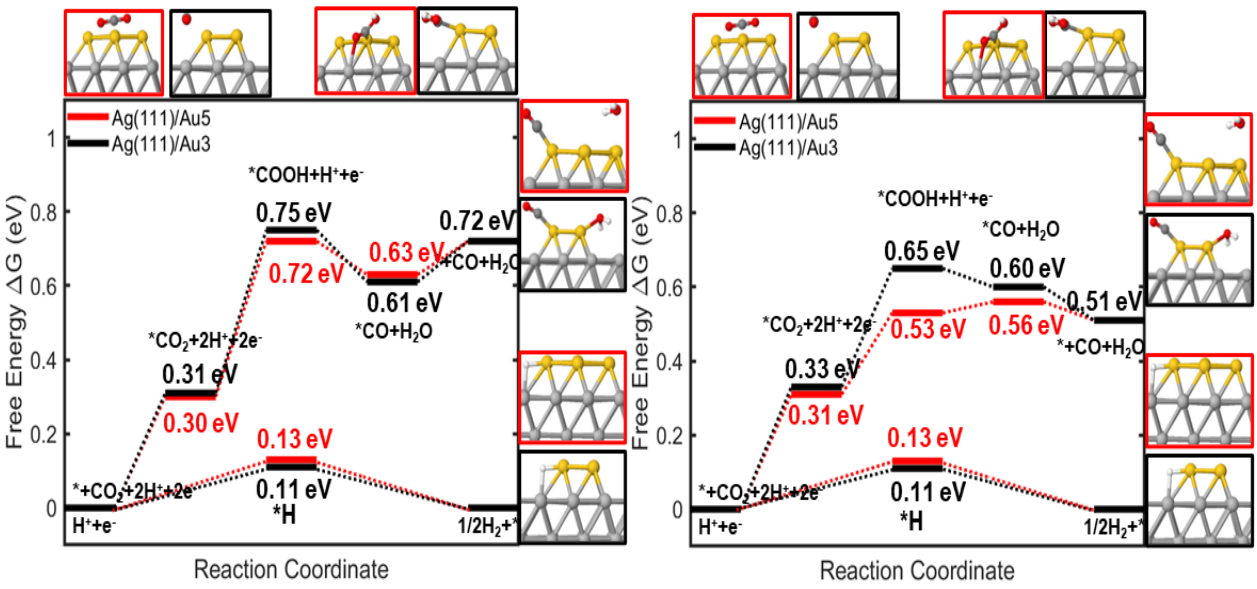

Fig. 19 Comparison between Au_5/Ag (111) and Au_3/Ag (111). A) CO pathway is the $*CO_2$, *COOH, $*CO+H_2O$ and $*+CO+H_2O$ in the gas phase, respectively. B) CO pathway is the $*CO_2$, *COOH, $*CO+H_2O$ and $*+CO+H_2O$ in the solvation phase, respectively. The red colour of line and frame are referred to Au_5/Ag (111) and the black colour of line and frame are referred to Au_3/Ag (111). The Ag (111), AQC, O, C and H atoms are represented with grey, yellow, red, dark grey and white spheres, respectively.

To facilitate a clear comparison of the results obtained from the three distinct stages of the analysis, all findings are consolidated into a single set of comparative plots. Figures 20 and 21 present a comparison of the energy barriers associated with the CO pathway and the hydrogen evolution reaction (HER), respectively, under both gas-phase and solvated conditions. Notably, for silver clusters, smaller clusters exhibit lower energy barriers than larger clusters. In contrast, gold clusters display the opposite trend, with larger clusters showing lower energy barriers than their smaller counterparts.

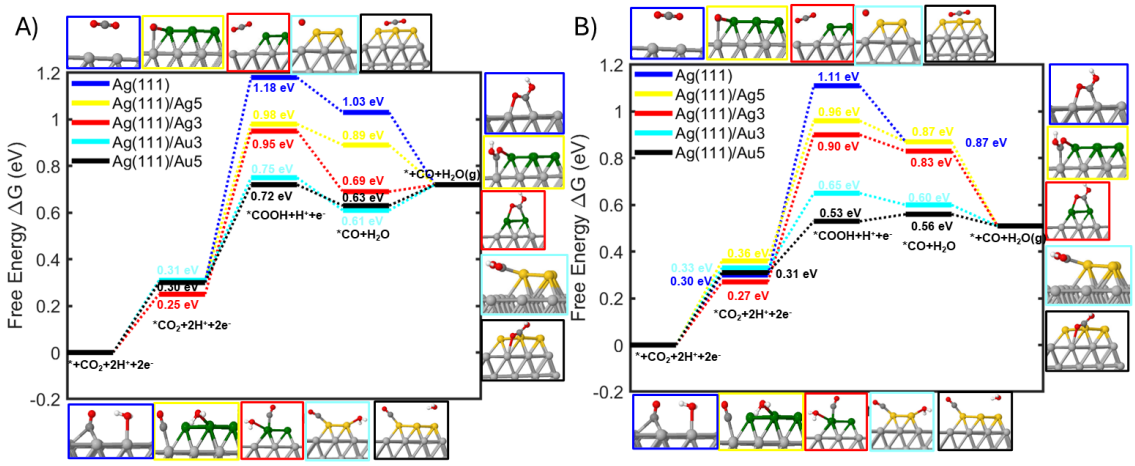

Fig. 20 Comparison between all the structure for the CO pathway. A) The energy barriers in the gas phase. B) The energy barriers in the solvation phase. The blue colour of line and frame are referred to Ag (111), the yellow colour of line and frame are referred to Ag_5/Ag (111), the red colour of line and frame are referred to Ag_3/Ag (111), the cyan colour of line and frame are referred to Au_3/Ag (111) and the black colour of line and frame are referred to Au_5/Ag (111).

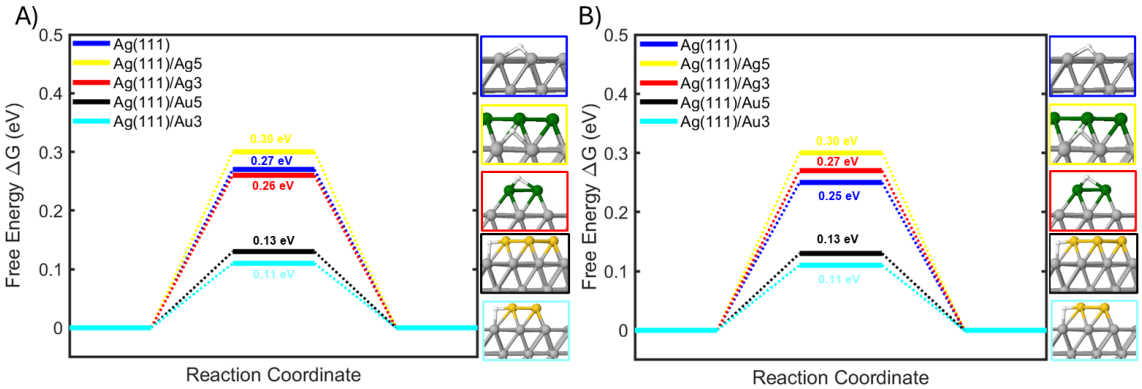

Fig. 21 Comparison between all the structure for the HER. A) The energy barriers in the gas phase. B) The energy barriers in the solvation phase. The blue colour of line and frame are referred to Ag (111), the yellow colour of line and frame are referred to Ag (111)/Ag_5, the red colour of line and frame are referred to Ag (111)/Ag_3, the black colour of line and frame are referred to Ag (111)/Au_5, the cyan colour of line and frame are referred to Ag (111)/Au_3.

To rationalise this behaviour, Bader charge analysis was employed to examine charge transfer effects. The results indicate that gold clusters gain more electrons than silver clusters, reflecting differences in charge distribution that may significantly influence their stability and reactivity. Specifically, for the *COOH intermediate on Au_5/Ag (111), the COOH molecule gains approximately 0.34 electrons, the substrate loses about 1.04 electrons, and the Au_5 cluster gains approximately 0.70 electrons. In comparison, for Au_3/Ag (111), the COOH molecule gains around 0.29 electrons, the substrate loses approximately 0.70 electrons, and the Au_3 cluster gains about 0.41 electrons. Table 5 and 6 presents the results of Bader charge analysis performed for COOH and H, respectively, on Ag_5/Ag (111), Ag_3/Ag (111), Au_3/Ag (111) and Au_5/Ag (111) to explore the nature of charge transfer.

Table 5 Bader charge in COOH situation.

	Slab	COOH	AQC
Ag (111)	Loses 0.38e	Gains 0.38e	
Ag_5/Ag (111)	Loses 0.22e	Gains 0.43e	Loses 0.21e
Ag_3 /Ag (111)	Loses 0.01e	Gains 0.45e	Loses 0.44e
Au_3/Ag (111)	Loses 0.70e	Gains 0.29e	Gains 0.41e
Au_5/Ag (111)	Loses 1.04e	Gains 0.34e	Gains 0.70e

Table 6 Bader charge in HER situation.

	Slab	H	AQC
Ag (111)	Loses 0.21e	Gains 0.21e	
Ag_5/Ag (111)	Loses 0.11e	Gains 0.18e	Loses 0.08e
Ag_3 /Ag (111)	Loses 0.19e	Gains 0.22e	Loses 0.03e
Au_3/Ag (111)	Loses 0.61e	Gains 0.12e	Gains 0.49e
Au_5/Ag (111)	Loses 0.90e	Gains 0.13e	Gains 0.77e

Finally, Table 7 presents the values of the DFT total energies (E_{DFT}), zero-point energies (E_{ZPE}), entropies (TS) multiplied by temperature (T = 298.15 K), free energies (G) and adsorption energy (Eabs).

Table 7 DFT total energies (E_{DFT}), zero-point energies (E_{ZPE}), entropies (T S, at T = 300 K), free energies (G) and adsorption energy (E_{abs}).

Catalysts	E_{DFT}	E_{ZPE}	$T * S$	G	E_{ads}
			Ag(111)		
*CO_2	-322.50	0.33	0.11	-322.38	0.18
*COOH	-325.48	0.63	0.18	325.03	-1.59
*H	-302.41	0.15	0.01	-302.41	0.27
			Ag(111)/Ag_5		
*CO_2	-337.03	0.34	0.17	-336.86	0.19
*COOH	-340.12	0.61	0.21	-339.72	-1.69
*H	-317.00	0.11	0.03	-316.92	0.22
			Ag(111)/Ag_3		
*CO_2	-331.02	0.34	0.15	-330.86	0.11
*COOH	-334.17	0.64	0.16	-333.69	-1.83
*H	-311.01	0.14	0.01	-310.87	0.12
			Ag(111)/Au_3		
*CO_2	-332.65	0.35	0.17	-332.47	0.15
*COOH	-336.11	0.63	0.13	-335.61	-2.10
*H	-312.82	0.16	0.03	-312.69	-0.02
			Ag(111)/Au_5		
*CO_2	-339.93	0.34	0.16	-339.75	0.13
*COOH	-343.39	0.62	0.22	-342.99	-2.12
*H	-320.06	0.16	0.03	-319.93	0.00

4.4 Conclusion

This chapter investigated the electrochemical reduction of CO_2 on silver surfaces and the influence of atomic quantum clusters on reaction energetics. Silver and gold clusters of different sizes were examined to assess their impact on catalytic performance, highlighting the importance of both cluster composition and size.

While CO_2 reduction on extended silver surfaces and on isolated clusters has been widely investigated, the combined system of supported atomic quantum clusters on metallic substrates has not been systematically explored. The present results therefore extend existing understanding by demonstrating that the introduction of clusters—either of the same element or a different metal—can be used to tune reaction energetics. In particular, silver clusters moderately reduce the CO_2 reduction energy barrier, with smaller clusters exhibiting higher activity, whereas gold clusters lead to a more substantial barrier reduction, particularly for larger cluster sizes. These contrasting trends are attributed to differences in charge transfer and electronic interactions between the clusters and the silver substrate.

The hydrogen evolution reaction (HER) was also analysed to evaluate catalyst selectivity. Under solvated conditions, silver clusters increase the HER energy barrier, while gold clusters lower it, indicating enhanced hydrogen formation on gold-modified surfaces. This dual behaviour is directly relevant to syngas production, as syngas (a mixture of CO and H_2) is a key industrial fuel and chemical feedstock.

Future work extending this approach to gold substrates would provide further insight into cluster–substrate interactions and support the rational design of efficient electrocatalysts for CO_2 conversion.

5.Electrochemical reduction of CO_2 on tin substrate

This chapter investigates the effect of bismuth (Bi) modification on the electrocatalytic reduction of carbon dioxide over the Sn (200) surface using density functional theory calculations. Electrochemical CO_2 reduction over tin (Sn) surfaces has attracted significant attention due to the low cost and abundance of Sn compared to noble metals such as silver, which was investigated in Chapter 4, as well as the distinct product selectivity, where Sn Favors formic acid formation while silver predominantly produces carbon monoxide.

The study follows a systematic approach, beginning with the pristine Sn surface, followed by substitution of surface and subsurface Sn atoms with Bi, and finally the adsorption of Bi atoms on the Sn surface. The results show that pristine Sn preferentially promotes formic acid formation via the *OCHO intermediate, whereas the CO pathway and hydrogen evolution reaction (HER) involve higher energy barriers. Bi incorporation significantly improves catalytic selectivity by increasing the energy barriers for *COOH formation and hydrogen adsorption under both gas-phase and solvated conditions, while further stabilising the *OCHO intermediate. These findings demonstrate that Bi modification effectively tunes the reaction energetics of Sn-based catalysts, providing a promising strategy for efficient and selective CO_2 reduction.

5.1 Introduction

Currently, the primary strategies for CO_2 utilisation include biological reduction, thermocatalytic reduction, photocatalytic reduction, and electrochemical reduction. Among these approaches, electrochemical CO_2 reduction (CO_2RR) has attracted particular attention due to its ability to convert CO_2 into useful products under relatively mild conditions by applying an external potential [129-134]. Unlike thermochemical or photochemical methods, CO_2RR does not require high temperatures, elevated pressures, or light irradiation, making the process both controllable and energy efficient [135]. Furthermore, when powered by renewable electricity sources such as wind or solar energy, electrochemical CO_2 reduction can proceed without additional CO_2 emissions, positioning it as one of the most promising routes toward economically viable and environmentally sustainable carbon utilisation technologies [136].

Among the various electrocatalysts explored for CO_2RR, tin (Sn) has emerged as a promising candidate due to its low cost and natural abundance [137,138]. Tin exhibits a strong binding affinity for the *OCHO intermediate, which facilitates the initial hydrogenation step in the CO_2-to-formate pathway [137-139]. However, the subsequent electron transfer required to convert *OCHO into formic acid (HCOOH) is energetically demanding, resulting in high overpotentials and reduced energy efficiency. In addition, Sn binds *COOH and *H intermediates with moderate strength, making it challenging to fully suppress competing CO formation and hydrogen evolution reactions. Consequently, the faradaic efficiency for formate production on pure Sn catalysts is typically limited to approximately 80–85% [140].

In recent years, alloying has emerged as an effective strategy for improving electrocatalytic performance by enabling precise tuning of the electronic structure at surface active sites, thereby modulating the binding energies of key reaction intermediates [141,142]. In the context

of CO_2RR, bimetallic catalysts can enhance selectivity toward formate by stabilising the *OCHO intermediate while suppressing undesired side reactions [143]. Among the various bimetallic systems investigated, Sn-based alloys such as Bi/Sn [30] and Cu/Sn [144] have demonstrated considerable promise. For example, Cu/Sn alloys, guided by theoretical insights, have achieved high formate selectivity by effectively suppressing both hydrogen evolution and CO production [145]. The Sn-Bi binary system can be categorised into three distinct configurations: substitutional systems, in which Bi atoms replace Sn atoms at surface or subsurface sites; surface adatom systems, where Bi atoms are adsorbed on the Sn surface; and alloyed systems containing approximately equal proportions of Sn and Bi.

5.2 Computational framework.

Density functional theory calculations were conducted using Vienna Ab initio Simulation Package (VASP) software [81] to obtain the electronic properties, as well as the geometrical properties in the substituted and adatoms of bismuth. Accordingly, the Sn (200) surface was constructed, as it has been reported to be one of the most thermodynamically stable facets [30]. The geometric structure of the Sn (200) surface is depicted in Figure 22, shown from both the top and side perspectives. The bulk lattice parameter of Sn was first optimised, yielding a value of 5.88 Å, which is in good agreement with the experimental value of 5.82 Å [146]. For calculational accuracy, in sampling the Brillouin zones, a 12 × 12 × 12 k-points mesh was employed. In this study, the slab installation was executed using the methodology established by Ong et al. [120] alongside VESTA software [121], which offers a comprehensive framework for applying these techniques in relevant geometrical contexts. However, all images were generated using Jmol software [122].

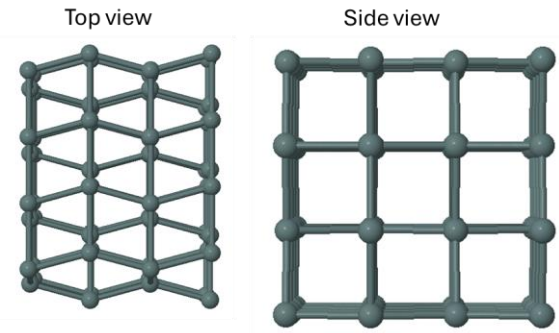

Fig 22. The optimised structures of the Sn (200).

Sn (200) as (4 × 4)-four layers unit cell with tin atom is modelled by 11.76 Å ×12.79 Å, to prevent interactions between the supercell and its periodic images in the z-direction, a vacuum of 20 Å is maintained in that direction. Convergence tests were performed with respect to both the in-plane supercell size and the vacuum thickness in the out-of-plane direction. The results confirmed that the chosen supercell dimensions and vacuum spacing were sufficient to eliminate spurious interactions between periodic images, including both electrostatic and elastic interactions. Consequently, the calculated energies and structural properties are considered to be well converged.

Furthermore, the top three layers of atoms were relaxed, and the remaining layer were fixed in the bulk phase, during the structural optimisation. For the relaxation of all selected initial structures, a kinetic energy cut-off of 500 eV was employed. The Brillouin zone was sampled using a 2 × 2 × 1 Monkhorst–Pack k-point mesh, which was selected based on k-point convergence tests (see Figure 23), where the total energy of the system was evaluated as a function of k-point density. The results showed that beyond this grid, the total energy variations became negligible, indicating sufficient convergence. A Generalized Gradient Approximation (GGA) was used to calculate the total energy and the geometric relaxations. The Perdew-Burke-Ernzerhof (PBE) [69], exchange-correlation functional was used to compute the correlation and exchange energy. London dispersion forces were described by Becke-Johnson damping function method [83] and the spin-polarized density functional theory approach. A

convergence threshold value was fixed to 10^{-4} eV for the self-consistent minimisation. A threshold force was set at 0.02 eV/A allowing the relaxation of all structures. The Bader charge analysis was performed using a code developed by the Henkelman group [98-100].

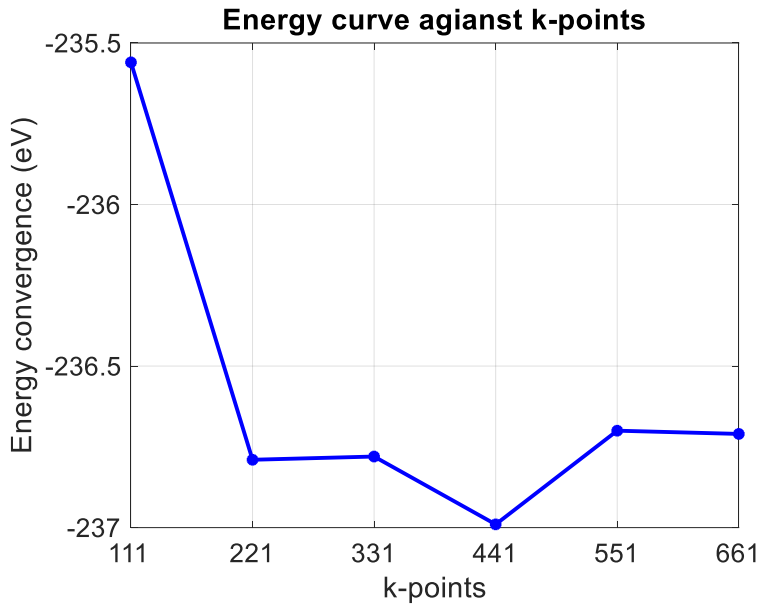

Fig. 23 The energy convergence vs k-points.

The state of density and the thermodynamics at the standard range for room calculations used the open-source command-line program VASPKIT [85]. The Gibbs free energy at 298.15 K and 1 ATM were calculated with equation (4-1).

Moreover, to evaluate the thermodynamic stability of the molecules the adsorption energy is obtained using equation (3-16).

Formate pathway reaction mechanism, mechanism underlying the transformation of CO_2 into HCOOH is suggested to involve three fundamental steps, which are represented below.

$$CO_{2(aq)} + * + H_{(aq)}^{+} + e^{-} \leftrightarrow *OCHO \quad (5\text{-}1)$$

$$*OCHO + H^{+} + e^{-} \leftrightarrow *HCOOH \quad (5\text{-}2)$$

$$*HCOOH \leftrightarrow HCOOH_{(aq)} \quad (5\text{-}3)$$

where a lone asterisk (*) denotes a surface site and an * symbol before a molecule denotes an adsorbed species.

CO pathway reaction mechanism is suggested to involve three fundamental steps, which are represented by the equations ((4-3), (4-4) and (4-5)).

The hydrogen evolution reaction (HER) was employed as a fundamental process for producing molecular hydrogen (H_2) through the electrochemical reduction of protons, which are represented by the equation (4-6).

Finally, after generating the diagrams and output files for the CO_2 reduction reaction (CO_2RR) on pure Sn (200) in the gas phase, it became possible to calculate and construct the corresponding diagram for the solvation phase by using solvation model [86,87], as well as repeat all this process into substitution and adatoms systems.

5.3 Results and discussion

5.3.1 Pure Sn (200)

The geometric and electronic configurations of reaction intermediates play a crucial role in governing the carbon dioxide reduction reaction (CO_2RR) on pure tin surfaces. As previously shown in Figure 22, the Sn (200) surface presents three possible adsorption sites: one top site and two bridge sites. For each adsorption site, the slab–adsorbate configurations were constructed and analysed using MATLAB software [124]. As an illustrative example, Figure 24 shows the adsorption configurations of the *COOH intermediate at the three distinct sites.

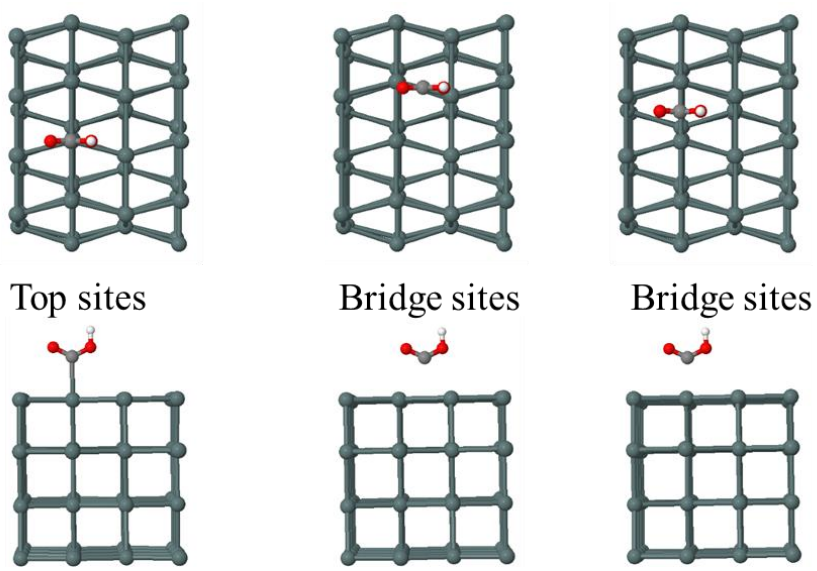

Fig. 24 Optimised structures of COOH adsorbed on Sn (200). The Sn, O, C and H atoms are represented with greyish turquoise, red, dark grey and white spheres respectively.

All adsorption sites were systematically evaluated for the relevant reaction pathways, including the CO pathway, the formate pathway, and the hydrogen evolution reaction (HER). In the CO pathway, the considered intermediates are CO_2, *COOH, and *CO + H_2O, whereas the formate pathway involves CO_2, *OCHO, and HCOOH. For the HER pathway, hydrogen adsorption (*H) was examined. For each pathway, the adsorption configuration corresponding to the lowest total energy was selected and used to construct the reaction energy diagrams discussed in the following sections.

To examine the reaction pathways leading to CO and formate formation, our calculations systematically investigated three key processes: the CO pathway, the formate pathway, and the competing hydrogen evolution reaction (HER). The initial hydrogenation step follows the adsorbed hydrogen transfer mechanism, in which surface-bound hydrogen interacts with adsorbed *CO_2 to form either *COOH or *OCHO intermediates. On the Sn (200) surface under gas-phase conditions, our calculated results show that the energy barrier for *COOH formation is approximately 0.81 eV, whereas *OCHO formation is energetically more favourable, exhibiting a much lower barrier of about -0.04 eV. When solvation effects are included, the

calculated energy barriers for both intermediates are reduced, with the *COOH barrier decreasing to around 0.70 eV and the *OCHO barrier to approximately -0.05 eV.

Further calculations reveal that the *COOH intermediate is unstable and proceeds to *CO via an H_2O-assisted hydrogen transfer mechanism, while *OCHO evolves into *HCOOH. The corresponding energy barriers in the gas phase are calculated to be 0.72 eV for the *COOH-to-*CO step and 0.50 eV for the *OCHO-to-*HCOOH step. Upon inclusion of solvation, these barriers decrease further to approximately 0.51 eV and 0.24 eV, respectively, highlighting the stabilising effect of the solvent environment on reaction intermediates.

In addition to the CO_2 reduction pathways, the competing HER was also considered. Our results indicate that the HER energy barrier is lower under solvated conditions, at approximately 0.03 eV, compared with the corresponding gas-phase value of 0.22 eV. Overall, these findings demonstrate the significant role of solvation in facilitating reaction kinetics by lowering the associated energy barriers. The calculated free-energy profiles of the key intermediates in the gas phase and under solvated conditions are presented in Figures 25A and 25B, respectively.

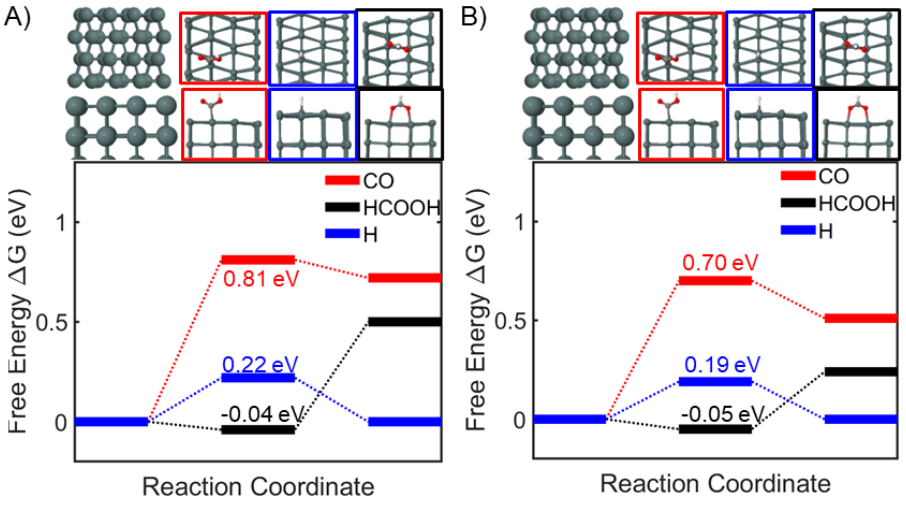

Fig. 25 The comparison between gas phase and solvation phase. The blue colour of line and farm are referred to HER, the black colour of line and farm are referred to formate pathway, and the red colour of line and farm are referred to CO pathway. The Sn, O, C and H atoms are represented with greyish turquoise, red, dark grey and white spheres respectively.

To further assess charge redistribution during the reaction, Bader charge and charge density difference analyses were performed for the *COOH and *OCHO intermediates, as shown in Figure 26 and summarised in Table 8. The Bader charge results clearly indicate electron transfer from the Sn active site to the adsorbed intermediates, confirming strong adsorbate–surface interactions. Specifically, the *COOH intermediate gains 0.46 e, accompanied by an equivalent charge loss from the Sn atom, suggesting moderate electron transfer and stabilization through adsorption. In contrast, the *OCHO intermediate exhibits a significantly larger charge gain of 0.74 e, indicating a stronger degree of electron transfer from the surface and a more pronounced interaction with the active site. These findings are consistent with the charge density difference plots, where distinct regions of electron accumulation on the intermediates and depletion around the Sn atom highlight the directionality of charge flow. Overall, the higher charge transfer observed for *OCHO suggests stronger electronic coupling with the surface compared to *COOH, which may influence its adsorption strength and play a key role in determining the preferred reaction pathway.

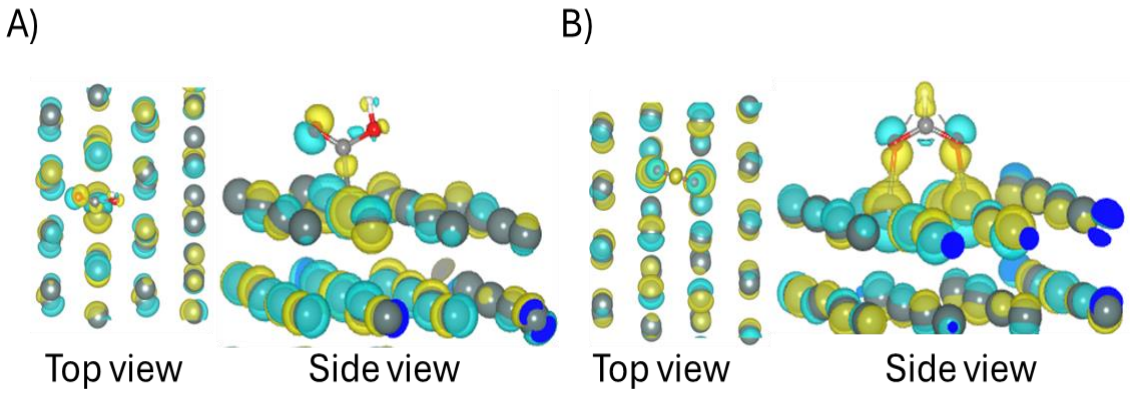

Fig. 26 The charge density difference. A) The charged density difference of COOH. B) The charged density difference of OCHO. The yellow and cyan regions depict the electron accumulation and depletion, respectively.

Table 8 Bader charge in COOH and OCHO situations.

System	COOH	Sn
Sn_{64}	Gains 0.46e	Loses 0.46e
System	OCHO	Sn
Sn_{64}	Gains 0.74e	Loses 0.74e

5.3.2 Bi substituted Sn

Following the analysis of the pristine Sn (200) surface, the effect of bismuth substitution was investigated by considering three distinct slab models with increasing levels of Bi incorporation. In the first model, a single Bi atom was substituted for a Sn atom, either at the surface layer or within the subsurface region of the Sn (200) slab. A comparison of these configurations shows that surface substitution is energetically more favourable than subsurface substitution, as illustrated in Figure 27. To ensure that the obtained structures correspond to low-energy configurations rather than local minima on the potential energy surface, multiple initial configurations were generated for each case and optimized independently. The final structures were then compared based on their converged E_0 values, and the lowest-energy configuration was identified as the most stable.

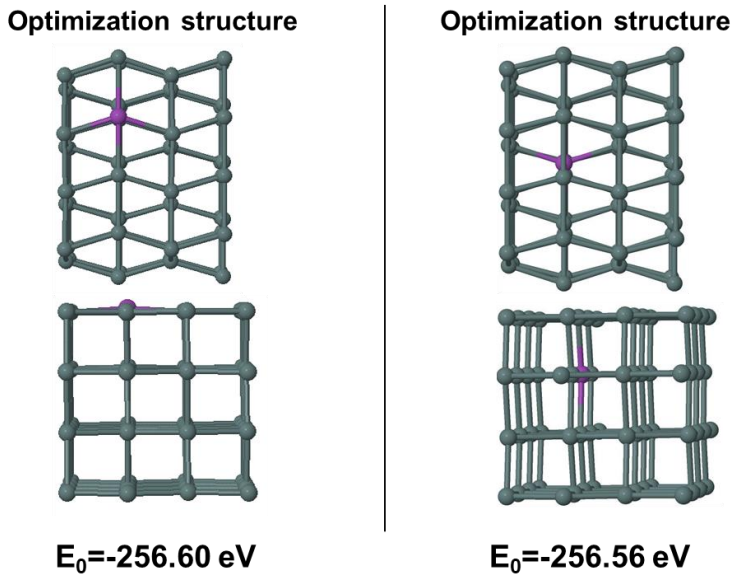

Fig. 27 Optimised structures of Bi_1Sn_{63}. The Sn and Bi atoms are represented with greyish turquoise and deep lilac spheres respectively. E_0 is the total energy extrapolated.

The second model involves the substitution of two Sn atoms with Bi atoms, while the third model consists of three Bi atoms replacing Sn atoms within the slab. The most stable configurations for the second and third substitution models are shown in Figures 28 and 29, respectively. In each case, several initial configurations were considered and optimized, and the lowest-energy structures were selected based on their converged E_0 values. This systematic approach enables evaluation of the influence of Bi concentration on the structural stability, electronic properties, and catalytic behaviour of the Sn surface.

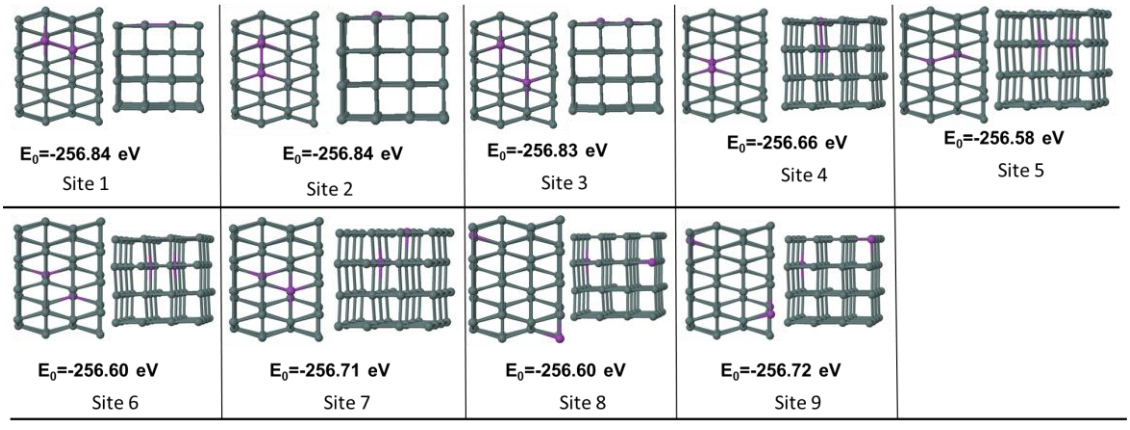

Fig. 28 Optimised structures of Bi_2Sn_{62}. The Sn and Bi atoms are represented with greyish turquoise and deep lilac spheres respectively. E_0 is the total energy extrapolated.

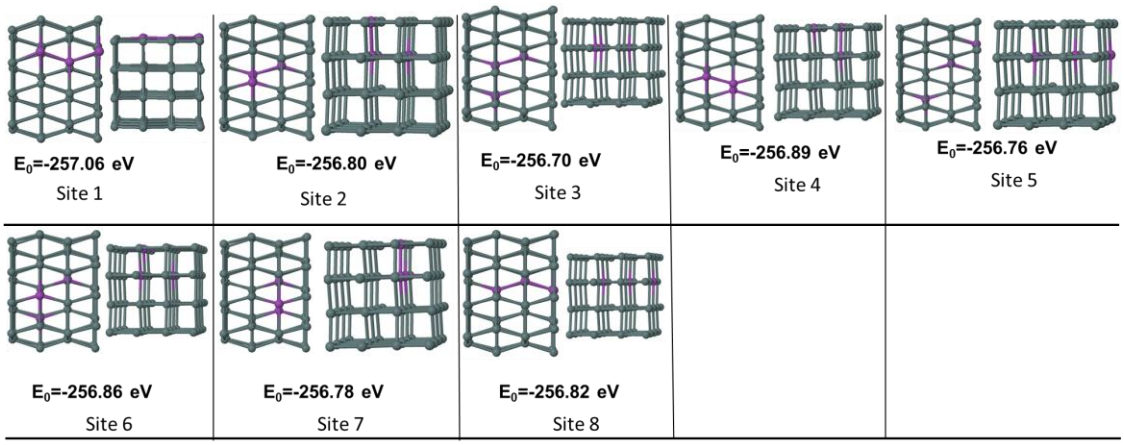

Fig. 29 Optimised structures of Bi_3Sn_{61}. The Sn and Bi atoms are represented with greyish turquoise and deep lilac spheres respectively. E_0 is the total energy extrapolated.

To examine charge redistribution resulting from Bi incorporation, Bader charge analysis was performed for the clean substituted surfaces, with the results presented in Table 9. The analysis indicates that increasing the number of substituted Bi atoms leads to enhanced charge transfer. By varying the Bi substitution level, the effects on reaction pathways, energy barriers, and overall catalytic efficiency can be assessed. Comparisons among these configurations provide insight into the role of Bi as a promoter or modifier of Sn-based catalysts, particularly in relation to the CO, formate, and hydrogen evolution pathways discussed previously.

Table 9 Bader charge in free metal situation.

System	Sn	Bi
Bi_1/Sn_{63}	Loses 0.08e	Gains 0.08e
Bi_2/Sn_{62}	Loses 0.11e	Gains 0.11e
Bi_3/Sn_{61}	Loses 0.12e	Gains 0.12e

In addition to the conventional adsorption sites, new binding sites emerge either directly above the substituted bismuth atoms or at the interface between tin and bismuth atoms. All such configurations were systematically examined, and the results indicate that adsorbates such as

*COOH, *OCHO, and *H preferentially bind to tin atoms rather than to bismuth atoms. As an illustrative example, Figure 30 presents the total energy differences associated with *OCHO adsorption at the various available sites, clearly demonstrating the energetic preference for tin-associated binding configurations.

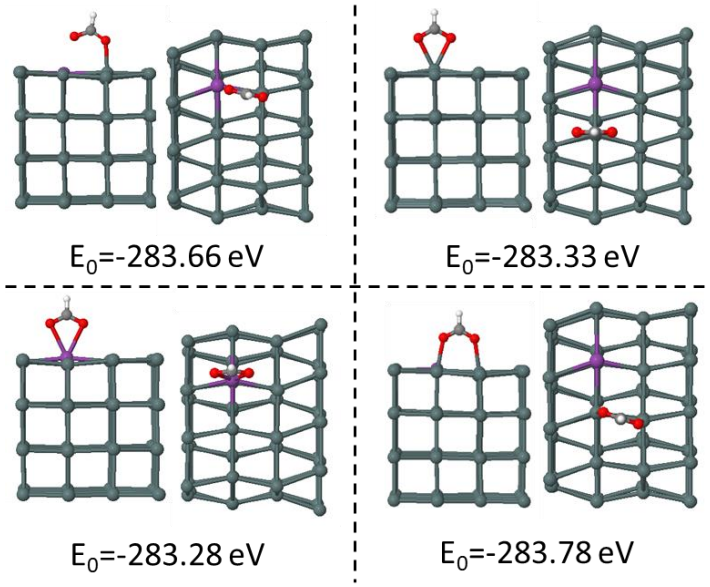

Fig. 30 Optimised structures of OCHO on Bi_1Sn_{63} in different sites. The Sn, Bi, O, C and H atoms are represented with greyish turquoise, deep lilac, red, dark grey and white spheres respectively. E_0 is the total energy extrapolated.

A comparison of the three bismuth-substituted tin slabs reveals pronounced changes in reaction pathways and energy barriers relative to the pristine Sn surface. For the slab containing a single substituted Bi atom under gas-phase conditions, the energy barrier associated with *COOH formation increases by approximately 0.10 eV, indicating a higher activation energy for the CO pathway. Similarly, the hydrogen evolution reaction (HER) exhibits an increased energy barrier of about 0.40 eV. In contrast, formic acid formation remains slightly favoured, with an energy barrier of approximately 0.08 eV, suggesting enhanced thermodynamic stability of the HCOOH pathway for this configuration.

When two Bi atoms are substituted, the energy barriers increase further for all intermediates under gas-phase conditions. Despite this overall increase in activation energies, the system continues to favour HCOOH formation as the most stable reaction pathway, while both the CO and HER pathways become increasingly suppressed. This trend indicates that increasing Bi substitution promotes selectivity toward formate production at the expense of competing reactions.

For the slab with three substituted Bi atoms, the gas-phase energy barriers exceed those observed for the one- and two-Bi substitution cases. Under solvated conditions, the energy barriers for all intermediates are higher than those on the pristine Sn surface; however, the energy differences between the *COOH and HCOOH intermediates become relatively small. This convergence suggests that the system can readily progress toward formic acid formation despite the higher absolute barriers.

The calculated energy profiles for these reaction mechanisms under gas-phase and solvated conditions are shown in Figures 31A and 31B, respectively, providing a comprehensive view of the energetic landscape.

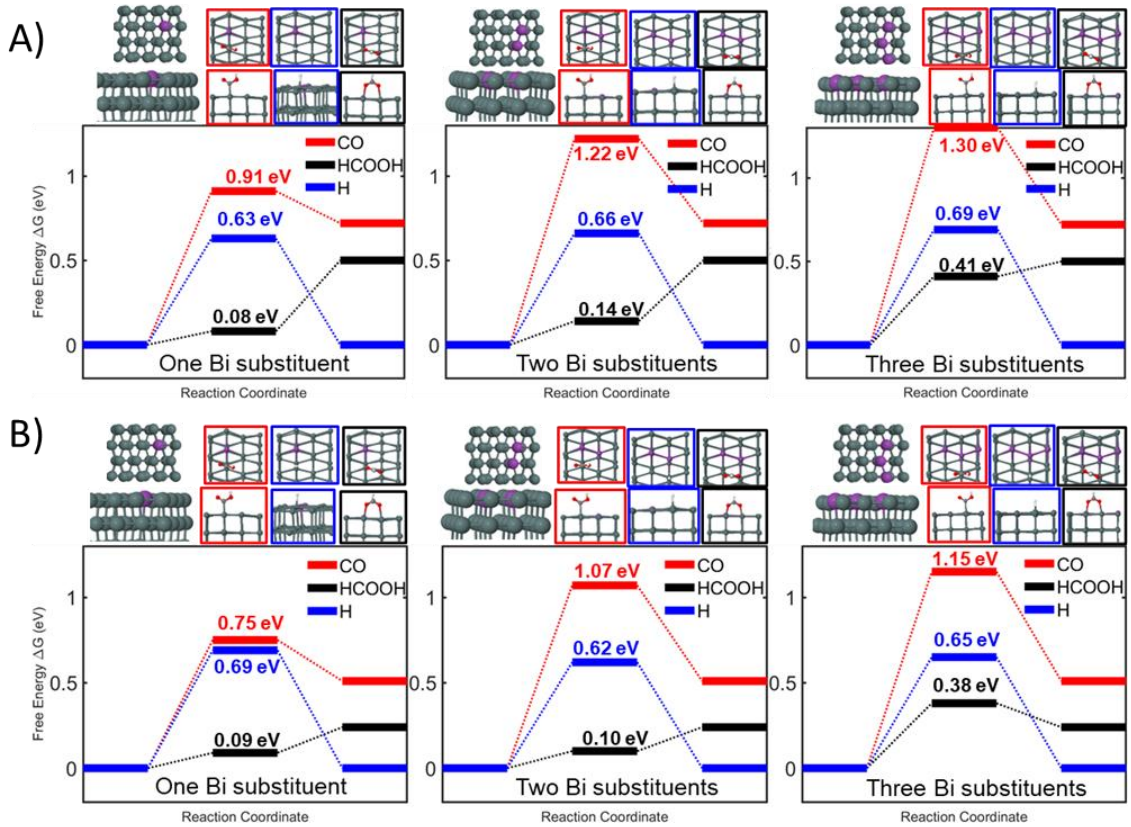

Fig. 31 The comparison between Bi_1Sn_{63}, Bi_2Sn_{62} and Bi_3Sn_{61} in gas phase and solvation phase. The blue colour of line and farm are referred to HER, the black colour of line and farm are referred to formate pathway, the red colour of line and farm are referred to CO pathway. The Sn, Bi, O, C and H atoms are represented with greyish turquoise, deep lilac, red, dark grey and white spheres respectively.

To further elucidate the electronic effects of Bi incorporation, Bader charge analysis was performed for the *COOH and *OCHO intermediates, with the results summarised in Table 10, while the corresponding charge density difference plots are presented in Figure 32. The analysis shows that for all systems, electron transfer occurs predominantly from the Sn surface to the adsorbed intermediates, accompanied by partial charge accumulation on the substituted Bi atoms. For the *COOH intermediate, the adsorbate gains approximately 0.44–0.47 e, while Sn loses 0.53–0.60 e, and Bi atoms gain a smaller but increasing fraction of charge (from 0.06 to 0.15 e) with higher Bi content. A similar trend is observed for *OCHO, where the adsorbate gains a larger amount of charge (0.72–0.74 e), with Sn losing 0.82–0.90 e and Bi gaining 0.08–0.16 e. Notably, the progressive increase in charge accumulation on Bi atoms with increasing substitution level indicates enhanced electronic participation of Bi in the adsorption process.

This redistribution of charge suggests that Bi acts as an electron reservoir, modifying the local electronic environment and weakening the direct interaction between the intermediates and Sn sites. These findings are consistent with the charge density difference plots and correlate with the observed increase in activation barriers and the enhanced selectivity toward formic acid formation, particularly through stabilization of the *OCHO intermediate.

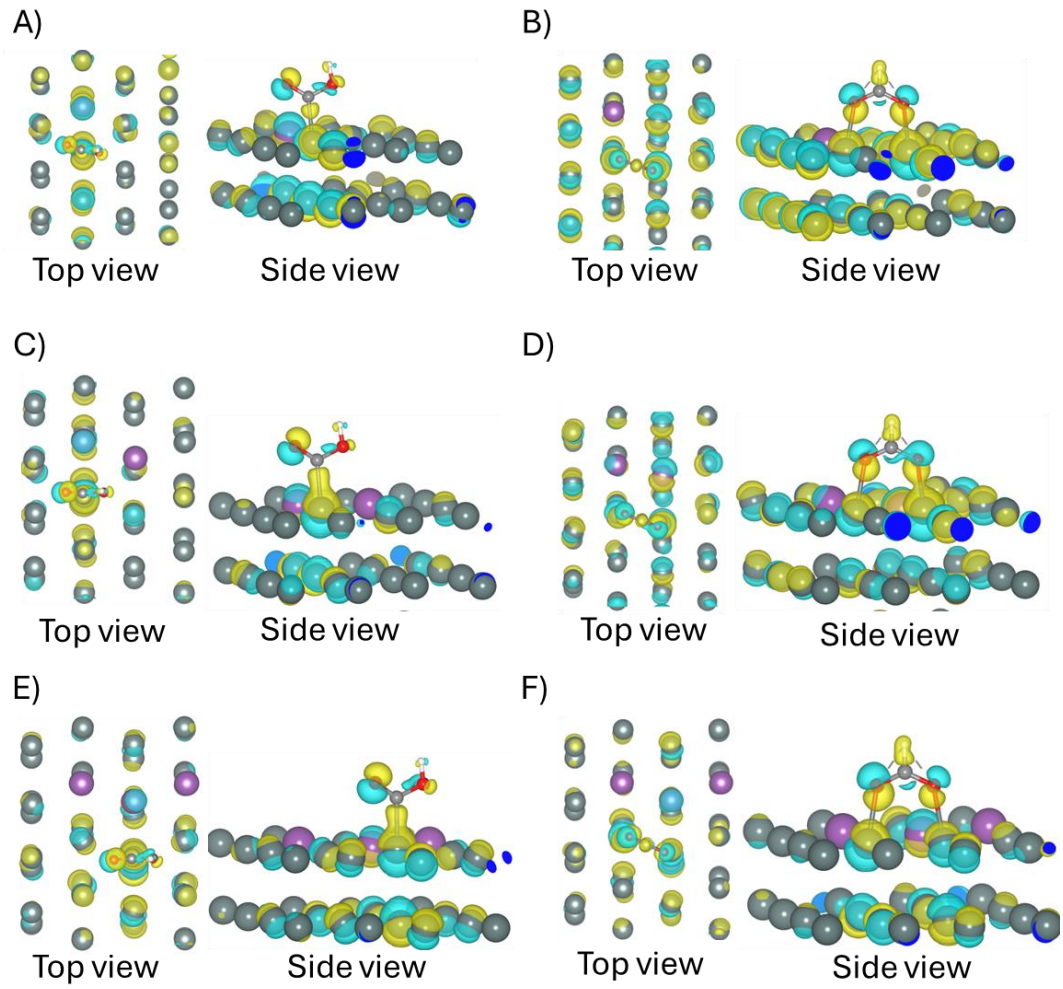

Fig. 32 The charge density difference. A) and B) The charged density difference of COOH and OCHO, respectively, on Bi_1Sn_{63}. C) and D) The charged density difference of COOH and OCHO, respectively, on Bi_2Sn_{62}. E) and F) The charged density difference of COOH and OCHO, respectively, on Bi_3Sn_{61}. The yellow and cyan regions depict the electron accumulation and depletion, respectively.

Table 10 Bader charge in COOH and OCHO situations.

System	COOH	Sn	Bi
Bi_1/Sn_{63}	Gains 0.47e	Loses 0.53e	Gains 0.06e
Bi_2/Sn_{62}	Gains 0.44e	Loses 0.53e	Gains 0.09e
Bi_3/Sn_{61}	Gains 0.45e	Loses 0.60e	Gains 0.15e
System	OCHO	Sn	Bi
Bi_1/Sn_{63}	Gains 0.74e	Loses 0.82e	Gains 0.08e
Bi_2/Sn_{62}	Gains 0.72e	Loses 0.84e	Gains 0.12e
Bi_3/Sn_{61}	Gains 0.74e	Loses 0.90e	Gains 0.16e

Finally, Table 11 presents the values of the DFT total energies (E_{DFT}), zero-point energies (E_{ZPE}), entropies (TS) at temperature (T = 298.15 K), free energies (G) and adsorption energy (E_{abs}).

Table 11 The values of the DFT total energies (E_{DFT}), zero-point energies (E_{ZPE}), entropies (TS) at temperature (T = 298.15 K), free energies (G) and adsorption energy (E_{abs}).

Catalysts	E_{DFT}	E_{ZPE}	TS	G	E_{ads}
			Bi_1/Sn_{63}		
$*CO_2$	-279.80	0.35	0.14	-279.59	0.19
*COOH	-283.16	0.62	0.16	-282.70	-1.96
*OCHO	-283.82	0.61	0.15	-283.36	-2.94
*H	-259.50	0.20	0.00	-259.30	0.49
			Bi_2/Sn_{62}		
$*CO_2$	-280.02	0.34	0.21	-279.81	0.21
*COOH	-283.07	0.62	0.17	-282.62	-1.63
*OCHO	-284.00	0.62	0.21	-283.59	-2.88
*H	-259.72	0.14	0.03	-259.61	0.51
			Bi_3/Sn_{61}		
$*CO_2$	-280.23	0.35	0.20	280.08	0.23
*COOH	-283.26	0.61	0.12	-282.77	-1.59
*OCHO	-283.99	0.61	0.16	-283.64	-2.64
*H	-259.90	0.14	0.03	-259.81	0.56

5.3.3 Bi adatom on Sn

Following the investigation of bismuth substitution, the effect of bismuth adatoms on tin surfaces was examined by considering three distinct slab configurations with increasing numbers of Bi atoms. In the first configuration, a single bismuth atom was adsorbed on the Sn (200) surface. Several possible adsorption sites were evaluated, including top, bridge, and hollow sites. The results indicate that the bismuth atom preferentially adsorbs at the hollow site, as illustrated in Figure 33 and the lowest-energy structures were selected based on their converged E_0values.

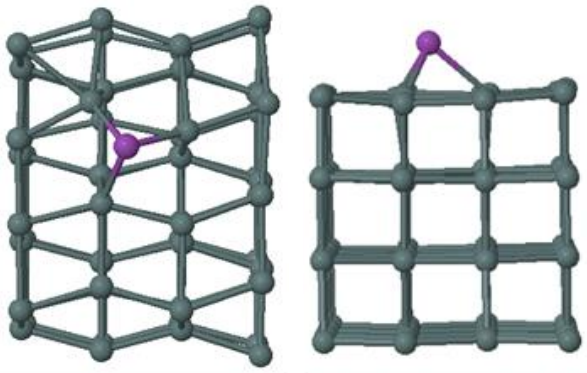

Fig. 33 Optimised structures of Bi_1Sn_{64}. The Sn and Bi atoms are represented with greyish turquoise and deep lilac spheres respectively. E_0 is the total energy extrapolated.

The second configuration, referred to as the dimer, involves the adsorption of two bismuth atoms on the tin surface. In this case, the Bi atoms can adopt either transverse or longitudinal arrangements relative to the surface lattice, with the corresponding geometries shown in Figure 34. The third configuration, termed the trimer, consists of three bismuth atoms adsorbed on the tin surface, and the optimised geometries for this system are presented in Figure 35. In each case, several initial configurations were considered and optimized, and the lowest-energy structures were selected based on their converged E_0values.

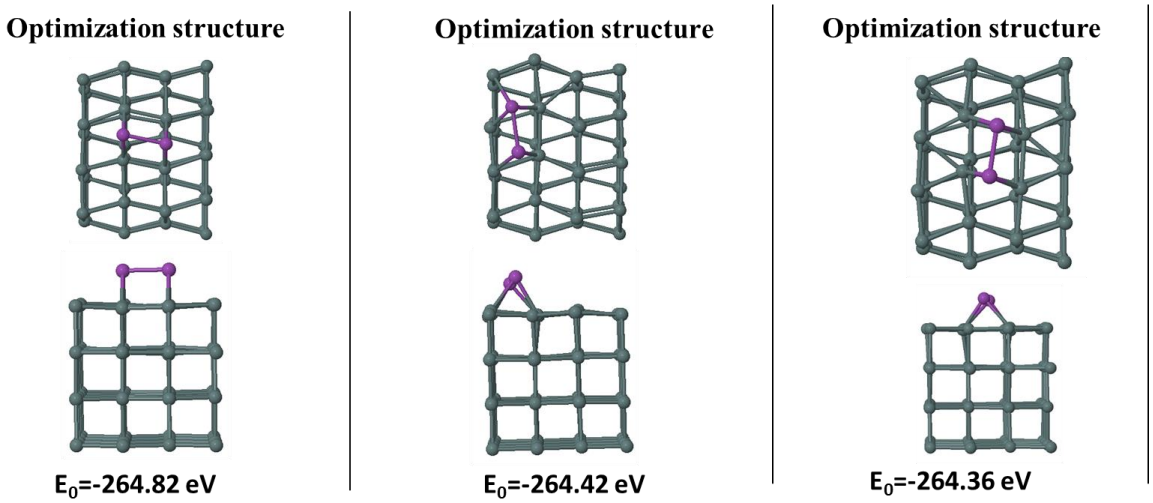

Fig. 34 Optimised structures of Bi_2Sn_{64}. The Sn and Bi atoms are represented with greyish turquoise and deep lilac spheres respectively. E_0 is the total energy extrapolated.

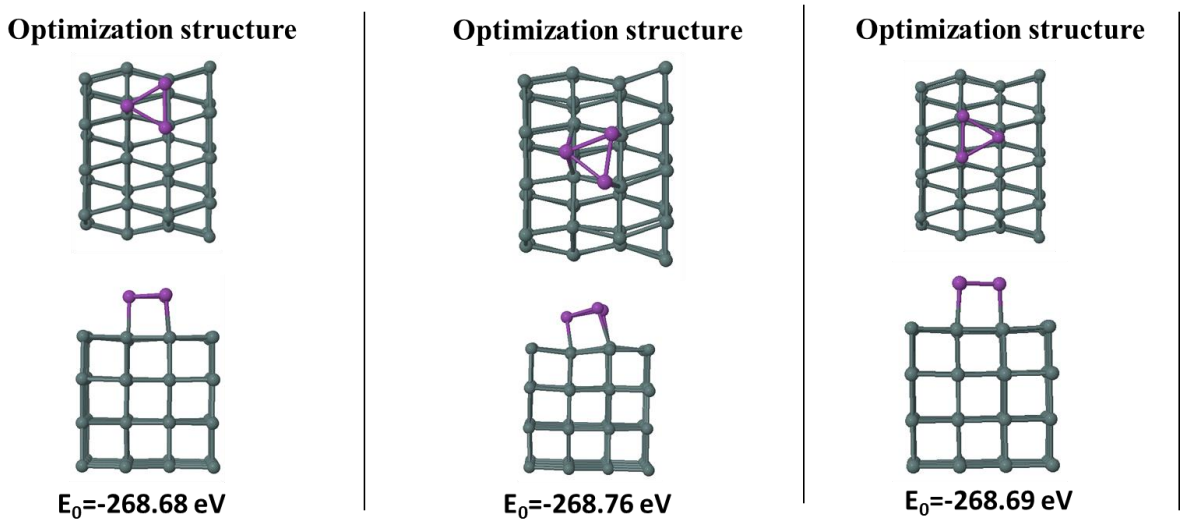

Fig. 35 Optimised structures of Bi_3Sn_{64}. The Sn and Bi atoms are represented with greyish turquoise and deep lilac spheres respectively. E_0 is the total energy extrapolated.

To examine charge redistribution induced by Bi adatom incorporation, Bader charge analysis was performed for the Bi adatoms and the Sn substrate, with the results summarised in Table 12. The analysis indicates that charge transfer is lowest for a single Bi adatom, increases with the addition of a second Bi atom, and decreases again when three Bi atoms are present. This non-monotonic behaviour highlights the sensitivity of the electronic structure and charge distribution to both the number and spatial arrangement of bismuth adatoms on the tin surface.

Table 12 Bader charge in free metal situation.

System	Sn	Bi
Bi_1/Sn_{64}	Loses 0.08e	Gains 0.08e
Bi_2/Sn_{64}	Loses 0.13e	Gains 0.13e
Bi_3/Sn_{64}	Loses 0.08e	Gains 0.08e

The results demonstrate that the incorporation of bismuth significantly modifies the reaction behaviour, particularly under gas-phase conditions. For configurations involving a single Bi atom, either substituted into the lattice or adsorbed as an adatom, the energy barriers associated with all reaction pathways increase markedly. This increase shifts the selectivity toward formic acid formation and suppresses the CO pathway. In contrast, for the dimer configuration, the energy barriers remain comparable to those of the two substituted atoms, while for the trimer configuration, the energy barriers decrease, indicating a more favourable reaction pathway.

Under solvated conditions, all three Bi-modified configurations exhibit slightly higher energy barriers relative to their gas-phase counterparts; however, the overall trends observed in the gas phase are preserved. The calculated energy profiles for these mechanisms in the gas-phase and solvated environments are presented in Figures 36A and 36B, respectively, providing a clear comparison of the energetic landscapes.

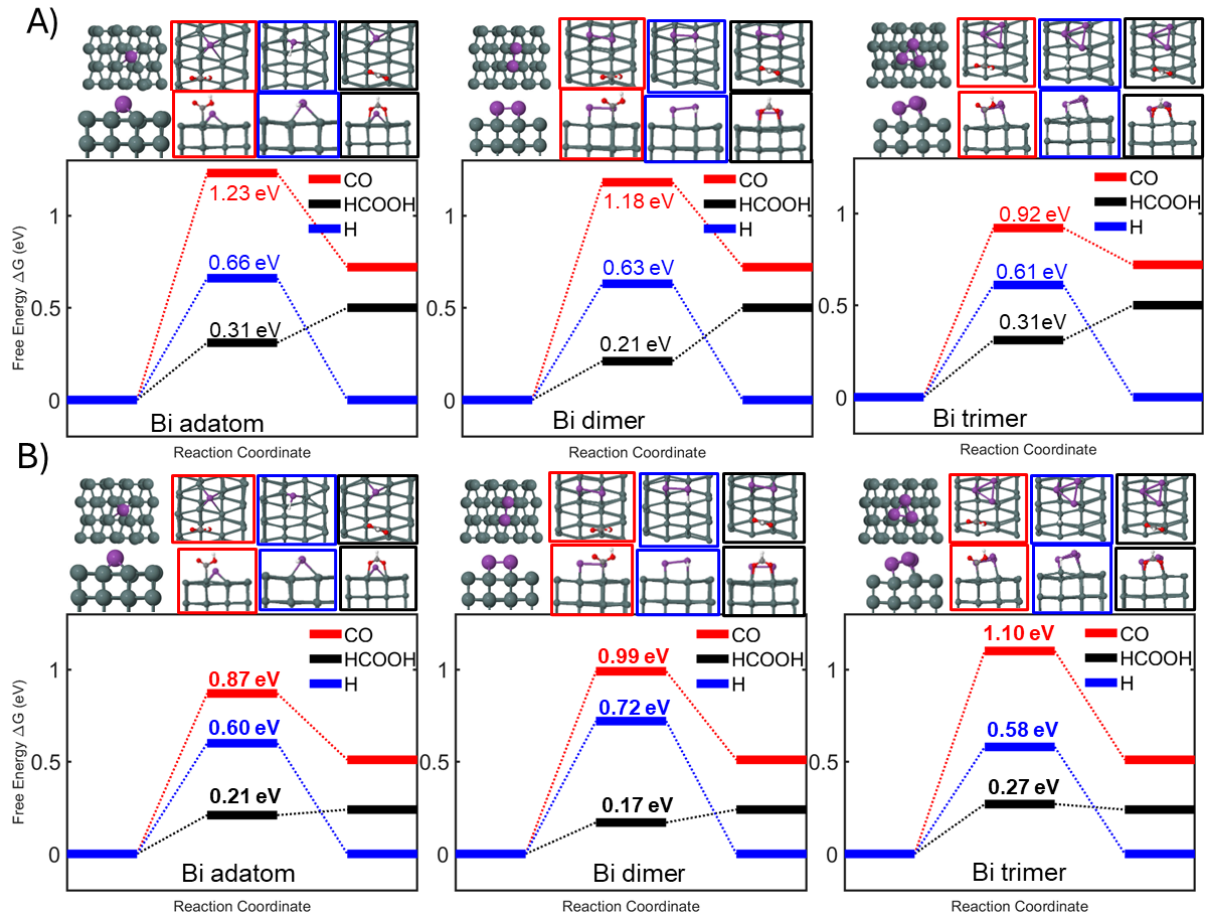

Fig. 36 The comparison between Bi_1Sn_{64}, Bi_2Sn_{64} and Bi_3Sn_{64} in gas phase and solvation phase. The blue colour of line and farm are referred to HER, the black colour of line and farm are referred to formate pathway, the red colour of line and farm are referred to CO pathway. The Sn, Bi, O, C and H atoms are represented with greyish turquoise, deep lilac, red, dark grey and white spheres respectively.

To assess charge redistribution effects, Bader charge analysis was performed for the *COOH and *OCHO intermediates, with the results summarised in Table 13, while the corresponding charge density difference plots are shown in Figure 37. The analysis indicates that electron transfer predominantly occurs from the Sn surface to both intermediates, accompanied by partial charge accumulation on Bi atoms. For the *COOH intermediate, the adsorbate gains 0.45–0.50 e, while Sn loses 0.56–0.59 e, and Bi atoms gain a smaller but progressively increasing amount of charge from 0.07 to 0.14 e as the Bi content increases. A similar trend is observed for *OCHO, where the adsorbate gains a larger charge (0.73–0.77 e), with Sn losing 0.80–0.86 e and Bi atoms gaining 0.08–0.13 e for Bi1 and Bi2 configurations. However, in the Bi3/Sn64 system, the charge accumulation on Bi decreases to 0.03 e, suggesting a possible

redistribution of charge back toward the adsorbate or Sn atoms at higher Bi concentrations. Overall, these results confirm that Bi incorporation modifies the electronic environment by acting as an electron-accepting site, thereby influencing the charge transfer pathway. This redistribution correlates with the observed increase in energy barriers and enhanced selectivity toward formic acid formation, particularly through modulation of the *OCHO intermediate interaction.

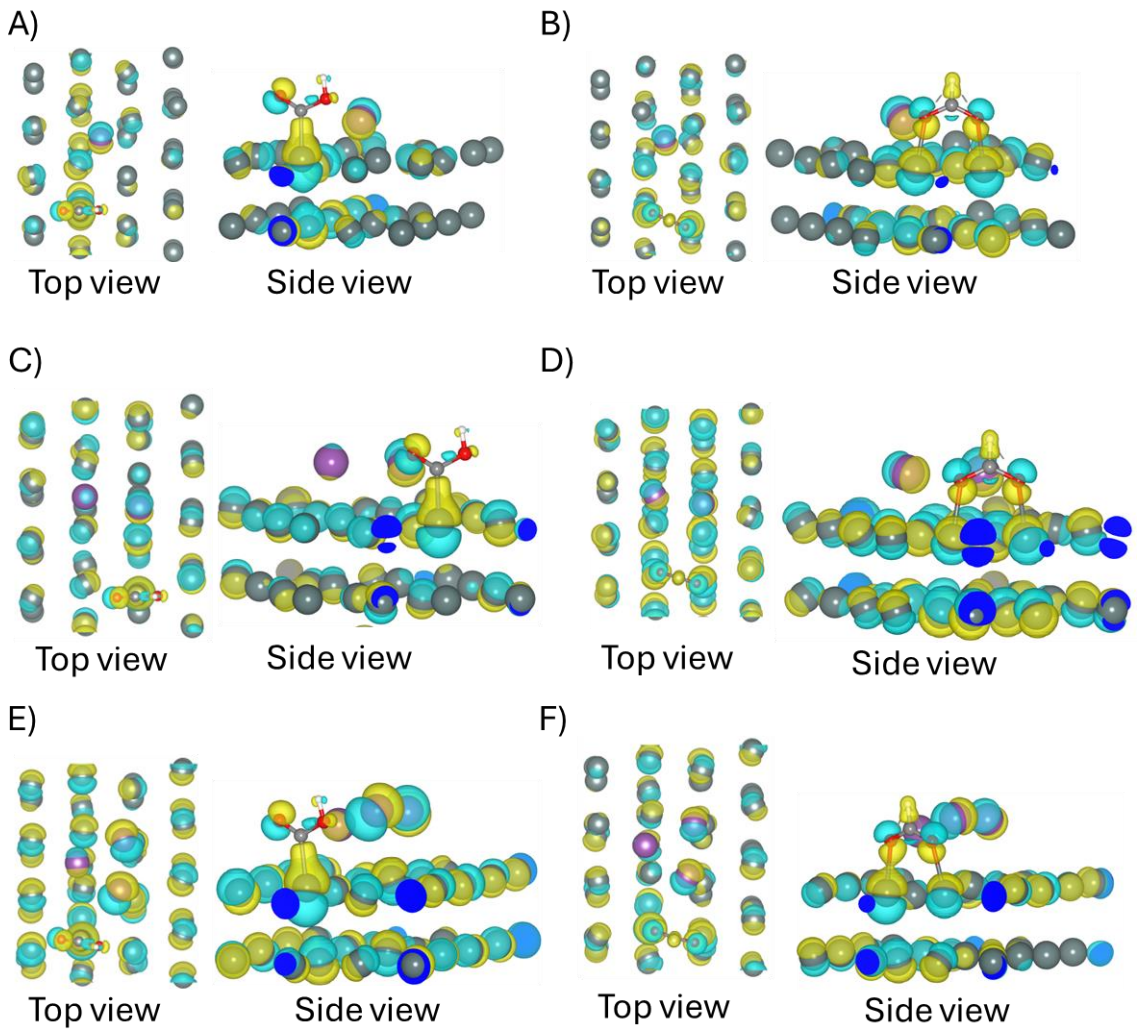

Fig. 37 The charge density difference. A and B) The charged density difference of COOH and OCHO, respectively, on Bi_1Sn_{64}. C and D) The charged density difference of COOH and OCHO, respectively, on Bi_2Sn_{64}. E and F) The charged density difference of COOH and OCHO, respectively, on Bi_3Sn_{64}. The yellow and cyan regions depict the electron accumulation and depletion, respectively.

Table 13 Bader charge in COOH and OCHO situations.

System	COOH	Sn	Bi
Bi_1/Sn_{64}	Gains 0.50e	Loses 0.57e	Gains 0.07e
Bi_2/Sn_{64}	Gains 0.45e	Loses 0.56e	Gains 0.11e
Bi_3/Sn_{64}	Gains 0.45e	Loses 0.59e	Gains 0.14e
System	OCHO	Sn	Bi
Bi_1/Sn_{64}	Gains 0.73e	Loses 0.82e	Gains 0.08e
Bi_2/Sn_{64}	Gains 0.73e	Loses 0.86e	Gains 0.13e
Bi_3/Sn_{64}	Gains 0.77e	Loses 0.80e	Gains 0.03e

Finally, Table 14 presents the values of the DFT total energies (E_{DFT}), zero-point energies (E_{ZPE}), entropies (TS) at temperature (T=298.15 K), free energies (G) and adsorption energy (E_{abs}).

Table 14 The values of the DFT total energies (E_{DFT}), zero-point energies (E_{ZPE}), entropies (TS) at temperature (T = 298.15 K), free energies (G) and adsorption energy (E_{abs}).

Catalysts	E_{DFT}	E_{ZPE}	TS	G	E_{ads}
			Bi_1/Sn_{64}		
$*CO_2$	-283.85	0.33	0.11	-283.74	0.14
*COOH	-286.99	0.62	0.21	-286.58	-1.79
*OCHO	-287.65	0.62	0.21	-287.24	-2.77
*H	-263.50	0.14	0.03	-263.39	0.49
			Bi_2/Sn_{64}		
$*CO_2$	-288.05	0.33	0.12	287.84	0.17
*COOH	-291.16	0.62	0.15	290.69	-1.73
*OCHO	-291.94	0.62	0.19	291.51	-2.83
*H	-267.70	0.14	0.03	-267.59	0.52
			Bi_3/Sn_{64}		
$*CO_2$	-291.99	0.34	0.16	291.81	0.15
*COOH	-295.00	0.62	0.14	-294.52	-1.39
*OCHO	-295.78	0.62	0.19	-295.35	-2.62
*H	-271.72	0.14	0.03	-271.61	0.50

5.4 Conclusion

In this study, the effect of incorporating bismuth (Bi) atoms into the Sn (200) surface on catalytic performance for CO_2 reduction was systematically investigated using density functional theory calculations. Both adsorption and substitution strategies were examined to understand how local atomic configurations influence reaction energetics and selectivity.

The results confirm that pristine Sn strongly favours the formate (*OCHO) pathway; however, competing reactions such as CO formation and the hydrogen evolution reaction (HER) remain significant. The introduction of Bi alters the reaction landscape by increasing the energy barriers for *COOH formation and hydrogen adsorption, thereby suppressing undesired pathways and enhancing selectivity toward formic acid production under both gas-phase and solvated conditions. Among the configurations studied, Bi adsorption on the surface provides the most favourable catalytic performance.

In comparison with previous studies, which largely focused on bulk alloys or high Bi loadings, the present work demonstrates that improved selectivity can be achieved with minimal Bi incorporation. While earlier research reported enhanced CO_2 reduction performance with increasing Bi content, our findings show that similar trends can be obtained at much lower concentrations, accompanied by reduced energy barriers for key intermediates. This highlights the critical role of local atomic structure rather than overall composition in determining catalytic behaviour.

Overall, this work provides new insight into the design of Sn-based catalysts, showing that strategic, low-level Bi modification is an effective approach for optimizing catalytic efficiency and selectivity. These findings contribute to the rational development of advanced materials for sustainable CO_2 utilization and renewable energy applications.

6.Summary and Future Work

This thesis has presented a comprehensive investigation into the electrochemical reduction of carbon dioxide, with particular emphasis on the role of surface modification in tuning catalytic activity and selectivity. The results demonstrate that the incorporation of atomic clusters on silver substrates significantly lowers reaction energy barriers, leading to enhanced catalytic performance. In particular, gold clusters deposited on silver surfaces exhibit a more pronounced reduction in energy barriers compared with silver clusters, highlighting their strong potential for catalyst optimisation.

A key finding of this work is that the combination of different materials, specifically gold with silver, leads to a significant enhancement in catalytic activity beyond what is typically expected from the individual components. Moreover, an unexpected observation is that the behaviour of the clusters varies not only with size but also strongly with composition: the trend in catalytic performance between small and large clusters changes when the material is altered, indicating a complex interplay between cluster size and electronic structure.

The binding strength of the key *COOH intermediate was found to depend strongly on both cluster size and composition. While larger silver clusters exhibited slightly lower binding energies than smaller ones, gold clusters showed consistently higher binding energies, which correlated with reduced activation barriers and improved catalytic activity.

For tin-based catalysts, the *OCHO intermediate displayed strong binding on pristine Sn surfaces, resulting in hindered formic acid release. The introduction of bismuth, either through substitution or surface modification, significantly improved selectivity towards formic acid formation. In particular, substitution with two bismuth atoms yielded the highest selectivity for the desired product. Increasing bismuth content led to a systematic reduction in *OCHO binding energy, facilitating product desorption and enhancing overall catalytic efficiency.

The results presented in this thesis form the basis for ongoing work and are expected to be published in the near future in collaboration with VITO.

Future Work:

Future research could extend these findings by exploring alternative substrate–cluster combinations to further optimise catalytic activity and selectivity. One promising direction involves replacing the silver substrate with gold and applying similar cluster modification strategies to evaluate whether superior catalytic performance can be achieved. In addition, copper-based substrates merit particular attention due to copper's unique ability to produce a broader range of carbon-based products during CO_2 reduction. Systematic investigations of copper substrates decorated with metal clusters, including silver, gold, or bismuth clusters, could provide valuable insights into how cluster–substrate interactions influence reaction pathways, product distribution, and selectivity.

Although other metals such as platinum and Rhodium are catalytically active, they are generally less suitable for CO_2 reduction because they favour the hydrogen evolution reaction and tend to bind intermediates too strongly, which reduces selectivity. For this reason, research has focused more on metals like Au, Ag, Cu, Sn, and Bi.

Furthermore, the tin–bismuth system could be expanded by introducing tin atoms onto bismuth surfaces, enabling a complementary assessment of charge transfer and binding energetics. Such studies would deepen the understanding of synergistic effects between different metallic components and support the rational design of next generation electrocatalysts for efficient and sustainable CO_2 conversion.

7. Bibliography

1. Team GW. Trends in CO2 - NOAA Global Monitoring Laboratory [Internet]. 2024. Available from: https://gml.noaa.gov/ccgg/trends/
2. NOAA National Centers for Environmental Information (2024). Annual 2024 Global Climate Report. Accessed May 21, 2025, from https://www.ncei.noaa.gov/access/monitoring/monthly-report/global/202413.
3. Vary Z, Mullins E, McElwain JC, Doohan FM. The severity of wheat diseases increases when plants and pathogens are acclimatized to elevated carbon dioxide. Global change biology. 2015 Jul;21(7):2661-9.
4. Li X, Ulfat A, Lv Z, Fang L, Jiang D, Liu F. Effect of multigenerational exposure to elevated atmospheric CO2 concentration on grain quality in wheat. Environmental and Experimental Botany. 2019 Jan 1;157:310-9.
5. Spafford L, MacDougall AH. Quantifying the probability distribution function of the transient climate response to cumulative CO2 emissions. Environmental Research Letters. 2020 Mar 5;15(3):034044.
6. Liu Q, Yang X, Li L, Miao S, Li Y, Li Y, Wang X, Huang Y, Zhang T. Direct catalytic hydrogenation of CO2 to formate over a Schiff-base-mediated gold nanocatalyst. Nature communications. 2017 Nov 10;8(1):1407.
7. Shi J, Jiang Y, Jiang Z, Wang X, Wang X, Zhang S, Han P, Yang C. Enzymatic conversion of carbon dioxide. Chemical Society Reviews. 2015;44(17):5981-6000.
8. Habisreutinger SN, Schmidt-Mende L, Stolarczyk JK. Photocatalytic reduction of CO2 on TiO2 and other semiconductors. Angewandte Chemie International Edition. 2013 Jul 15;52(29):7372-408.
9. Zhu DD, Liu JL, Qiao SZ. Recent advances in inorganic heterogeneous electrocatalysts for reduction of carbon dioxide. Advanced materials. 2016 May;28(18):3423-52.
10. Zhang S, Liu X, Wang M, Wu B, Pan B, Yang H, Yu HQ. Diketone-mediated photochemical processes for target-selective degradation of dye pollutants. Environmental Science & Technology Letters. 2014 Feb 11;1(2):167-71

11. Ma Q, Luo L, Wang RZ, Sauce G. A review on transportation of heat energy over long distance: Exploratory development. Renewable and Sustainable Energy Reviews. 2009 Aug 1;13(6-7):1532-40.
12. Ridjan I, Hansen K, Sorknæs P, Xu J, Connolly D, Mathiesen BV. The role of electrolysers in energy system: Energy markets, grid stabilisation and transport fuels.
13. Wang L, Chen M, Küngas R, Lin TE, Diethelm S, Maréchal F. Power-to-fuels via solid-oxide electrolyzer: Operating window and techno-economics. Renewable and Sustainable Energy Reviews. 2019 Aug 1;110:174-87.
14. Alvarez-Gomez JM, Varela AS. Review on long-term stability of electrochemical CO2 reduction. Energy & Fuels. 2023 Oct 5;37(20):15283-308.
15. Bagchi D, Roy S, Sarma SC, C. Peter S. Toward unifying the mechanistic concepts in electrochemical CO2 reduction from an integrated material design and catalytic perspective. Advanced Functional Materials. 2022 Dec;32(51):2209023.
16. Küngas R. electrochemical CO2 reduction for CO production: comparison of low-and high-temperature electrolysis technologies. Journal of The Electrochemical Society. 2020 Feb 14;167(4):044508.
17. Eren EO, Özkar S. Recent advances in heterogeneous catalysts for the effective electroreduction of carbon dioxide to carbon monoxide. Journal of Power Sources. 2021 Sep 15;506:230215.
18. Josipovic L, Alyones D, Roybal S, Sun Q, Fei Y, Zhou M, Luo H. Development of Catalysts for the Electrochemical CO2 Reduction Reaction. Inorganics. 2025 Aug 21;13(8):276.
19. Adegoke KA, Tseki PF. Electrochemical CO2 conversion to C1 and C2 products on defective metal electrocatalysts. Journal of CO2 Utilization. 2025 Nov 1;101:103201.
20. Xu D, Li K, Jia B, Sun W, Zhang W, Liu X, Ma T. Electrocatalytic CO2 reduction towards industrial applications. Carbon Energy. 2023 Jan;5(1):e230.
21. Zhang X, Guo SX, Gandionco KA, Bond AM, Zhang J. Electrocatalytic carbon dioxide reduction: from fundamental principles to catalyst design. Materials Today Advances. 2020 Sep 1;7:100074.
22. Daiyan R, Lu X, Ng YH, Amal R. Liquid hydrocarbon production from CO2: Recent development in metal-based electrocatalysis. ChemSusChem. 2017 Nov 23;10(22):4342-58.
23. Hussain J, Jónsson H, Skúlason E. Calculations of product selectivity in electrochemical CO2 reduction. Acs Catalysis. 2018 Apr 23;8(6):5240-9.

24. Khezri B, Fisher AC, Pumera M. CO 2 reduction: the quest for electrocatalytic materials. Journal of Materials Chemistry A. 2017;5(18):8230-46.
25. Feaster JT, Shi C, Cave ER, Hatsukade T, Abram DN, Kuhl KP, Hahn C, Nørskov JK, Jaramillo TF. Understanding selectivity for the electrochemical reduction of carbon dioxide to formic acid and carbon monoxide on metal electrodes. Acs Catalysis. 2017 Jul 7;7(7):4822-7.
26. Pathak B, Sarma N, Handique KC, Das H, Saikia P, Kalita PK. Nanomaterials for electrochemical CO2 conversion: mechanistic insights and emerging hybrid strategies. Emergent Materials. 2025 Oct 22:1-38.
27. Yang X, Xiang X, Zhou L, Fan J, Chen J, Liu Y, Zhou C, Fan W, Han M, Pu Z, Xia BY. Catalyst design strategies for highly efficient CO2 electroreduction. Coordination Chemistry Reviews. 2025 Aug 1;536:216650.
28. Bhuyan P, Ledendecker M. A perspective on tailoring grain boundaries to enhance the electrochemical performance of catalytic materials. Materials & Design. 2025 Jul 12:114388.
29. Gong Q, Ding P, Xu M, Zhu X, Wang M, Deng J, Ma Q, Han N, Zhu Y, Lu J, Feng Z. Structural defects on converted bismuth oxide nanotubes enable highly active electrocatalysis of carbon dioxide reduction. Nature communications. 2019 Jun 26;10(1):2807.
30. Ren B, Wen G, Gao R, Luo D, Zhang Z, Qiu W, Ma Q, Wang X, Cui Y, Ricardez–Sandoval L, Yu A. Nano-crumples induced Sn-Bi bimetallic interface pattern with moderate electron bank for highly efficient CO2 electroreduction. Nature communications. 2022 May 5;13(1):2486.
31. Roy X, Lee CH, Crowther AC, Schenck CL, Besara T, Lalancette RA, Siegrist T, Stephens PW, Brus LE, Kim P, Steigerwald ML. Nanoscale atoms in solid-state chemistry. Science. 2013 Jul 12;341(6142):157-60.
32. Zhou M, Higaki T, Hu G, Sfeir MY, Chen Y, Jiang DE, Jin R. Three-orders-of-magnitude variation of carrier lifetimes with crystal phase of gold nanoclusters. Science. 2019 Apr 19;364(6437):279-82.
33. Zhou M, Jin R, Sfeir MY, Chen Y, Song Y, Jin R. Electron localization in rod-shaped triicosahedral gold nanocluster. Proceedings of the National Academy of Sciences. 2017 Jun 13;114(24):E4697-705.

34. Roach PJ, Woodward WH, Castleman Jr AW, Reber AC, Khanna SN. Complementary active sites cause size-selective reactivity of aluminum cluster anions with water. Science. 2009 Jan 23;323(5913):492-5.
35. Wu H, Zhang H, Geng L, Jia Y, Huang B, Yang M, Yin B, Lei X, Luo Z. Pure metal clusters with atomic precision for nanomanufacturing. Nanomanufacturing and Metrology. 2022 Sep;5(3):230-9.
36. González BS, López-Quintela MA. New strategies and synthetic routes to synthesize fluorescent atomic quantum clusters.
37. Copp SM, Gorovits A, Swasey SM, Gudibandi S, Bogdanov P, Gwinn EG. Fluorescence color by data-driven design of genomic silver clusters. ACS nano. 2018 Jul 30;12(8):8240-7.
38. Porto V, Borrajo E, Buceta D, Carneiro C, Huseyinova S, Domínguez B, Borgman KJ, Lakadamyali M, Garcia-Parajo MF, Neissa J, García-Caballero T. Silver atomic quantum clusters of three atoms for cancer therapy: targeting chromatin compaction to increase the therapeutic index of chemotherapy. Advanced Materials. 2018 Aug;30(33):1801317.
39. Abbas MA, Kamat PV, Bang JH. Thiolated gold nanoclusters for light energy conversion. ACS Energy Letters. 2018 Mar 2;3(4):840-54.
40. Liu L, Corma A. Metal catalysts for heterogeneous catalysis: from single atoms to nanoclusters and nanoparticles. Chemical reviews. 2018 Apr 16;118(10):4981-5079.
41. Passalacqua R, Parathoner S, Centi G, Halder A, Tyo EC, Yang B, Seifert S, Vajda S. Electrochemical behaviour of naked sub-nanometre sized copper clusters and effect of CO 2. Catalysis Science & Technology. 2016;6(18):6977-85.
42. Halder A, Curtiss LA, Fortunelli A, Vajda S. Perspective: Size selected clusters for catalysis and electrochemistry. The Journal of chemical physics. 2018 Mar 21;148(11).
43. Dieste M, Arias IR, Buceta D, Davila N, Lopez-Quintela MA, Vázquez C. CO2 valorization: A new alternative catalysis with Ag and Cu Metal Molecules.
44. Popok VN, Barke I, Campbell EE, Meiwes-Broer KH. Cluster–surface interaction: From soft landing to implantation. Surface Science Reports. 2011 Oct 1;66(10):347-77.
45. Alonso JA. Electronic and atomic structure, and magnetism of transition-metal clusters. Chemical reviews. 2000 Feb 9;100(2):637-78.

46. Bickelhaupt FM, Baerends EJ. Kohn-Sham density functional theory: predicting and understanding chemistry. Reviews in computational chemistry. 2000 Jan 1:1-86.
47. Van Mourik T, Bühl M, Gaigeot MP. Density functional theory across chemistry, physics and biology. Philosophical Transactions of the Royal Society A: Mathematical, Physical and Engineering Sciences. 2014 Mar 13;372(2011):20120488.
48. Orio M, Pantazis DA, Neese F. Density functional theory. Photosynthesis research. 2009 Dec;102(2):443-53.
49. Martin RM. Electronic structure: basic theory and practical methods. Cambridge university press; 2020 Aug 27.
50. Al-Khaykanee MK. Quantum theory of electronic and thermal transport through nano-scale and single-molecule devices. Lancaster University (United Kingdom); 2018.
51. Schrödinger E. An undulatory theory of the mechanics of atoms and molecules. Physical review. 1926 Dec 1;28(6):1049.
52. Lee TD, Yang CN. Many-body problem in quantum statistical mechanics. I. General formulation. Physical Review. 1959 Mar 1;113(5):1165.
53. Fock V. Näherungsmethode zur Lösung des quantenmechanischen Mehrkörperproblems. Zeitschrift für Physik. 1930 Jan;61(1):126-48
54. Pauling L. The Application of the Quantum Mechanics to the Structure of the Hydrogen Molecule and Hydrogen Molecule-Ion and to Related Problems. Chemical Reviews. 1928 Jul 1;5(2):173-213.
55. Møller C, Plesset MS. Note on an approximation treatment for many-electron systems. Physical review. 1934 Oct 1;46(7):618.
56. Christiansen O. Vibrational coupled cluster theory. The Journal of chemical physics. 2004 Feb 1;120(5):2149-59.
57. Born M, Oppenheimer R. Zur quantentheorie der molekeln. Annalen der physik. 1927;389(20):457-84.
58. Hohenberg P, Kohn W. Inhomogeneous electron gas. Physical review. 1964 Nov 9;136(3B): B864.
59. Kohn W, Sham LJ. Self-consistent equations including exchange and correlation effects. Physical review. 1965 Nov 15;140(4A): A1133.
60. Parr RG. Density functional theory of atoms and molecules. InHorizons of Quantum Chemistry: Proceedings of the Third International Congress of Quantum Chemistry

Held at Kyoto, Japan, October 29-November 3, 1979 1989 (pp. 5-15). Dordrecht: Springer Netherlands.

61. Levy M. Electron densities in search of Hamiltonians. Physical Review A. 1982 Sep 1;26(3):1200.
62. Lieb EH. Thomas-Fermi and related theories of atoms and molecules. Reviews of Modern Physics. 1981 Oct 1;53(4):603.
63. Hartree DR. The wave mechanics of an atom with a non-Coulomb central field. Part I. Theory and methods. InMathematical Proceedings of the Cambridge Philosophical Society 1928 Jan (Vol. 24, No. 1, pp. 89-110). Cambridge university press.
64. Hartree DR. The calculation of atomic structures. J. Wiley; 1957.
65. Kohn W, Becke AD, Parr RG. Density functional theory of electronic structure. The journal of physical chemistry. 1996 Aug 1;100(31):12974-80.
66. Jones RO, Gunnarsson O. The density functional formalism, its applications and prospects. Reviews of Modern Physics. 1989 Jul 1;61(3):689.
67. Grossman JC, Mitas L, Raghavachari K. Structure and stability of molecular carbon: importance of electron correlation. Physical review letters. 1995 Nov 20;75(21):3870.
68. Zupan A, Blaha P, Schwarz K, Perdew JP. Pressure-induced phase transitions in solid Si, SiO 2, and Fe: Performance of local-spin-density and generalized-gradient-approximation density functionals. Physical Review B. 1998 Nov 1;58(17):11266.
69. Perdew JP, Burke K, Ernzerhof M. Generalized gradient approximation made simple. Physical review letters. 1996 Oct 28;77(18):3865.
70. Penev E, Kratzer P, Scheffler M. Effect of the cluster size in modeling the H 2 desorption and dissociative adsorption on Si (001). The Journal of chemical physics. 1999 Feb 22;110(8):3986-94.
71. Zhang GP, Mu YQ, Zhao JM, Huang H, Hu GC, Li ZL, Wang CK. Optimizing the conductance switching performance in photoswitchable dimethyldihydropyrene/cyclophanediene single-molecule junctions. Physica E: Low-dimensional Systems and Nanostructures. 2019 May 1;109:1-5.
72. Grimme S. Density functional theory with London dispersion corrections. Wiley Interdisciplinary Reviews: Computational Molecular Science. 2011 Mar;1(2):211-28.
73. Kristyán S, Pulay P. Can (semi) local density functional theory account for the London dispersion forces?. Chemical physics letters. 1994 Oct 28;229(3):175-80.
74. Pérez-Jordá J, Becke AD. A density-functional study of van der Waals forces: rare gas diatomics. Chemical physics letters. 1995 Feb 3;233(1-2):134-7.

75. Grimme S. Semiempirical GGA-type density functional constructed with a long-range dispersion correction. Journal of computational chemistry. 2006 Nov 30;27(15):1787-99.
76. Goerigk L. A comprehensive overview of the DFT-D3 London-dispersion correction. Non-covalent interactions in quantum chemistry and physics. 2017 Jan 1:195-219.
77. Grimme S, Antony J, Ehrlich S, Krieg H. A consistent and accurate ab initio parametrization of density functional dispersion correction (DFT-D) for the 94 elements H-Pu. The Journal of chemical physics. 2010 Apr 21;132(15).
78. Huang H. *A density functional theory study into the mechanism and reactivity in heterogeneous system* (Doctoral dissertation, Queen's University Belfast).
79. Grimme S, Ehrlich S, Goerigk L. Effect of the damping function in dispersion corrected density functional theory. Journal of computational chemistry. 2011 May;32(7):1456-65.
80. Smith DG, Burns LA, Patkowski K, Sherrill CD. Revised damping parameters for the D3 dispersion correction to density functional theory. The journal of physical chemistry letters. 2016 Jun 16;7(12):2197-203.
81. Kresse G, Furthmüller J. Efficiency of AB-initio total energy calculations for metals and semiconductors using a plane-wave basis set. Computational Materials Science. 1996;6(1):15–50.
82. Teter MP, Payne MC, Allan DC. Solution of Schrödinger's equation for large systems. Physical Review B. 1989 Dec 15;40(18):12255.
83. Bylander DM, Kleinman L, Lee S. Self-consistent calculations of the energy bands and bonding properties of B 12 C 3. Physical Review B. 1990 Jul 15;42(2):1394.
84. Cramer CJ, Bickelhaupt FM. Essentials of computational chemistry. ANGEWANDTE CHEMIE-INTERNATIONAL EDITION IN ENGLISH-. 2003;42(4):381-.
85. Wang V, Xu N, Liu J-C, Tang G, Geng W-T. VASPKIT: A user-friendly interface facilitating high-throughput computing and analysis using VASP Code. Computer Physics Communications. 2021;267:108033. doi:10.1016/j.cpc.2021.108033
86. Mathew K, Sundararaman R, Letchworth-Weaver K, Arias TA, Hennig RG. Implicit solvation model for density-functional study of nanocrystal surfaces and reaction pathways. The Journal of chemical physics. 2014 Feb 28;140(8).
87. Mathew K, Kolluru VS, Mula S, Steinmann SN, Hennig RG. Implicit self-consistent electrolyte model in plane-wave density-functional theory. The Journal of chemical physics. 2019 Dec 21;151(23).

88. Kresse G, Joubert D. From ultrasoft pseudopotentials to the projector augmented-wave method. Physical review b. 1999 Jan 15;59(3):1758.
89. Johnson DD. Modified Broyden's method for accelerating convergence in self-consistent calculations. Physical Review B. 1988 Dec 15;38(18):12807.
90. Kresse G, Furthmüller J. Efficient iterative schemes for ab initio total-energy calculations using a plane-wave basis set. Physical review B. 1996 Oct 15;54(16):11169.
91. Phillips JC. Energy-band interpolation scheme based on a pseudopotential. Physical Review. 1958 Nov 1;112(3):685.
92. Yin MT, Cohen ML. Ab initio pseudopotential theory. Phys. Rev. B: Condens. Matter;(United States). 1982 Jun 15;25(12).
93. Kleinman L, Bylander DM. Efficacious form for model pseudopotentials. Physical Review Letters. 1982 May 17;48(20):1425.
94. Vanderbilt D. Soft self-consistent pseudopotentials in a generalized eigenvalue formalism. Physical review B. 1990 Apr 15;41(11):7892.
95. King-Smith RD, Vanderbilt D. Theory of polarization of crystalline solids. Physical Review B. 1993 Jan 15;47(3):1651.
96. Blöchl PE. Projector augmented-wave method. Physical review B. 1994 Dec 15;50(24):17953.
97. Bader RF. A quantum theory of molecular structure and its applications. Chemical Reviews. 1991 Jul 1;91(5):893-928.
98. Henkelman G, Arnaldsson A, Jónsson H. A fast and robust algorithm for Bader decomposition of charge density. Computational Materials Science. 2006 Jun 1;36(3):354-60.
99. Sanville E, Kenny SD, Smith R, Henkelman G. Improved grid-based algorithm for Bader charge allocation. Journal of computational chemistry. 2007 Apr 15;28(5):899-908.
100. Tang W, Sanville E, Henkelman G. A grid-based Bader analysis algorithm without lattice bias. Journal of Physics: Condensed Matter. 2009 Jan 30;21(8):084204.
101. Mistry H, Choi Y, Bagger A, Scholten F, Bonifacio CS, Sinev I, et al. Enhanced carbon dioxide electroreduction to carbon monoxide over defect-rich plasma-activated silver catalysts. Angewandte Chemie. 2017;129(38):11552–6. doi:10.1002/ange.201704613

102. Zhu S, Qin X, Wang Q, Li T, Tao R, Gu M, Shao M. Composition-dependent CO 2 electrochemical reduction activity and selectivity on Au–Pd core–shell nanoparticles. Journal of Materials Chemistry A. 2019;7(28):16954-61.
103. Sekimoto T, Deguchi M, Yotsuhashi S, Yamada Y, Masui T, Kuramata A, Yamakoshi S. Highly selective electrochemical reduction of CO2 to HCOOH on a gallium oxide cathode. Electrochemistry communications. 2014 Jun 1;43:95-7.
104. Hara K, Kudo A, Sakata T. Electrochemical reduction of carbon dioxide under high pressure on various electrodes in an aqueous electrolyte. Journal of Electroanalytical Chemistry. 1995;391(1–2):141–7. doi:10.1016/0022-0728(95)03935-a.
105. Lieber CM, Lewis NS. Catalytic reduction of carbon dioxide at carbon electrodes modified with cobalt phthalocyanine. Journal of the American Chemical Society. 1984;106(17):5033–4. doi:10.1021/ja00329a082.
106. Zhang X-G, Jin X, Wu D-Y, Tian Z-Q. Selective electrocatalytic mechanism of CO2 reduction reaction to CO on silver electrodes: A unique reaction intermediate. The Journal of Physical Chemistry C. 2018;122(44):25447–55. doi:10.1021/acs.jpcc.8b08170
107. Kondratenko EV, Mul G, Baltrusaitis J, Larrazábal GO, Pérez-Ramírez J. Status and perspectives of CO2 conversion into fuels and chemicals by catalytic, photocatalytic and electrocatalytic processes. Energy & Environmental Science. 2013;6(11):3112. doi:10.1039/c3ee41272e.
108. Seifitokaldani A, Gabardo CM, Burdyny T, Dinh C-T, Edwards JP, Kibria MG, et al. Hydronium-induced switching between CO2 electroreduction pathways. Journal of the American Chemical Society. 2018;140(11):3833–7. doi:10.1021/jacs.7b13542
109. Rosen J, Hutchings GS, Lu Q, Rivera S, Zhou Y, Vlachos DG, Jiao F. Mechanistic insights into the electrochemical reduction of CO2 to CO on nanostructured Ag surfaces. Acs Catalysis. 2015 Jul 2;5(7):4293-9.
110. Clark EL, Ringe S, Tang M, Walton A, Hahn C, Jaramillo TF, et al. Influence of atomic surface structure on the activity of AG for the electrochemical reduction of CO2 To Co. ACS Catalysis. 2019;9(5):4006–14. doi:10.1021/acscatal.9b00260
111. Yuan X, Wu Y, Jiang B, Wu Z, Tao Z, Lu X, et al. Interface Engineering of silver-based heterostructures for co2 reduction reaction. ACS Applied Materials & Interfaces. 2020;12(50):56642–9. doi:10.1021/acsami.0c19031

112. Hoshi N, Kato M, Hori Y. Electrochemical reduction of CO2 on single crystal electrodes of Silver AG(111), AG(100) and AG(110). Journal of Electroanalytical Chemistry. 1997;440(1–2):283–6. doi:10.1016/s0022-0728(97)00447-6

113. Taylor HS. A theory of the catalytic surface. Proceedings of the Royal Society of London. Series A, Containing Papers of a Mathematical and Physical Character. 1925 May 1;108(745):105-11.

114. Echt O, Jena P, Rao BK, Khanna SN. Physics and chemistry of small clusters. Jena, P., Rao, BK, Khanna, SN,(eds.). 1987;158:623.

115. FUJITA M. Engineering a Small World: From Atomic Manipulation to Microfabrication (A special section of Science). Science. 1991;254:1300.

116. Brauman JI. Clusters. Science. 1996 Feb 16;271(5251):889-.

117. Du Y, Sheng H, Astruc D, Zhu M. Atomically precise noble metal nanoclusters as efficient catalysts: a bridge between structure and properties. Chemical reviews. 2019 Mar 22;120(2):526-622.

118. Agrawal BK, Agrawal S, Srivastava P, Singh S. Ab-initio study of small silver nanoclusters. Journal of Nanoparticle Research. 2004;6(4):363–8.

119. Straumanis ME. Neubestimmung der Gitterparameter, Dichten und thermischen Ausdehnungskoeffizienten von Silber und Gold, und Vollkommenheit der struktur. Monatshefte fur Chemie. 1971;102(5):1377–86.

120. Ong SP, Richards WD, Jain A, Hautier G, Kocher M, Cholia S, Gunter D, Chevrier VL, Persson KA, Ceder G. Python Materials Genomics (pymatgen): A robust, open-source python library for materials analysis. Computational Materials Science. 2013 Feb 1;68:314-9.

121. Momma K, Izumi F. VESTA 3 for three-dimensional visualization of crystal, volumetric and morphology data. Journal of applied crystallography. 2011 Dec 1;44(6):1272-6.

122. Jmol development team. Jmol [Internet]. 2016. Available from: http://jmol.sourceforge.net/

123. Yu M, Trinkle DR. Accurate and efficient algorithm for Bader charge integration. The Journal of chemical physics. 2011 Feb 14;134(6).

124. Beale MH, Hagan MT, Demuth HB. Neural network toolbox. User's Guide, MathWorks. 2010 Jan;2:77-81.

125. Alotaibi M, Wu Q, Lambert C. Computational studies of Ag5 atomic quantum clusters deposited on anatase and rutile TiO2 surfaces. Applied Surface Science. 2023 Mar 15;613:156054.
126. Heiles S, Johnston RL. Global optimization of clusters using electronic structure methods. International Journal of Quantum Chemistry. 2013 Sep 15;113(18):2091-109.
127. Bonacic-Koutecky V, Cespiva L, Fantucci P, Koutecky J. Effective core potential-configuration interaction study of electronic structure and geometry of small neutral and cationic Agn clusters: Predictions and interpretation of measured properties. The Journal of chemical physics. 1993;98(10):7981-94.
128. Garg S, Kaur N, Goel N, Molayem M, Grigoryan VG, Springborg M. Properties of naked silver clusters with up to 100 atoms as found with embedded-atom and density-functional calculations. Molecules. 2023 Apr 6;28(7):3266.
129. Singh S. Energy crisis and climate change: Global concerns and their solutions. Energy: crises, challenges and solutions. 2021 Sep 10:1-7.
130. Handoko AD, Steinmann SN, Seh ZW. Theory-guided materials design: two-dimensional MXenes in electro-and photocatalysis. Nanoscale Horizons. 2019;4(4):809-27.
131. Wang J, Zou J, Hu X, Ning S, Wang X, Kang X, Chen S. Heterostructured intermetallic CuSn catalysts: high performance towards the electrochemical reduction of CO 2 to formate. Journal of Materials Chemistry A. 2019;7(48):27514-21.
132. Choi SY, Jeong SK, Kim HJ, Baek IH, Park KT. Electrochemical reduction of carbon dioxide to formate on tin–lead alloys. ACS Sustainable Chemistry & Engineering. 2016 Mar 7;4(3):1311-8.
133. An X, Li S, Yoshida A, Wang Z, Hao X, Abudula A, Guan G. Electrodeposition of tin-based electrocatalysts with different surface tin species distributions for electrochemical reduction of CO2 to HCOOH. ACS Sustainable Chemistry & Engineering. 2019 Apr 29;7(10):9360-8.
134. Li Q, Zhang Y, Zhang X, Wang H, Li Q, Sheng J, Yi J, Liu Y, Zhang J. Novel Bi, BiSn, Bi2Sn, Bi3Sn, and Bi4Sn catalysts for efficient electroreduction of CO2 to formic acid. Industrial & Engineering Chemistry Research. 2019 Aug 19;59(15):6806-14.
135. Hailu A, Tamijani AA, Mason SE, Shaw SK. Efficient conversion of CO2 to formate using inexpensive and easily prepared post-transition metal alloy catalysts. Energy & fuels. 2020 Jan 28;34(3):3467-76.

136. Han N, Wang Y, Deng J, Zhou J, Wu Y, Yang H, Ding P, Li Y. Self-templated synthesis of hierarchical mesoporous SnO 2 nanosheets for selective CO 2 reduction. Journal of Materials Chemistry A. 2019;7(3):1267-72.
137. Zhang S, Kang P, Meyer TJ. Nanostructured tin catalysts for selective electrochemical reduction of carbon dioxide to formate. Journal of the American Chemical Society. 2014 Feb 5;136(5):1734-7.
138. Wen G, Ren B, Park MG, Yang J, Dou H, Zhang Z, Deng YP, Bai Z, Yang L, Gostick J, Botton GA. Ternary Sn-Ti-O Electrocatalyst Boosts the Stability and Energy Efficiency of CO2 Reduction. Angewandte Chemie International Edition. 2020 Jul 27;59(31):12860-7.
139. Yoo JS, Christensen R, Vegge T, Nørskov JK, Studt F. Theoretical insight into the trends that guide the electrochemical reduction of carbon dioxide to formic acid. ChemSusChem. 2016 Feb;9(4):358-63.
140. Li L, Ozden A, Guo S, García de Arquer FP, Wang C, Zhang M, Zhang J, Jiang H, Wang W, Dong H, Sinton D. Stable, active CO2 reduction to formate via redox-modulated stabilization of active sites. Nature communications. 2021 Sep 1;12(1):5223.
141. Zhang T, Qiu Y, Yao P, Li X, Zhang H. Bi-modified Zn catalyst for efficient CO2 electrochemical reduction to formate. ACS Sustainable Chemistry & Engineering. 2019 Aug 14;7(18):15190-6.
142. Wang G, Chen J, Ding Y, Cai P, Yi L, Li Y, Tu C, Hou Y, Wen Z, Dai L. Electrocatalysis for CO 2 conversion: from fundamentals to value-added products. Chemical Society Reviews. 2021;50(8):4993-5061.
143. Seh ZW, Kibsgaard J, Dickens CF, Chorkendorff IB, Nørskov JK, Jaramillo TF. Combining theory and experiment in electrocatalysis: Insights into materials design. Science. 2017 Jan 13;355(6321):eaad4998.
144. Jiang X, Wang X, Liu Z, Wang Q, Xiao X, Pan H, Li M, Wang J, Shao Y, Peng Z, Shen Y. A highly selective tin-copper bimetallic electrocatalyst for the electrochemical reduction of aqueous CO2 to formate. Applied Catalysis B: Environmental. 2019 Dec 15;259:118040.
145. Ye K, Zhou Z, Shao J, Lin L, Gao D, Ta N, Si R, Wang G, Bao X. In situ reconstruction of a hierarchical Sn-Cu/SnOx core/shell catalyst for high-performance CO2 electroreduction. Angewandte Chemie International Edition. 2020 Mar 16;59(12):4814-21.

146. El-Ashram T. The relation between valency, axial ratio, Young's modulus and resistivity of rapidly solidified tin-based eutectic alloys. Journal of Materials Science: Materials in Electronics. 2005 Aug;16(8):501-5.